

---

---

# COMPUTATIONAL STUDIES OF AROMATIC SUBSTITUTION AND GAS-SURFACE REACTIONS

---

---

By

**NISHANT SHARMA**

CHEM11201504004

National Institute of Science Education and Research Bhubaneswar

*A thesis submitted to the  
Board of Studies in Chemical Sciences  
in partial fulfillment of requirements for the degree of  
DOCTOR OF PHILOSOPHY  
of*

**HOMI BHABHA NATIONAL INSTITUTE**





# Homi Bhabha National Institute

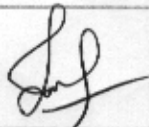
## Recommendations of the Viva Voce Committee

As members of the Viva Voce Committee, we certify that we have read the dissertation prepared by **Nishant Sharma** entitled "**Computational Studies of Aromatic Substitution and Gas-Surface Reactions**" and recommend that it may be accepted as fulfilling the thesis requirement for the award of Degree of Doctor of Philosophy.

---

Chairman – Prof. A. Srinivasan  Date: 23.07.21

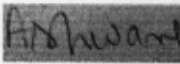
---

Guide / Convener – Dr. U. Lourderaj  Date: 23/7/2021

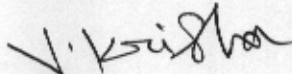
---

Co-Guide Date:

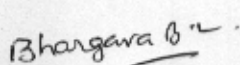
---

Examiner – Prof. A. Tiwari  Date: 23/07/2021

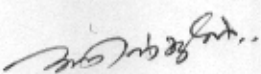
---

Member 1 – Dr. V. Krishnan  Date: 23/7/2021

---

Member 2 – Dr. B. L. Bhargava  Date: 23/7/2021

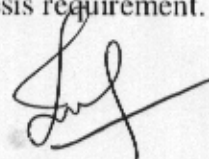
---

Member 3\* – Dr. A. V. Anil Kumar  Date: 23/7/2021

---

Final approval and acceptance of this thesis is contingent upon the candidate's submission of the final copies of the thesis to HBNI.

We hereby certify that we have read this thesis prepared under my/our direction and recommend that it may be accepted as fulfilling the thesis requirement.



Date: 23 July 2021

Place: Bhubaneswar

(Dr. U. Lourderaj)

(Guide)



## STATEMENT BY AUTHOR

This dissertation has been submitted in partial fulfillment of requirements for an advanced degree at Homi Bhabha National Institute (HBNI) and is deposited in the Library to be made available to borrowers under rules of the HBNI.

Brief quotations from this dissertation are allowable without special permission, provided that accurate acknowledgement of source is made. Requests for permission for extended quotation from or reproduction of this manuscript in whole or in part may be granted by the Competent Authority of HBNI when in his or her judgment the proposed use of the material is in the interests of scholarship. In all other instances, however, permission must be obtained from the author.



Signature of the Student  
Nishant Sharma



## DECLARATION

I hereby declare that the investigation presented in the thesis has been carried out by me. The work is original and has not been submitted earlier as a whole or in part for a degree/diploma at this or any other Institution/University.

A handwritten signature in black ink, appearing to read 'Nishant', written over a horizontal line.

Signature of the Student  
Nishant Sharma



## LIST OF PUBLICATIONS ARISING FROM THE THESIS

### Journal

1. **N. Sharma**, J. K. Ajay, K. Venkatasubbaiah, and U. Lourderaj, "Mechanisms and Dynamics of Protonation and Lithiation of Ferrocene." *Phys. Chem. Chem. Phys.* **2015**, *17*, 22204
2. **N. Sharma**, R. Biswas and U. Lourderaj, "Dynamics of a Gas-phase  $S_NAr$  Reaction: Non-concerted Mechanism Despite the Meisenheimer Complex being a Transition State." *Phys. Chem. Chem. Phys.* **2020**, *22*, 26562

### Manuscripts under preparation

1. **N. Sharma**, P. Sharma and U. Lourderaj, Dissociation Dynamics of Formaldehyde on Single Graphene Sheet
2. **N. Sharma**, P. Sharma and U. Lourderaj, Effect of Confinement on the Dissociation Dynamics of Formaldehyde
3. **N. Sharma**, K. Venkatasubbaiah and U. Lourderaj, Unusual Ortho-borylation of 1,1-Bis(trimethylstannyl)ferrocene using  $BCl_3$ : A DFT Study



Signature of the Student  
Nishant Sharma



## CONFERENCES

1. Spectroscopy and Dynamics of Molecules and Clusters (SDMC) - 2014 conference, organized by School of Chemical Sciences, NISER, BBSR.
2. Theoretical Chemistry Symposium (TCS) - 2014 conference, organized by National Chemical Laboratory, Pune.
3. Spectroscopy and Dynamics of Molecules and Clusters (SDMC) - 2016 conference, organized by IISER Pune.
4. International Conference on Molecular Energy Transfer in Complex Systems (iCOMET) - 2017, organized by University of Innsbruck, Austria.
5. Inter-IISER & NISER Chemistry Meet (IINCM) - 2017, organized by School of Chemical Sciences, NISER, BBSR.
6. Spectroscopy and Dynamics of Molecules and Clusters (SDMC) - 2018 conference, organized by IISER Kolkata.
7. Spectroscopy and Dynamics of Molecules and Clusters (SDMC) - 2019 conference, organized by IISER Mohali and IIT Kanpur.



Signature of the Student  
Nishant Sharma



## ACKNOWLEDGEMENTS

Firstly, I would like to express my sincere gratitude to my thesis advisor Dr. U. Lourderaj for his patience, motivation and continuous support during the course of my Ph.D work. I also thank the thesis monitoring committee members Prof. A. Srinivasan, Dr. V. Krishnan, Dr. B. L. Bhargava, and Dr. A. V. Anil Kumar for their support. I would also like to thank Dr. Jayanth K. Ajay, Dr. Prachi Sharma, and Mr. Rupayan Biswas for their collaboration in my research work. I would like to thank Professor J. Bowman, Emory University for sharing the potential energy surface of formaldehyde. I thank my labmates for all the stimulating discussions and for all the fun I have had in the last five years. Last but not the least, I would like to thank my family members for their unconditional love and support.



## ABSTRACT

Understanding the mechanism of various chemical reactions is of fundamental importance in chemistry. This helps chemists to control reactions and design new molecules. To this end, theoretical and computational chemistry has been used to get insights into the mechanisms followed in the reactions. The present thesis involves the study of the atomic-level mechanisms and dynamics of certain aromatic substitution and gas-surface reactions.

Understanding the mechanism of the electrophilic substitution of ferrocene has been a topic of interest due to its application in chemical synthesis. It was observed that hard electrophiles follow exo pathway in which incoming electrophile attacks the cyclopentadienyl rings of ferrocene to form agostic intermediate and soft electrophiles follow endo pathway where the electrophile interacts with the metal center to form metal-protonated intermediate. When the incoming electrophile is a  $H^+$ , both the exo and endo pathway will give the same intermediate and thus understanding the mechanism has been a topic of much debate over several decades. Here, we employed ab initio chemical dynamics simulations to understand the atomic-level mechanism of the protonation of ferrocene. The dynamics of the lithiation of ferrocene was also investigated by ab initio methods, where  $Li^+$  exhibits planetary motion about the Fe-center. An orientational preference of incoming electrophile was seen for lithiation of ferrocene but not for protonation of ferrocene. In addition, the mechanism of borylation reaction between 1,1'-bis(trimethylstannyl)ferrocene and  $BCl_3$  was investigated by density functional theory (DFT).

Nucleophilic aromatic substitution ( $S_NAr$ ) reactions are an important class of reactions in chemistry and the commonly accepted mechanism is the stepwise addition-elimination mechanism characterized by the formation of Meisenheimer complex. Recent studies have pointed out to a concerted mechanism where Meisenheimer structure (MS) is a transition state on the potential energy surface. In this study, a detailed investigation of the atomic-level mechanism and dynamics of  $C_6H_5NO_2 + F^-$  reaction was carried out using ab initio and DFT methods. The potential energy profile of this reaction consists of various ion-dipole and  $\sigma$ -complexes. Dynamical simulations revealed that the reaction follows a stepwise mechanism characterized by the formation of various  $\sigma$  and ion-dipole complexes, in spite of the presence

of a MS transition state. Interestingly, a roaming atom mechanism was also observed in the reaction.

Investigation of the mechanism of gas-surface reactions is important in the context of heterogeneous catalysis and energy transfer processes. It is important to understand the effect of the surface on the dissociation dynamics of molecules. Here, a model reaction, the unimolecular dissociation of  $\text{H}_2\text{CO}$  on a graphene sheet was investigated using classical trajectory method. The effect of reagent vibrational energy, relative orientation of  $\text{H}_2\text{CO}$ , and collision energy on the dynamics of  $\text{H}_2\text{CO}$  dissociation were investigated. In addition, the dissociation dynamics of  $\text{H}_2\text{CO}$  in confinement was also studied using two models: (i)  $\text{H}_2\text{CO}$  between two graphene sheets and (ii)  $\text{H}_2\text{CO}$  inside a carbon nanotube. The reaction probability was found to decrease with the decrease in the pore-size.

## TABLE OF CONTENTS

	Page
<b>Summary</b>	<b>xi</b>
<b>List of Figures</b>	<b>xv</b>
<b>List of Tables</b>	<b>xix</b>
<b>1 Introduction</b>	<b>1</b>
<b>2 Dynamics of Protonation and Lithiation of Ferrocene</b>	<b>11</b>
2.1 Introduction . . . . .	11
2.2 Methodology . . . . .	15
2.3 Results and Discussions . . . . .	16
2.3.1 Protonation of ferrocene . . . . .	16
2.3.2 Lithiation of ferrocene . . . . .	25
2.4 Summary and conclusions . . . . .	31
<b>3 Computational Study of Borylation of 1-1'-bis(trimethylstannyl)ferrocene with BCl<sub>3</sub></b>	<b>33</b>
3.1 Introduction . . . . .	33
3.2 Methodology . . . . .	35
3.3 Results . . . . .	35
3.3.1 Pathway for 1-2 product . . . . .	36
3.3.2 Reaction path for the formation of 1-3 product . . . . .	38
3.3.3 Free energy profile for direct product ( <b>F4</b> ) . . . . .	39
3.4 Discussion and summary . . . . .	40
<b>4 Mechanisms and dynamics of Nucleophilic Aromatic Substitution (S<sub>N</sub>Ar) reaction</b>	<b>43</b>

4.1	Introduction . . . . .	43
4.2	Methodology . . . . .	47
4.3	Results and Discussions . . . . .	48
4.3.1	Energetics . . . . .	48
4.3.2	<i>Ab initio</i> Chemical Dynamics . . . . .	52
4.4	Summary and Conclusions . . . . .	63
<b>5</b>	<b>Dissociation Dynamics of formaldehyde on graphene sheet</b>	<b>65</b>
5.1	Introduction . . . . .	65
5.2	Computational methods . . . . .	68
5.3	Results and discussion . . . . .	72
5.3.1	Effect of Vibrational Energy of H <sub>2</sub> CO . . . . .	72
5.3.2	Effect of Orientation of H <sub>2</sub> CO . . . . .	73
5.3.3	Roaming atom mechanism . . . . .	77
5.4	Summary . . . . .	81
<b>6</b>	<b>Effect of confinement on dissociation Dynamics of formaldehyde</b>	<b>83</b>
6.1	Introduction . . . . .	83
6.2	Computational Methods . . . . .	84
6.3	Results and discussions . . . . .	86
6.3.1	H <sub>2</sub> CO confined between two graphene sheets . . . . .	86
6.3.2	H <sub>2</sub> CO confined inside a single-walled carbon nanotube . . . . .	89
6.4	Summary . . . . .	91
	<b>Bibliography</b>	<b>93</b>

## LIST OF FIGURES

FIGURE	Page
2.1 <i>Exo</i> and <i>endo</i> pathways followed by electrophiles. . . . .	12
2.2 Comparison of energy differences between metal-protonated and agostic structures at different levels of theory. . . . .	14
2.3 Electrostatic potential map (in a.u.) of ferrocene for the iso-value of -0.013. . . .	16
2.4 Potential energy profile depicting the different isomers of the protonated ferrocene obtained at the B3LYP/DZVP level. . . . .	17
2.5 Structures of all the transition states obtained for protonated ferrocene. . . . .	19
2.6 Population vs lifetime plot for <b>AG</b> and <b>MP</b> isomers for trajectories initiated at <b>AG</b> (a and b) and <b>MP</b> (c and d), respectively. . . . .	21
2.7 Partially optimized geometries to mimic bimolecular collision between H <sup>+</sup> and ferrocene. . . . .	23
2.8 Plots of $\angle X_1\text{-Fe-H}(\circ)$ vs Fe-H distance( $\text{\AA}$ ) in polar coordinates. (a) Initial orientation of H <sup>+</sup> in 80 trajectories is shown. (b) 3 representative trajectories showing different attacks. . . . .	24
2.9 Superimposed frames for representative trajectories exhibiting (a) <i>exo</i> attack and H <sup>+</sup> hopping on the Cp ring and (b) <i>endo</i> attack and H <sup>+</sup> motion between the two Cp rings. The incoming H <sup>+</sup> is shown in blue color. . . . .	25
2.10 Orbit of Li <sup>+</sup> cation around Ferrocene. Adapted with permission from Ref. [21]. Copyright 2001 American Chemical Society. . . . .	26
2.11 Energetic of lithiated ferrocene calculated at the B3LYP/DZVP level of theory. . .	27
2.12 Plot of Fe-Li and C-Li distances as a function of time for a representative trajectory that showed planetary motion. . . . .	28
2.13 Plots of $\angle X_1\text{-Fe-Li}(\circ)$ vs Fe-Li distance in polar coordinates ( $\text{\AA}$ ). (a) Initial orientation of Li <sup>+</sup> in 80 trajectories. (b) 3 representative trajectories showing different attacks. . . . .	30

2.14	Superimposed frames for representative trajectories exhibiting (a) <i>exo</i> attack of Li <sup>+</sup> followed by planetary motion and (b) <i>endo</i> attack of Li <sup>+</sup> followed by the formation of <b>CP</b> and then <b>ML</b> via <b>TSd</b> . The incoming Li <sup>+</sup> is shown in red color. . . . .	31
3.1	Reaction of trimethylstannyl ferrocene and 1-1'-bis(trimethylstannyl)ferrocene with BCl <sub>3</sub> to give BCl <sub>2</sub> substituted ferrocene derivatives. . . . .	34
3.2	<b>1-2'</b> and <b>1-3'</b> isomers of 1-1'-bis(trimethylstannyl)ferrocene . . . . .	36
3.3	Free energy profile of <i>exo</i> attack of BCl <sub>3</sub> to form $\alpha$ -substituted <b>1-2</b> product . . . . .	37
3.4	Free energy profile of <i>exo</i> attack of BCl <sub>3</sub> on <b>1-3'</b> isomer . . . . .	38
3.5	Free energy profile of <i>exo</i> attack of BCl <sub>3</sub> to form <b>1-3</b> product . . . . .	39
3.6	Free energy profile for the formation of <b>direct</b> product ( <b>F2</b> ) . . . . .	40
4.1	Potential energy profile for the reaction C <sub>6</sub> H <sub>5</sub> NO <sub>2</sub> + F <sup>-</sup> → C <sub>6</sub> H <sub>5</sub> F + NO <sub>2</sub> <sup>-</sup> at B3LYP/6-31+G* level of theory . . . . .	50
4.2	Optimized structures of different stationary points and their important geometrical parameters obtained at the B3LYP/6-31+G* level of theory . . . . .	51
4.3	Rotated coordinate system with C1 as the origin. . . . .	53
4.4	Coordinates (Å) of F atom during the reaction for three bimolecular reactive trajectories in the rotated coordinate system. The <i>IRC</i> path is also shown for comparison. . . . .	54
4.5	Snapshots of a representative bimolecular reactive trajectory . . . . .	54
4.6	Three largest principal components (PC1, PC2 and PC3) representing <i>IRC</i> in R3D space . . . . .	56
4.7	Plot of F atom cartesian coordinates in Å along the <i>IRC</i> path in the rotated coordinate system. Various stationary point are also shown along the <i>IRC</i> path . . . . .	57
4.8	Sample trajectories initiated at the transition state <b>mts</b> that follow (a) <i>IRC</i> , (b) direct- <i>IRC</i> , (c) non- <i>IRC</i> and (d) roaming pathways. Right: The cartesian coordinates of F atom (Å) in MEP and in the representative trajectory. ★ denotes the beginning of the trajectory. Left: Plot of minimum deviation from <i>IRC</i> ( $d_{\min}$ ) as a function of time for sample trajectories in the R3D space computed from PCA. The color coding in the right figures indicate stationary point which is closer to a given point in the trajectory . . . . .	59
4.9	Lifetime distribution for (a) <b>idp</b> , (b) <b>idm</b> , (c) <b>ido</b> , (d) <b>osc</b> , and (e) <b>ipc</b> for 150 reactive trajectories initiated at the transition stata <b>mts</b> . (f) Lifetime distribution for <b>ipc</b> intermediate formed just before the formation of the products . . . . .	61

4.10	Distribution of total lifetime in the intermediate region for the 150 reactive trajectories initiated at <b>mts</b> transition state. . . . .	62
5.1	Relative energies for minima and saddle points on the ground state PES of formaldehyde. . . . .	68
5.2	Orientations of the H <sub>2</sub> CO-pyrene system considered for calculating interaction potential, $V_{\text{int}}$ . . . . .	70
5.3	Reaction probability as a function of H <sub>2</sub> CO vibrational energy . . . . .	73
5.4	Four different orientations of H <sub>2</sub> CO with respect to graphene considered in the trajectory simulations. . . . .	74
5.5	Reaction probability as a function of different collision energies for four different orientations of H <sub>2</sub> CO. . . . .	75
5.6	Reaction probability as a function of collision energy for H <sub>2</sub> + CO channel. . . . .	76
5.7	Reaction probability as a function of collision energy for H + HCO channel. . . . .	77
5.8	Reaction probability as a function of collision energy for random orientations. . . . .	78
5.9	Reaction probability as a function of collision energy for three different pathways. . . . .	79
5.10	Vibrational state distribution of H <sub>2</sub> products ( $\nu_{\text{H}_2}$ ) formed in gas-phase dissociation and in the dissociation of H <sub>2</sub> CO on graphene. . . . .	80
5.11	Rotational state distribution of H <sub>2</sub> products ( $J_{\text{CO}}$ ) formed in gas-phase dissociation and in the dissociation of H <sub>2</sub> CO on graphene. . . . .	81
6.1	Model for H <sub>2</sub> CO confined between two graphene sheets. . . . .	86
6.2	Reaction probability as a function of distance between the two graphene sheets. . . . .	87
6.3	Plot of $z$ -component of the coordinates (Å) for C atom of H <sub>2</sub> CO vs time for three representative (a) reactive and (b) non-reactive trajectories. The two graphene sheets are placed 20 Å apart. . . . .	88
6.4	Model for H <sub>2</sub> CO confined inside single-walled nanotube. . . . .	89
6.5	Snapshot of a representative trajectory that forms H + HCO inside a CNT. . . . .	90
6.6	Reaction probability as a function of the diameter of carbon nanotube . . . . .	91



## LIST OF TABLES

TABLE	Page
2.1 Comparison of structural parameters and relative energies of ferrocene and its protonated forms . . . . .	17
2.2 Comparison of structural parameters and relative energies of three different transition states . . . . .	18
4.1 Electronic energies (kcal/mol) of stationary points relative to the reactants obtained at different levels of theory <sup>a</sup> . . . . .	49
4.2 Geometrical criteria used to define various intermediate region for the calculation of lifetimes of different intermediates. . . . .	60
4.3 Average lifetimes of various intermediates computed from 150 trajectories initiated at <b>mts</b> . . . . .	62
5.1 Parameters for H <sub>2</sub> CO - graphene interaction obtained from the fit . . . . .	71
5.2 Reaction probabilities for different orientations and Collision energy . . . . .	75



## INTRODUCTION

Chemical reactions are transformations in which molecules interact with each other to form new chemical entities. Some reactions are spontaneous while others need energy (activation energy,  $E_a$ ) in the form of heat or light. This energy helps molecule to cross the barrier and form products. It is of fundamental interest to understand how molecules interact with each other during a reaction and the underlying atomic-level mechanisms that lead to the formation of products. Understanding the atomic-level mechanism of reactions gives control and freedom to alter the pathway to get new and targeted products. Various experimental and computational methods are employed to understand chemical reaction mechanisms.

Computational chemistry has been used extensively to understand the results from experiments and to predict the outcomes of reactions beforehand. In general, chemical reactions can be investigated computationally using two approaches: (i) Energetics of the reaction and (ii) dynamics of various processes.

**(i) Energetics of the reaction:** Here, the energies of the stationary points on the potential

energy surface (PES) viz, the reactants, products, the transition states and the intermediates are calculated and compared. From the energetics, a mechanism is proposed to explain the experimental observations. The stationary point energies, their geometries and the electronic structure properties are computed by solving the time-independent Schrödinger equation (TISE) of the system (molecule) under Born-Oppenheimer approximation which is discussed below.

The time-independent Schrödinger equation<sup>1</sup> (TISE) of the system given as,

$$\hat{H}\Psi(\vec{r}, \vec{R}) = E\Psi(\vec{r}, \vec{R}) \quad (1.1)$$

In equation 1.1,  $\hat{H}$  is the Hamiltonian operator,  $\Psi$  is the wavefunction of the system, and  $E$  is the energy of the system,  $\vec{r}$  denotes the coordinates of the electrons and  $\vec{R}$  denotes the coordinates of the nuclei. The wavefunction  $\Psi$  is a function of the coordinates of electrons and nuclei. The Hamiltonian for a molecular system with  $n$  electrons and  $N$  nuclei is written as:

$$\hat{H} = -\frac{\hbar^2}{2m_e} \sum_i^n \nabla_i^2 - \frac{\hbar^2}{2} \sum_A^N \frac{1}{M_A} \nabla_A^2 - \frac{e^2}{4\pi\epsilon_0} \sum_i^n \sum_A^N \frac{Z_A}{r_{iA}} + \frac{e^2}{4\pi\epsilon_0} \sum_j^n \sum_{i>j}^n \frac{1}{r_{ij}} + \frac{e^2}{4\pi\epsilon_0} \sum_B^N \sum_{A>B}^N \frac{Z_A Z_B}{R_{AB}} \quad (1.2)$$

where,  $m_e$  is the mass of the electron,  $\hbar$  is the Planck's constant ( $h$ ) divided by  $2\pi$ ,  $M_A$  is the mass of nucleus A,  $Z_A$  and  $Z_B$  are the nuclear charges of A and B, respectively,  $r_{ij}$  is the distance between the electrons  $i$  and  $j$ ,  $R_{AB}$  is the distance between the nuclei A and B,  $r_{iA}$  is the distance between electron  $i$  and nucleus A and  $\epsilon_0$  is the permittivity of free space. The first and second set of terms in equation 1.2 represents kinetic energy of all the electrons and nuclei respectively, the third set of term represents the electrostatic attraction between the electrons and nuclei, the fourth and fifth set of terms represent electron-electron and nucleus-nucleus electrostatic repulsions respectively.

Since the mass of nuclei are much larger than the mass of electron, the motion of the nuclei are much slower than the motion of the electrons. So, from the perspective of electrons, the

nuclei can be considered as stationary. Thus, the electronic and nuclear coordinates can now be separated. This is known as Born-Oppenheimer (BO) approximation.<sup>1</sup> The total wavefunction of the system can now be written as,

$$\Psi(\vec{r}, \vec{R}) = \psi_{el}(\vec{r}; \vec{R})\psi_N(\vec{R}) \quad (1.3)$$

where,  $\psi_{el}(\vec{r}; \vec{R})$  is the electronic wavefunction of the system that depends parametrically on the nuclear coordinates  $\vec{R}$  and  $\psi_N(\vec{R})$  is the nuclear wavefunction of the system. Since nuclei can be fixed within BO approximation, the nuclear kinetic energy term in the Hamiltonian is set to zero. The equation 1.2 can now be written as,

$$\hat{H} = -\frac{\hbar^2}{2m_e} \sum_i^n \nabla_i^2 - \frac{e^2}{4\pi\epsilon_0} \sum_i^n \sum_A^N \frac{Z_A}{r_{iA}} + \frac{e^2}{4\pi\epsilon_0} \sum_j^n \sum_{i>j}^n \frac{1}{r_{ij}} + \frac{e^2}{4\pi\epsilon_0} \sum_B^N \sum_{A>B}^N \frac{Z_A Z_B}{R_{AB}} \quad (1.4)$$

$$\hat{H} = \hat{H}_{el} + \hat{V}_{NN} \quad (1.5)$$

In equation 1.5,  $\hat{H}_{el}$  is the electronic Hamiltonian given by,

$$\hat{H}_{el} = -\frac{\hbar^2}{2m_e} \sum_i^n \nabla_i^2 - \frac{e^2}{4\pi\epsilon_0} \sum_i^n \sum_A^N \frac{Z_A}{r_{iA}} + \frac{e^2}{4\pi\epsilon_0} \sum_j^n \sum_{i>j}^n \frac{1}{r_{ij}} \quad (1.6)$$

and  $\hat{V}_{NN}$  is the nuclear-nuclear repulsion term which is constant for the fixed nuclei.  $\hat{V}_{NN}$  is represented as,

$$\hat{V}_{NN} = \sum_B^N \sum_{A>B}^N \frac{Z_A Z_B}{R_{AB}} \quad (1.7)$$

The electronic Schrödinger equation can now be written as,

$$\hat{H}_{el}\psi_{el}(\vec{r}; \vec{R}) = E_{el}\psi_{el}(\vec{r}; \vec{R}). \quad (1.8)$$

where,  $\psi_{el}(\vec{r}; \vec{R})$  is the electronic wavefunction of the system and  $E_{el}$  is the electronic energy obtained by solving this equation. The potential energy surface (PES) of the system can now be calculated as,

$$V(\vec{R}) = E_{el}(\vec{r}; \vec{R}) + \hat{V}_{NN}(\vec{R}) \quad (1.9)$$

PES is the potential energy of a molecule as a function of  $3N-6$  degrees of freedom. It is worth pointing out that the reliability of the PES depends on the validity of BO approximation.

Stationary points are important aspect of the PES which is characterized when the first derivative of the potential energy ( $V$ ) with respect to each orthogonal normal coordinate ( $Q_i$ ) is equal to zero as shown below,

$$\left(\frac{\partial V}{\partial Q_i}\right) = 0; \quad \text{where, } i = 1, 2, 3, \dots, 3N - 6 \quad (1.10)$$

For a given chemical reaction, reactants, transition states, intermediates and products are all stationary points on the PES. The stationary points are then characterized as a minimum (reactants, intermediates and products) or a maximum (transition state and  $n^{\text{th}}$  order saddle) by computing the second derivatives of the potential energy with respect to the coordinates. For a minimum along all the coordinates  $Q_i$ ,

$$\left(\frac{\partial^2 V}{\partial Q_i^2}\right) > 0; \quad \text{where, } i = 1, 2, 3, \dots, 3N - 6 \quad (1.11)$$

On the other hand, a transition state is characterized by a maximum along one coordinate ( $Q_k$ ),

$$\left(\frac{\partial^2 V}{\partial Q_k^2}\right) < 0 \quad (1.12)$$

and minima in rest  $3N-7$  coordinates,

$$\left(\frac{\partial^2 V}{\partial Q_i^2}\right) > 0; \quad \text{where, } i = 1, 2, 3, \dots, 3N - 7 \quad (1.13)$$

Hence, by computing the classical vibrational frequencies, various stationary points are characterized as a minimum or maximum on the PES.

It is important to note that the electronic Schrödinger Equation 1.8 cannot be solved exactly for a system with more than one electron because of the non-separability of the electron-electron repulsion terms in the Hamiltonian. To address this problem, various approximate methods

were developed over the years. The common methods include Hartree-Fock (HF) method, Møller-Plesset perturbation theory, etc. These approximate methods are briefly discussed below.

In the Hartree method,<sup>2</sup> the electronic wavefunction  $\psi(\vec{r})$  is written as the product of the functions  $\phi(r_i)$  that depend only on one electron,

$$\psi(r_1, r_2, \dots, r_n) = \phi(r_1)\phi(r_2)\dots\phi(r_n) \quad (1.14)$$

where,  $r_i$ 's are the coordinates of electron  $i$ . This equation is known as Hartree product. The Hamiltonian in atomic units is then written as follows,

$$H = \sum_i \left[ H^c(i) + \sum_{j>i} \frac{1}{r_{ij}} \right] \quad (1.15)$$

where,  $H_i^c$  is the core Hamiltonian and the second term is the electron-electron repulsion term,  $i$  and  $j$  are the indices of the electrons. The core Hamiltonian  $H_i^c$  is given by,

$$H^c(i) = -\frac{1}{2}\nabla_i^2 - \sum_A \frac{Z_A}{r_{iA}} \quad (1.16)$$

The electron-electron repulsion terms in equation 1.15 is treated in an average way by assuming that each electron is moving independently in an average field created by rest of the electrons. Since, electron-electron repulsion term is treated in an average way, the energy obtained using this method is always greater than the true energy of the system. This is a very crude approximation because the freedom of an electron to adjust instantaneously due to the interactions with other electrons is missing.

The separable wavefunction used by Hartree does not follow Pauli exclusion principle. To solve this issue, Fock used Slater determinant to define the wavefunction of the system. This method is popularly known as HF method. The difference between the energy obtained via HF calculations ( $E_{\text{HF}}$ ) and exact energy of the system ( $E_{\text{exact}}$ ) is termed as the correlation energy ( $E_{\text{corr}}$ ),

$$E_{\text{corr}} = E_{\text{exact}} - E_{\text{HF}} \quad (1.17)$$

Depending on the problem, HF method can be improved by either incorporating electron-electron repulsion by adding an explicit term in the Hamiltonian or by adding excited state wavefunctions to HF wavefunction to represent  $\psi_{el}(\vec{r}; \vec{R})$ .

An alternative formalism to compute electronic energies is the density functional theory (DFT). The DFT method is based on Hohenberg-Kohn theorems<sup>3</sup> in which total electron density is used to compute electronic energy of the system i.e,

$$F[\rho(r)] = E_{elec} \quad (1.18)$$

where,  $\rho(r)$  is the total electron density of the system,  $E_{elec}$  is the electronic energy of the system and  $F$  is a functional. To solve for the electronic energy of the system, the functional has the form,

$$E[\rho(r)] = T_e[\rho(r)] + V_{ee}[\rho(r)] + V_{ne}[\rho(r)] + E_{XC}[\rho(r)] \quad (1.19)$$

where,  $T_e[\rho(r)]$  is the kinetic energy of the electrons and within DFT approach, it is defined as the kinetic energy of non-interacting electrons having same density as the real electrons in the system. The last term is the exchange-correlation functional. The accuracy of any DFT calculation strongly depends on the exchange-correlation functional  $E_{XC}$ . If  $E_{XC}$  is known accurately for a system, DFT would give exact results. In DFT approach, the challenge is to find accurate  $E_{XC}$  for a given system. Various empirical functionals have been developed that can be used for a given system.<sup>4</sup>

One of the simplest ways of incorporating electron correlation formally in the system is the Møller-Plesset perturbation theory<sup>1</sup>. The electron correlation is incorporated as a perturbation to the Hartree-Fock Hamiltonian. The new Hamiltonian is given as,

$$\hat{H} = \hat{H}_0 + \lambda \hat{P} \quad (1.20)$$

where,  $\hat{H}_0$  is the Hartree-Fock Hamiltonian,  $\hat{P}$  is the perturbation, and  $\lambda$  is a dimensionless parameter that controls the amount of perturbation. The exact wavefunction and energy can be

written as,

$$\psi = \psi_0 + \lambda\psi^{(1)} + \lambda^2\psi^{(2)} + \lambda^3\psi^{(3)} + \dots \quad (1.21)$$

$$E = E^{(0)} + \lambda E^{(1)} + \lambda^2 E^{(2)} + \lambda^3 E^{(3)} + \dots \quad (1.22)$$

where,  $\psi_0$  and  $E^{(0)}$  are the wave function and energy obtained using HF method,  $\psi^{(1)}$ ,  $\psi^{(2)}$  and  $\psi^{(3)}$  are the first, second and third order corrections to the wavefunction and  $E^{(1)}$ ,  $E^{(2)}$ , and  $E^{(3)}$  are first, second, and third order corrections to the energy. Equations 1.20, 1.21 and 1.22 are substituted in the Schrödinger equation and equating the terms of like-orders in  $\lambda$ 's, one obtains correction to the energies and wavefunctions. It can be shown that for the ground state

$$E_0^{(0)} + E_0^{(1)} = E_{HF} \text{ and}$$

$$E_0^{(2)} = \sum_{m \neq 0} \frac{|\langle \psi_m^{(0)} | \hat{H}' | \psi_0^{(0)} \rangle|^2}{E_0^{(0)} - E_m^{(0)}} \quad (1.23)$$

MP2 method that includes  $E^{(2)}$  is the simplest alternative to configuration interaction methods and is widely used to account for electron correlation in medium-sized systems. It is important to note that MP2 method is size consistent unlike configuration interaction methods. However, MP2 method does not follow variational principle and hence can give energies below the true energy of the system.

Depending on the nature of the system, these different approximate methods are used to solve for the energy and wavefunction of a system. The initial wavefunction of the system is written as the linear combination of basis functions commonly known as basis set. A variety of basis sets are available for the constructions of the initial wavefunction for the doing the calculations. In the past, *Slater-type orbitals* (STOs) were used to define the wave function and have the following form,

$$\phi = N x^i y^j z^k e^{-\zeta(r-\mathbf{R})} \quad (1.24)$$

where,  $N$  is the normalization constant and  $\mathbf{R}$  is the position vector of the nucleus where the function is centered and  $\zeta$  is the exponent. For every STO for a given element, the value of  $\zeta$

is obtained by minimizing the atomic energy with respect to  $\zeta$ . Irrespective of the chemical environment, these values of  $\zeta$  are used for every atom of that element for doing the calculation. STO basis functions was popular since it mimics the exact solution of one-electron atom. But exact orbitals for other atoms are not hydrogen-like but are similar to hydrogen-like orbitals.

Basis sets developed by Boys and coworkers and popularized by Pople are very popular in quantum chemical calculations that uses *Gaussian-type orbitals* (GTOs). The form of GTO is as follows,

$$\phi = N x^i y^j z^k e^{-\alpha(r-\mathbf{R})^2} \quad (1.25)$$

Since the shape of GTOs differ from STOs specially at the nucleus (cusp-like shape), multiple GTOs are used to mimic each STO. Each of these individual GTO is known as primitive gaussian and multiple GTOs is known as contracted gaussian.

The minimum basis set is defined as one basis function per fully or partially occupied orbital in the atom. This is known as *single zeta* (SZ) basis set. SZ basis sets are usually inadequate, so *double zeta* (DZ) and *triple zeta* (TZ) basis sets are employed for the calculations. Since core electrons do not take part in chemical reactions, they were described using SZ basis set and valence electrons were described by using DZ or TZ basis functions. This kind of basis sets are known as *split-valence* (SV) basis sets. Popular examples of SV basis sets are Pople's and Dunning's basis sets which are extensively used for doing calculations. To describe the polarization of electron density of the atoms in the molecules, additional functions known as *polarization* functions are added to the basis set. For molecules with negative charge or lone pairs, *diffuse* functions are added to the basis set to allow the electron density to expand.

To understand the thermochemistry of a chemical reaction, various thermodynamics quantities are calculated using statistical mechanics. By calculating the partition functions for vibrational, translational, rotational and electronic part, one can calculate the thermodynamic properties of the system such as entropy ( $S$ ), Gibbs free energy ( $G$ ), etc. To assess the thermodynamic feasibility of a pathway in a chemical reaction, Gibbs free energy ( $G$ ) is computed

along the reaction pathway using,

$$G = H - TS \quad (1.26)$$

where,  $T$  is the temperature,  $S$  is the total entropic contribution from electronic, vibrational, rotational and translation degree of freedoms as,

$$S = S_{\text{total}} = S_{\text{elec}} + S_{\text{vib}} + S_{\text{rot}} + S_{\text{trans}} \quad (1.27)$$

and  $H$  is calculated as,

$$H = E_{\text{tot}} + k_B T \quad (1.28)$$

where,  $E_{\text{tot}}$  is the total correction to the internal thermal energy as,

$$E_{\text{tot}} = E_{\text{elec}} + E_{\text{vib}} + E_{\text{rot}} + E_{\text{trans}} \quad (1.29)$$

In going from reactions to products, a large negative change in free energy indicates that the pathway is spontaneous.

**(ii) Dynamics of various processes :** In the previous section, various approximate methods were discussed which can be used to compute different static properties of the system that do not change with time. For example, in a chemical reaction, different pathways can be mapped by calculating the potential energy profile. The reaction can proceed through any of these pathways but the real system is dynamical in nature and changes with time. So, to understand the dynamical pathways followed in the reaction, the system needs to be evolved with time. This can be achieved by solving equations of motion (EOM) in two ways: by using quantum mechanics or by using classical mechanics.

In quantum mechanics, the system is defined by the wavefunction  $\Psi(R, t)$  whose evolution with time is calculated by integrating the time-dependent Schrödinger equation<sup>1</sup> given as,

$$i\hbar \frac{\partial}{\partial t} \Psi(R, t) = \hat{H} \Psi(R, t) \quad (1.30)$$

However, quantum dynamical simulations are computationally very expensive and difficult to handle more than 4-5 atoms.

An alternative to quantum dynamics is evolving the system using classical mechanics by solving Newton's equations of motion,

$$F_i = m_i a_i \quad (1.31)$$

$$F_i = m_i \frac{d^2 R_i}{dt^2} = - \frac{\partial V(R)}{\partial R_i} \quad (1.32)$$

where,  $F_i$ ,  $m_i$  and  $a_i$  are the force, mass and acceleration of the  $i_{\text{th}}$  particle of the system. These equations are solved numerically which result in  $R_i(t)$  at each time step. The coordinates  $R_i(t)$  and its conjugate momentum  $p_i(t)$  together is called a trajectory.

In the work presented here, classical trajectory simulations were performed to understand the mechanism and dynamics of chemical reactions. In this approach, an ensemble of trajectories are initiated and integrated. The initial coordinates and momenta for each trajectory is obtained by using either microcanonical normal mode sampling or by sampling a Boltzmann distribution of internal energies at a particular temperature.<sup>5</sup> The trajectories are integrated numerically using velocity-Verlet algorithm<sup>6</sup> with a small time step.

Integration of the system requires the knowledge of the potential energy surface, usually represented in an analytical form  $V(R_1, R_2, \dots, R_{3N-6})$ , where  $R_i$ 's are the internal coordinates of the system. For systems with large number of atoms, an accurate analytical description of the potential energy of the system is extremely difficult. For these cases, *ab initio* trajectory simulations<sup>5</sup> were employed where at every step of integration, the time-independent electronic Schrödinger equation is solved to compute the energy and forces of the system on-the-fly at a particular level of theory.

## DYNAMICS OF PROTONATION AND LITHIATION OF FERROCENE

### 2.1 Introduction

**E**lectrophilic aromatic substitution reactions<sup>7</sup> are important class of reactions in which a group attached to the aromatic system is replaced by an incoming electrophile. Some of these aromatic reactions include Friedel-Crafts reaction, halogenation and nitration. Using this approach, many aromatic derivatives have been synthesized that are used for various applications.

In 1951, Pauson and Kealy<sup>8</sup> accidentally discovered ferrocene, the first metallocene that gave way to the whole era of organometallic chemistry. In ferrocene, Fe metal is in +2 oxidation state and is sandwiched between the two cyclopentadienyl (Cp) rings. It was found that ferrocene follows 18 electron rule which makes it an aromatic system and undergoes reactions characteristics of aromatic compounds. From the experimental studies conducted by Cunningham and coworkers,<sup>9-11</sup> it has been proposed that hard electrophiles attack ferrocene through *exo*

pathway in which the incoming electrophile attacks on the top of the Cp ring. On the other hand, soft electrophiles attack ferrocene through the *endo* pathway in which electrophile first bonds with Fe metal and then attacks the Cp ring on its *endo* face. Figure 2.1 shows both *exo* and *endo* attacks on the ferrocene moiety. A problem arose when the incoming electrophile is  $H^+$ . Since both the *exo* and *endo* pathways would result in the formation of the same intermediate that can not be distinguished. Thus, experimental studies could not provide conclusive evidence as to which pathway is followed in the reaction between ferrocene and  $H^+$ .

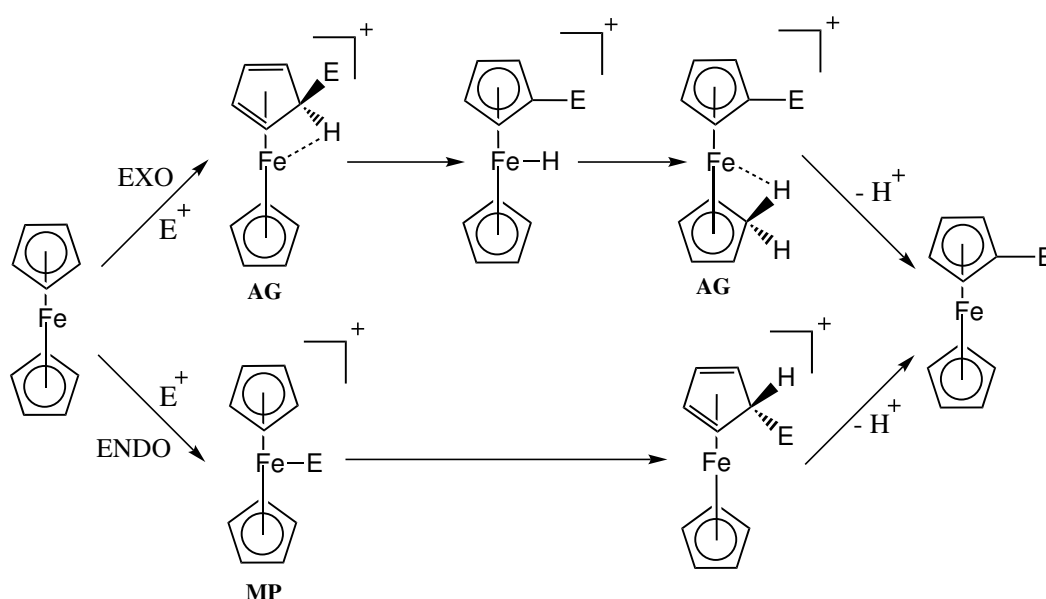


Figure 2.1: *Exo* and *endo* pathways followed by electrophiles.

Several experimental and theoretical studies have been carried out to investigate the mechanism of protonation of ferrocene. Curphey *et al*<sup>12</sup> conducted NMR experiments in boron trifluoride hydrate that showed that only metal-protonated isomer is observed in the solution. Gas phase deuteration experiments by Meot-Ner<sup>13</sup> revealed that the incoming  $H^+/D^+$  attaches to either the Cp ring or Fe atom but without exchange of H atom of the Cp ring. On the other hand, experiments conducted in deuterated acidic media suggested that *exo* pathway is followed in the reaction.<sup>14</sup> The same study also suggested the existence of a rapid equilibrium between

two protonated forms of ferrocene, the ring protonated and metal-protonated forms. IR spectra of protonated ferrocene indicated the presence of Fe-H stretch and Cp-Fe-H deformation.<sup>15</sup> Gas phase study of protonation of ferrocene conducted by Hop *et al*<sup>16</sup> indicated that H<sup>+</sup> switches from one Cp ring to another by a similar mechanism proposed by Cunningham<sup>9-11</sup> for electrophilic substitution of ferrocene. Their experiments revealed that the structure in which the added proton is bound to one of the Cp ring in an agostic fashion, plays an important role in the gas-phase behaviour of protonated ferrocene. The experimental studies conducted thus far could not conclusively establish the preference of *exo* and *endo* attack in the protonation of ferrocene.

The mechanism of the protonation was also investigated computationally. One of the first attempts to predict the structure of protonated ferrocene was done by McKee<sup>17</sup> using Hartree-Fock (HF) and Møller-Plesset second order (MP2) methods with effective core potential (ECP) for Fe and 6-31G\* for other atoms. The study suggested that the protonated ferrocene can exist in two isomers. At the HF level, the metal-protonated form was preferred whereas, MP2 method preferred the agostic form (**2b**), both with considerable stabilization energy, suggesting a need for the accurate treatment of electron correlation. Weber and coworkers<sup>18</sup> performed density functional theory (DFT) studies using BPW91 functional and found out the existence of two minima with very small energy difference between ring protonated and metal-protonated forms. The closely lying energies of these two isomers and a transition state corresponding to the proton transfer suggested rapid equilibrium between the two forms. Bühl and coworkers<sup>19</sup> conducted an extensive study that showed that the structures are very sensitive to various DFT functionals and basis functions because of the shallow nature of the PES. It can be seen that B3LYP suggests that the agostic form is favored over the metal-protonated form by an energy difference of ca 2-4 kcal/mol for different basis sets.<sup>19</sup> BLYP also shows similar tendency, but with a lower stabilization energy. The coupled-cluster level of theory showed that ring protonated isomer is favourable over metal-protonated isomer by 2 kcal/mol, which indicated

that *exo* pathway should be the favourable pathway in the protonation of ferrocene<sup>20</sup>. Figure 2.2 shows the comparison of the relative energies between the metal-protonated and agostic forms of protonated ferrocene at different levels of theory. *Ab initio* molecular dynamical studies were performed by Bühl and coworkers<sup>19</sup> using BP86 and B3LYP functionals and compared with the equilibrium chemical shift values of <sup>13</sup>C, <sup>1</sup>H and <sup>57</sup>Fe. It was observed that ring protonated isomer was more preferred but computed NMR chemical shifts of <sup>1</sup>H and <sup>57</sup>Fe were found to be close to the experimental chemical shifts of ring-protonated and metal-protonated isomers, respectively.

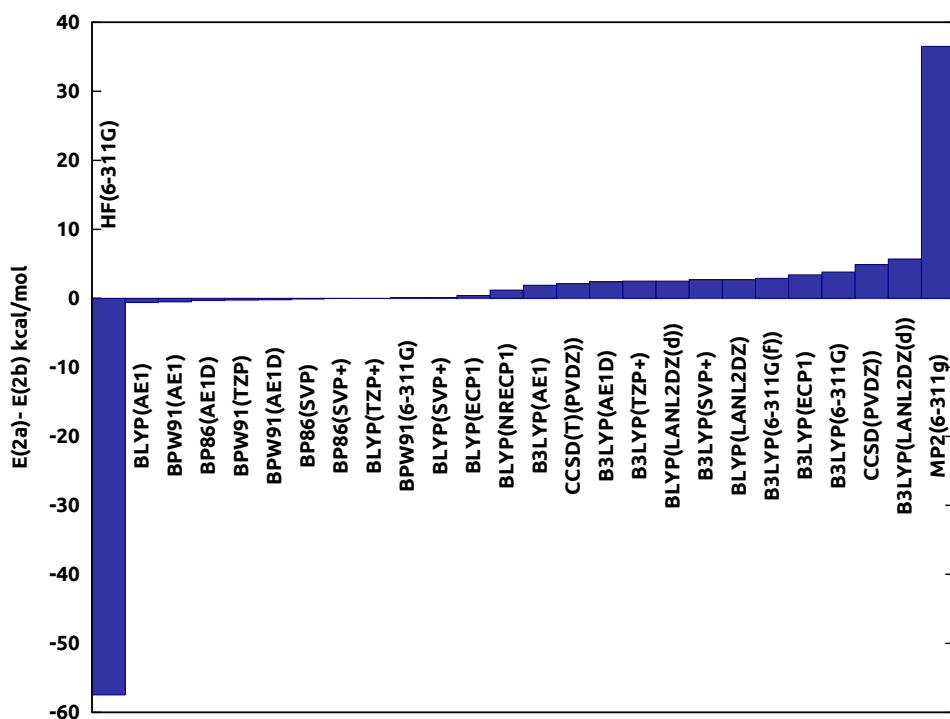


Figure 2.2: Comparison of energy differences between metal-protonated and agostic structures at different levels of theory.

The various computational and experimental studies suggested the importance of ring-

protonated isomer in the reaction mechanism but the actual mechanism (*exo* or *endo*) is still not known unambiguously. It is also interesting to study the mechanism of the lithiation of ferrocene, the next  $E^+$  in the periodic table.  $Li^+$  is a hard electrophile and can be expected to attack in the *exo* fashion. In literature, it is known that  $Li^+$  interacts very strongly with neutral chemical species and gained huge attention since it can form *planetary systems*.<sup>21,22</sup> Abboud *et al*<sup>22</sup> studied  $P_4-Li^+$  system and found that  $Li^+$  complexes with neutral  $P_4$  through paths resembling orbits, revolving around the  $P_4$  moiety. In addition, lithiation of ferrocenyl groups is the first step in the synthesis of di- or tri-substituted ferrocene<sup>23</sup>. Since ferrocene has two binding sites: Cp ring and Fe metal, it is of fundamental interest to investigate the mechanism of the lithiation of ferrocene.

Here, a detailed DFT and *ab initio* classical dynamics study of the protonation and lithiation of ferrocene is conducted to understand the atomic-level mechanism followed in these reactions.

## 2.2 Methodology

Density functional theory (DFT) functionals B3LYP and BPW91 with Dunning's DZVP basis set and Pople's 6-311++G\*\* basis set was used to map the potential energy profile for both protonated and lithiated ferrocene. The nature of a stationary point on the potential energy profile as an intermediate or a transition state was characterized by computing harmonic vibrational frequencies. Intrinsic reaction coordinate (IRC) calculations were performed to connect all the transition states to their respective adjacent minima. All the electronic structure calculations were carried out using Gaussian 09<sup>24</sup> and NWChem<sup>25</sup> software packages.

To understand the initial attack of both the electrophiles ( $H^+$  and  $Li^+$ ) on ferrocene, *ab initio* classical trajectory simulations were performed using VENUS/NWChem software package<sup>26</sup> at B3LYP/DZVP level of theory as this method gave results closer to CCSD(T)/pVDZ. Preliminary calculations were performed earlier.<sup>27</sup> Both unimolecular and bimolecular dynamical trajectories were carried out to understand the atomic-level mechanisms. The initial coordi-

nates and their conjugate momenta were chosen by employing using quasi-classical sampling procedure. The trajectories were numerically integrated using velocity-Verlet algorithm for 0.5-1 ps. A time step of 0.5 fs was used for protonation reaction, while in case of lithiation, 0.5 and 0.3 fs were used as for timesteps for unimolecular and bimolecular dynamical simulations respectively.

## 2.3 Results and Discussions

### 2.3.1 Protonation of ferrocene

#### 2.3.1.1 Potential energy profile

The potential energy profile for the protonated ferrocene was mapped using B3LYP/DZVP, B3LYP/6-311++G\*\* and BPW91/6-311++G\*\* levels of theory. Figure 2.3 shows the molecular electrostatic potential map for the iso-value of -0.013 au. It is evident that the negative potential is present above and below the Cp ring and also around Fe atom, which suggest the possible binding sites of electrophiles on ferrocene moiety. The stationary points on the potential energy surface of protonated ferrocene are calculated using B3LYP/DZVP, B3LYP/6-311++G\*\* and

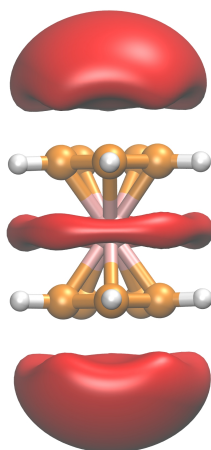


Figure 2.3: Electrostatic potential map (in a.u.) of ferrocene for the iso-value of -0.013.

Table 2.1: Comparison of structural parameters and relative energies of ferrocene and its protonated forms

	MP			AG			Ferrocene		
	BPW91 <sup>a</sup>	B3LYP <sup>a</sup>	B3LYP <sup>b</sup>	BPW91 <sup>a</sup>	B3LYP <sup>a</sup>	B3LYP <sup>b</sup>	BPW91 <sup>a</sup>	B3LYP <sup>a</sup>	B3LYP <sup>b</sup>
Fe-H <sup>+</sup> (Å)	1.50	1.48	1.49	1.58	1.67	1.70	-	-	-
C-H <sup>+</sup> (Å)	1.87	1.87	1.88	1.36	1.23	1.22	-	-	-
Fe-X <sub>1</sub> (Å) <sup>c</sup>	1.68	1.71	1.70	1.67	1.71	1.70	1.64	1.68	1.67
Fe-X <sub>2</sub> (Å) <sup>d</sup>	1.68	1.71	1.70	1.68	1.70	1.69	1.64	1.68	1.67
X <sub>1</sub> -Fe-X <sub>2</sub> (°)	167	167	167	169	169	169	180	180	180
X <sub>1</sub> -Fe-H <sup>+</sup> (°)	97	97	97	80	74	74	-	-	-
C-H(Å)	-	-	-	-	-	-	1.09	1.08	1.08
Fe-C(Å)	-	-	-	-	-	-	2.05	2.08	2.07
Structure	eclipsed								
$\Delta E^e$ (kcal/mol)	-0.03	2.60	2.58	0	0	0	-	-	-

<sup>a</sup>6-311++G\*\* basis set. <sup>b</sup>DZVP basis set. <sup>c</sup>X<sub>1</sub> is the center of the Cp ring which is closer to the H<sup>+</sup>. <sup>d</sup>X<sub>2</sub> is the center of the Cp ring which is farther from the H<sup>+</sup>. <sup>e</sup> $\Delta E = E_{MP} - E_{AG}$  at different levels of theory.

BPW91/6-311++G\*\* levels of theory. The important geometrical parameters and their energies are given in Tables 2.1 and 2.2.

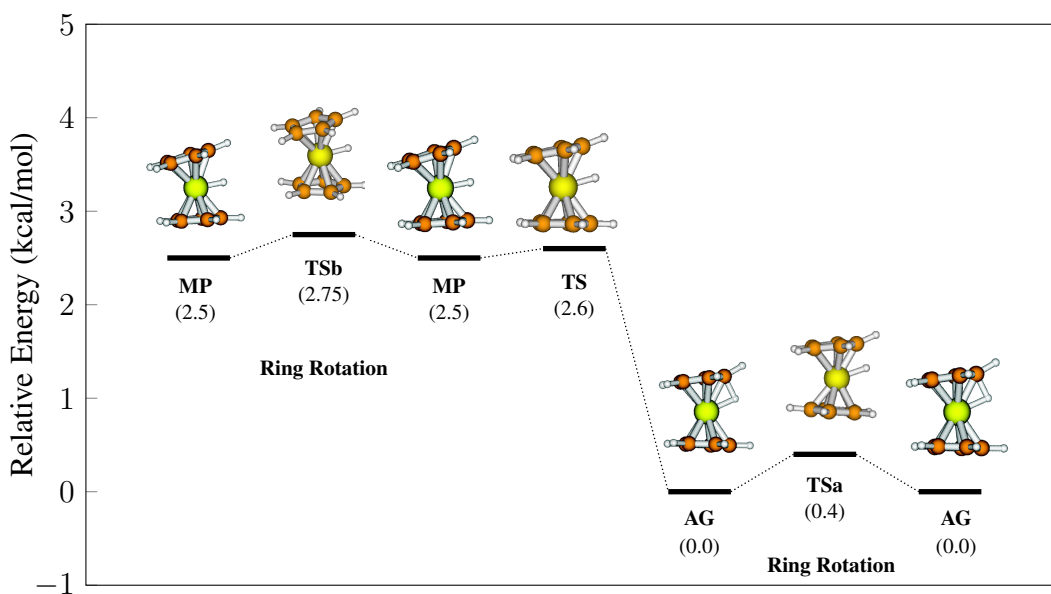


Figure 2.4: Potential energy profile depicting the different isomers of the protonated ferrocene obtained at the B3LYP/DZVP level.

Table 2.2: Comparison of structural parameters and relative energies of three different transition states

	T <sub>Sa</sub>			T <sub>S</sub>			T <sub>Sc</sub>			T <sub>Sb</sub> <sup>c</sup>
	BPW91 <sup>a</sup>	B3LYP <sup>a</sup>	B3LYP <sup>b</sup>	BPW91 <sup>a</sup>	B3LYP <sup>a</sup>	B3LYP <sup>b</sup>	BPW91 <sup>a</sup>	B3LYP <sup>a</sup>	B3LYP <sup>b</sup>	B3LYP <sup>b</sup>
Im. Freq (cm <sup>-1</sup> )	44i	29i	30i	290i	144i	308i	653i	742i	848i	48i
Fe-H <sup>+</sup> (Å)	1.59	1.68	1.71	1.52	1.48	1.50	-	-	-	1.48
C-H <sup>+</sup> (Å)	1.34	1.22	1.21	1.57	1.80	1.70	1.29	1.28	1.29	1.91
Fe-X <sub>1</sub> (Å) <sup>d</sup>	1.67	1.71	1.70	1.67	1.70	1.69	1.59	1.64	1.62	1.71
Fe-X <sub>2</sub> (Å) <sup>e</sup>	1.68	1.71	1.69	1.68	1.71	1.70	1.67	1.70	1.68	1.70
X <sub>1</sub> -Fe-X <sub>2</sub> (°)	168	169	169	168	167	167	178	178	178	159
X <sub>1</sub> -Fe-H <sup>+</sup> (°)	79	74	74	87	94	91	25	25	25	98
Structure	staggered	staggered	staggered	eclipsed	eclipsed	eclipsed	eclipsed	eclipsed	eclipsed	staggered
$\Delta E^f$ (kcal/mol)	0.85	0.37	0.31	0.13	2.60	2.63	20.1	20.09	20.29	5.16

<sup>a</sup>6-311++G\*\* basis set. <sup>b</sup>DZVP basis set. <sup>c</sup>T<sub>Sc</sub> could not be located for B3LYP/6-311++g\*\* and BPW91/6-311++g\*\* levels of theory. <sup>d</sup>X<sub>1</sub> is the center of the Cp ring which is closer to the H<sup>+</sup>.

<sup>e</sup>X<sub>2</sub> is the center of the Cp ring which is farther from the H<sup>+</sup>. <sup>f</sup>Energies relative to **AG** at different levels of theory.

Figure 2.4 shows the potential energy profile for the protonated ferrocene using B3LYP/DZVP level of theory. We can see that B3LYP/DZVP level of theory gives energies comparable to CCSD(T)/pVDZ. Two isomers exist on the profile: the agostic (**AG**) and metal protonated (**MP**) with **AG** is more stable than **MP** by 2.58 kcal/mol. **AG** can isomerize to **MP** via the transition state **TS** with a barrier of 2.63 kcal/mol.

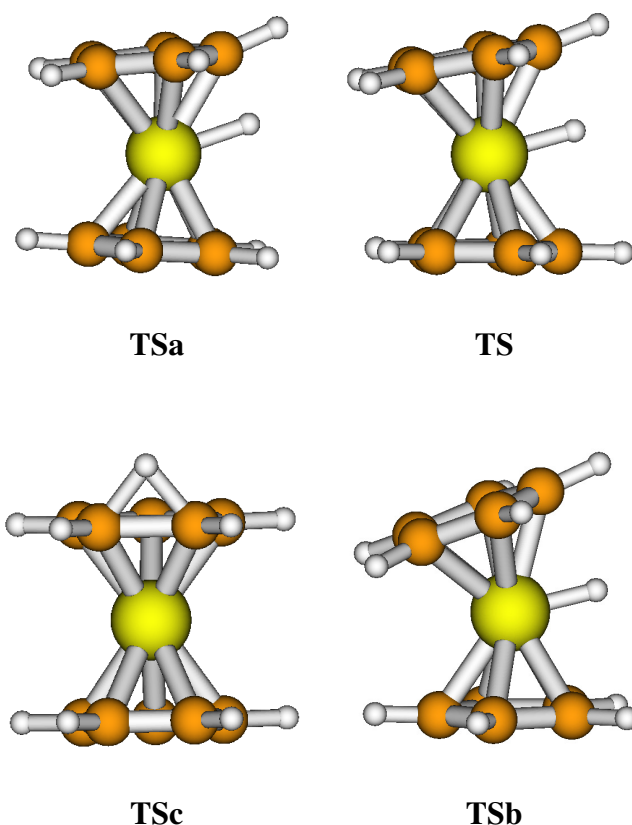


Figure 2.5: Structures of all the transition states obtained for protonated ferrocene.

$\text{H}^+$  in **AG** forms a three-centered bond with C atom of Cp ring and Fe atom. Fe- $\text{H}^+$  bond distance changes from 1.7 Å in **AG** to 1.49 Å in **MP**. The angle formed between center of the Cp ring ( $X_1$ ), Fe atom and  $\text{H}^+$  ( $\angle X_1\text{-Fe-H}^+$ ) changes from 74° in **AG** to 97° in **MP**. The metal-protonated form can isomerize to another isoenergetic form (**MP**) through a transition state **TSa** with a barrier of 0.25 kcal/mol. In a similar way, the agostic form can isomerize to another isoenergetic form (**AG**) by rotation of the Cp rings about an axis passing through their

center of masses via a transition state **TSb** with a barrier of just 0.4 kcal/mol. In **AG**, the exo H atom can also hop to the adjacent C atom of the Cp ring via a high barrier transition state **TSc** which is 20.29 kcal/mol above **AG**. Figure 2.5 shows the structure of all the transition states of protonated ferrocene.

To understand the atomic-level mechanism of protonation of ferrocene, classical trajectory simulations were performed using B3LYP/DZVP level of theory.

### 2.3.1.2 Dynamics of protonated ferrocene

To understand the isomerization dynamics of protonated ferrocene, trajectories were initiated from both the isomers: **AG** and **MP**. Vibrational and rotational energies were sampled using Boltzmann distribution at 300 K. The trajectories were integrated for 1.5-2 ps using a time step of 0.5 fs. 50 trajectories from **AG** and 45 trajectories from **MP** were computed.

Out of 50 trajectories initiated from **AG**, 41 showed H<sup>+</sup> hopping between the two Cp rings via the **MP** isomer. The remaining 9 were trapped in the **AG** isomer for 1.5 ps of integration time. In a similar way, 39 out of 45 trajectories initiated from **MP** showed rapid isomerization between **AG** and **MP** isomers, while rest 7 trajectories were trapped in agostic isomer **AG**. It was found that none of the trajectories were trapped in the metal-protonated isomer **MP**. Rotation of both the Cp rings relative to each other was observed in most of the trajectories. H<sup>+</sup> was found to be very mobile and H<sup>+</sup> hopping from one C atom to another on the same Cp ring was also observed in 3 trajectories initiated at **AG** and 11 trajectories initiated at **MP**.

To investigate the time the system spends in the **AG** and **MP** isomers during the trajectory, the lifetime of the isomers were calculated by following X<sub>1</sub>-Fe-H<sup>+</sup> angle as a function of time for all the trajectories, where X<sub>1</sub> is the center of the Cp ring. It should be noted that the equilibrium structure X<sub>1</sub>-Fe-H<sup>+</sup> angle for **AG**, **MP** and **TS** connecting the two forms are 74.0, 96.7 and 90.8, respectively. Figure 2.6 shows the lifetime distributions of **AG** and **MP** isomers for both sets of trajectories initiated from **AG** and **MP** minima. For the set of trajectories initiated at **MP** minimum, the average lifetime of **AG** was found to be 186 fs, where that for

**MP** it was found 16 fs. On the other hand, the average lifetimes for **AG** and **MP** isomers were computed to be 167 and 17 fs, respectively. This indicates that  $H^+$  spends most of the time being in **AG** isomer than in **MP** isomer. Large lifetimes of 1.5 ps for **AG** isomer corresponds to the trajectories that were trapped in **AG** minimum. The exponential decay behaviour of the lifetimes indicate statistical behaviour of the isomers.

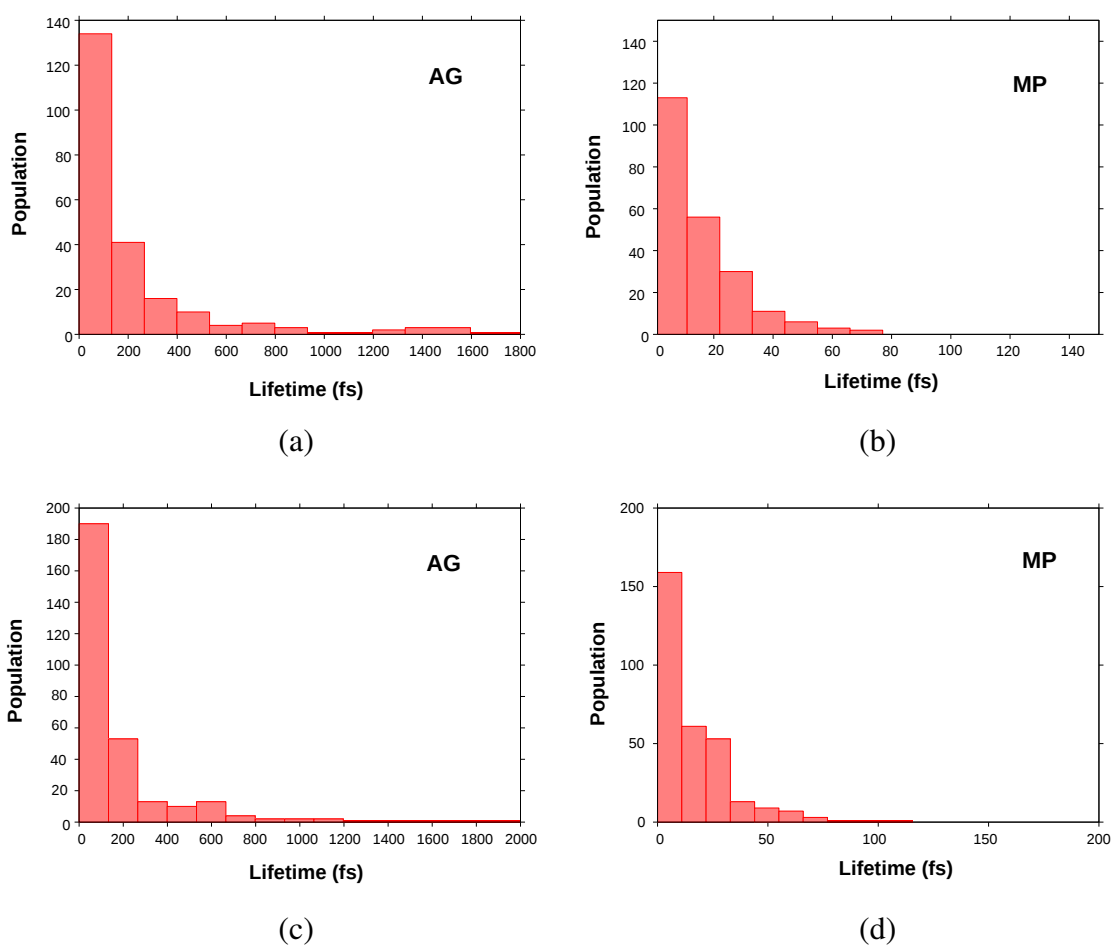


Figure 2.6: Population vs lifetime plot for **AG** and **MP** isomers for trajectories initiated at **AG** (a and b) and **MP** (c and d), respectively.

### 2.3.1.3 Dynamics of protonation of ferrocene

The trajectories initiated at the agostic and metal protonated minima gave information about the rich dynamical events that happen when  $H^+$  is already bound to the ferrocene moiety. But to understand the actual mechanism of the protonation, it is of interest to focus on the initial attack of  $H^+$  on ferrocene to understand whether the mechanism followed by the reaction is *exo* or *endo* in nature. To this end, bimolecular collisions were carried out in which  $H^+$  and ferrocene were initially separated by 8 Å. However, the trajectories exhibited SCF convergence issues due to the instability of the electron densities. So, to mimic bimolecular collisions between  $H^+$  and ferrocene, the trajectories were initiated from three geometries as shown in Figure 2.7. These three geometries were obtained by partial optimization fixing (i) the *endo* C–H bond distance at 5 Å in **AG** isomer, (ii)  $H^+$  on top of Cp ring with Fe–H bond distance at 6.6 Å and  $\angle X_1\text{-Fe-H}^+ = 4.6^\circ$  and (iii) Fe–H bond distance at 7.48 Å and  $\angle X_1\text{-Fe-H}^+ = 41.8^\circ$ .

182 trajectories were initiated from these three geometries using Boltzmann sampling of vibrational and rotational energies at 300 K. These trajectories were integrated for 0.5-1 ps. 80 out of 182 trajectories initiated resulted in the protonation of ferrocene. Figure 2.8(a) shows the plot of initial position of  $H^+$  with respect to ferrocene for 80 trajectories. In Figure 2.8(a), blue circles (●) represent  $H^+$  orientations that resulted in *exo* attack and red triangles (►) represent  $H^+$  initial orientations that resulted in *endo* attack.

These trajectories showed rich dynamical events and  $H^+$  was found out to be very mobile. Out of 80 trajectories, 58 trajectories followed *exo* pathway in which  $H^+$  attacked ferrocene moiety on top of the ring. In the remaining 22 trajectories,  $H^+$  followed *endo* pathway where the initial attack of  $H^+$  was on Fe metal. Figure 2.8(b) shows representative trajectories for the different pathways of the reaction. In Figure 2.8(b), the black squares (□) and the blue circles (○) represent trajectories exhibiting *exo* attack and the red triangles (►) represent a trajectory exhibiting *endo* attack. It was observed that in 35 out of 58 *exo* trajectories,  $H^+$  hops on different C atoms of the same Cp ring. In 23 out of these 35 trajectories, *endo*  $H^+$

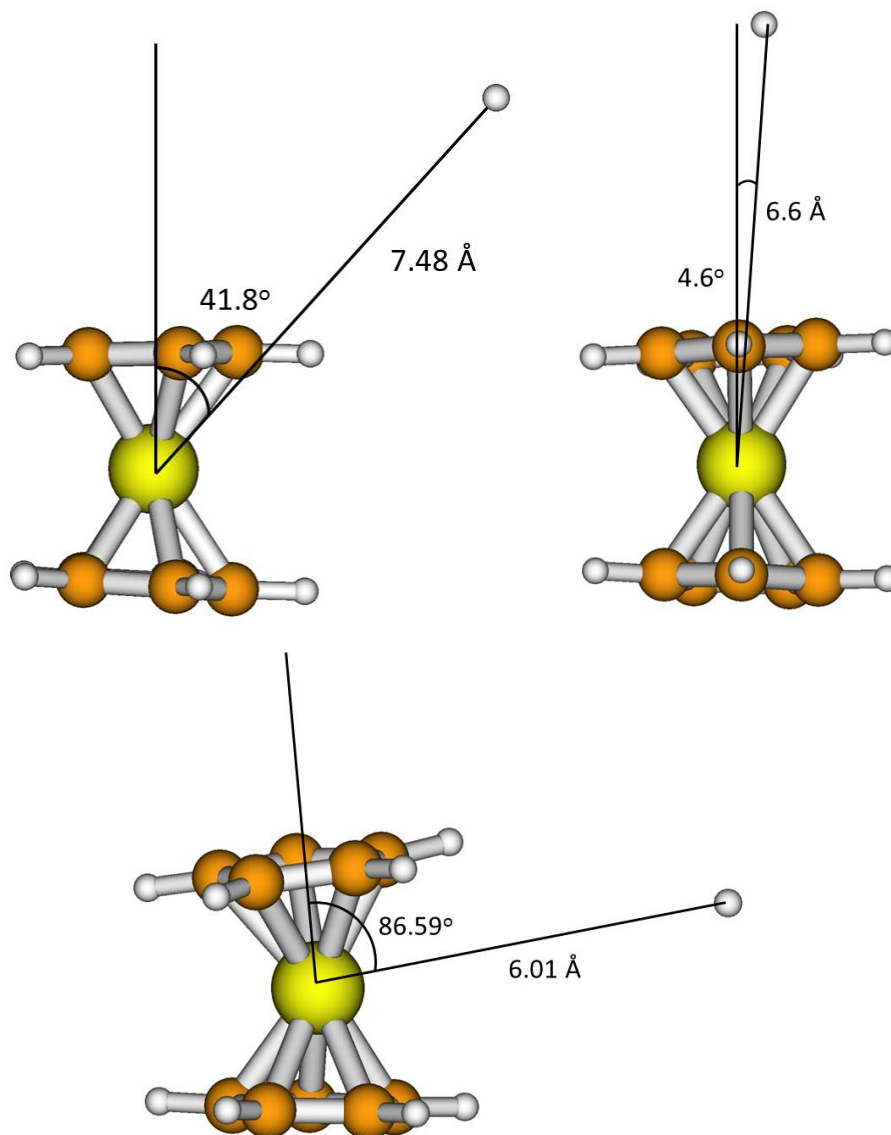


Figure 2.7: Partially optimized geometries to mimic bimolecular collision between H<sup>+</sup> and ferrocene.

is transferred to the other Cp ring through **MP** after the hopping of H<sup>+</sup> on the same Cp ring, while, in remaining 9 trajectories, H<sup>+</sup> hops on the different C atom of the same Cp ring but stayed in **AG** form. In another 19 out of 58 *exo* trajectories, the *endo* H<sup>+</sup> is transferred to the other Cp ring via **MP** immediately after the attack. 4 trajectories out of 58 were trapped in **AG** form for 1.5 ps in which H<sup>+</sup> hopping on the different C atoms of the same Cp ring was not observed.

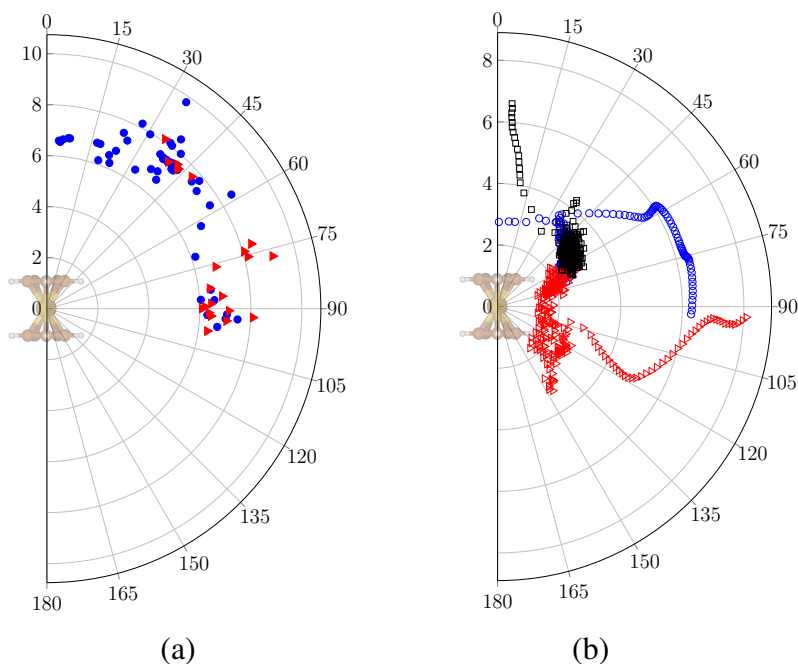


Figure 2.8: Plots of  $\angle X_1\text{-Fe-H}(\circ)$  vs Fe-H distance( $\text{\AA}$ ) in polar coordinates. (a) Initial orientation of  $\text{H}^+$  in 80 trajectories is shown. (b) 3 representative trajectories showing different attacks.

As mentioned above, 22 out of 80 trajectories followed *endo* pathway. It was observed that all the trajectories exhibited  $\text{H}^+$  hopping between the two Cp rings through the formation of **MP**. These trajectories showed similar rich dynamical behaviour as that of the trajectories that followed *exo* pathway and a rapid isomerization between **AG** and **MP** was observed as shown in Figure 2.9. Interestingly, none of the trajectories were found to be trapped in the **MP** minimum. *Ab initio* classical trajectory simulations revealed that protonation of ferrocene can happen via both *exo* and *endo* pathways with *exo* being the major one. Of interest here is to see that if the initial orientation of the incoming  $\text{H}^+$  has any effect on the mechanism that would be followed in the reaction. Figure 2.8(a) shows the polar plot of  $\angle X_1\text{-Fe-H}(\circ)$  vs Fe-H distance ( $\text{\AA}$ ) for all the 80 trajectories. This shows the initial orientation of the incoming  $\text{H}^+$  with respect to ferrocene moiety. It was clearly seen that trajectories that followed *endo* pathway are the ones in which  $\angle X_1\text{-Fe-H}^+$  was in between  $45^\circ\text{--}105^\circ$ , indicating orientational preference for *endo* mechanism. On the other hand, the trajectories that followed *exo* mechanism covers full range

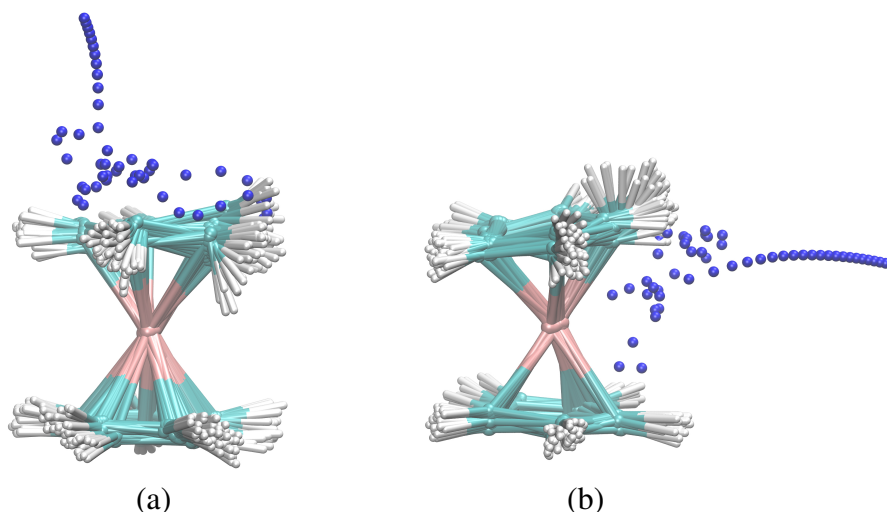


Figure 2.9: Superimposed frames for representative trajectories exhibiting (a) *exo* attack and  $\text{H}^+$  hopping on the Cp ring and (b) *endo* attack and  $\text{H}^+$  motion between the two Cp rings. The incoming  $\text{H}^+$  is shown in blue color.

of  $\angle\text{X}_1\text{-Fe-H}^+$  showing no preference for initial orientation of  $\text{H}^+$  with respect to ferrocene.

### 2.3.2 Lithiation of ferrocene

After understanding mechanism of the protonation of ferrocene, we turned our attention to investigate the mechanism of the next electrophile ( $\text{Li}^+$ ) in the periodic table. Few DFT studies have been carried out to understand the interaction between  $\text{Li}^+$  cation and ferrocene moiety<sup>21,28</sup>. Interestingly, it was observed that the lithiation of ferrocene results in a *planetary system*, that refers to complexes between  $\text{Li}^+$  and Fe atom where the  $\text{Li}^+$  cation is expected to have closed, thermally accessible paths resembling orbits, revolving around the central Fe atom<sup>21,28</sup>. Figure 2.10 shows the orbit of  $\text{Li}^+$  cation around Fe atom. Lithiation of aromatic compounds is a well known chemical reaction routinely done in the laboratory for synthesizing different substituted ferrocene. In this reaction, Lithium cation ( $\text{Li}^+$ ) attacks the aromatic ring. Now, if we consider the aromatic compound to be ferrocene,  $\text{Li}^+$  being a hard electrophile, is expected to undergo *exo* mechanism according to the model proposed by Cunningham and coworkers. Figure 2.3

shows the MEP of neutral ferrocene moiety for the iso-value of 0.013 au. It shows the possible binding sites of  $\text{Li}^+$  cation on ferrocene in which the top of the Cp ring has more negative MEP value than the radial part around the Fe atom. This indicates that possibility of  $\text{Li}^+$  cation binding at the top of the Cp ring is more than the radial part around Fe atom.

Potential energy profile was mapped for the lithiated ferrocene at B3LYP/DZVP level of theory. Figure 2.11 shows the relative energy and optimized structures of various stationary points obtained. It was found that lithiated ferrocene can exist in two isomers: the most stable cation- $\pi$  complex (**CP**) and the metal-lithated complex (**ML**). In **CP**,  $\text{Li}^+$  cation sits on top of the Cp ring at a distance of 2.32 Å from all the five C atoms. **CP** can be converted to **ML** through the transition state **TSe** with a barrier of 23.62 kcal/mol. Here,  $\text{Li}^+$  cation lies in the plane of Cp ring in **TSe**. In **ML**, Fe- $\text{Li}^+$  bond distance is 2.6 Å, and  $\angle\text{C-X}_1\text{-Fe-Li}^+ = 44^\circ$  where  $\text{Li}^+$  is staggered with respect to closest C atoms of Cp ring. **ML** can inter convert to five symmetrical isoenergetic **ML** forms in which  $\text{Li}^+$  atom moves about the Fe atom. These five **ML** forms can inter convert among themselves through the transition state **TSf** with a barrier of 1.47 kcal/mol in which motion along the IRC represents a *planetary* kind of motion due to the revolution of

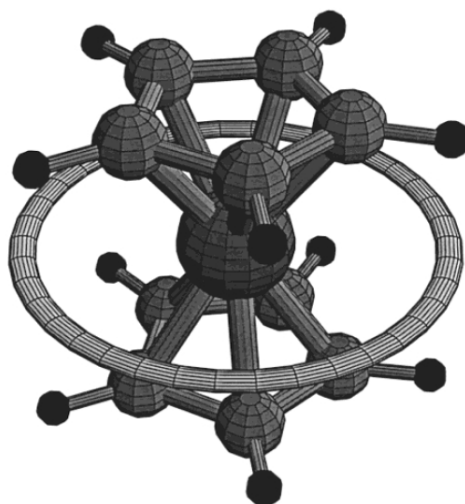


Figure 2.10: Orbit of  $\text{Li}^+$  cation around Ferrocene. Adapted with permission from Ref. [21]. Copyright 2001 American Chemical Society.

$\text{Li}^+$  about the Fe atom. It was observed that the **ML** isomer can also be converted to five more isoenergetic forms due to the relative rotation of the Cp rings through the transition state **TSg** having barrier of 1.03 kcal/mol.

To understand the intramolecular dynamics of lithiated ferrocene, *ab initio* classical trajectories were carried out starting from the transition states: **TSe** and **TSf**, on the potential energy surface.

### 2.3.2.1 Isomerization Dynamics of lithiated ferrocene

To understand the atomic-level mechanism of lithiated ferrocene, trajectories were initiated at transition states **TSe** and **TSf**. 25 trajectories were integrated for 1-1.5 ps from the transition state **TSf** which results in *planetary* motion of  $\text{Li}^+$  about Fe atom. Vibrational and rotational energies were sampled using Boltzmann distribution at 300 K. A time step of 0.5 fs was used to numerically integrate trajectories using velocity-Verlet algorithm. Out of the 25 trajectories, 7 trajectories showed planetary motion in which  $\text{Li}^+$  cation completes full circle by revolving about the Fe atom. None of these planetary trajectories showed relative Cp ring rotation. Figure

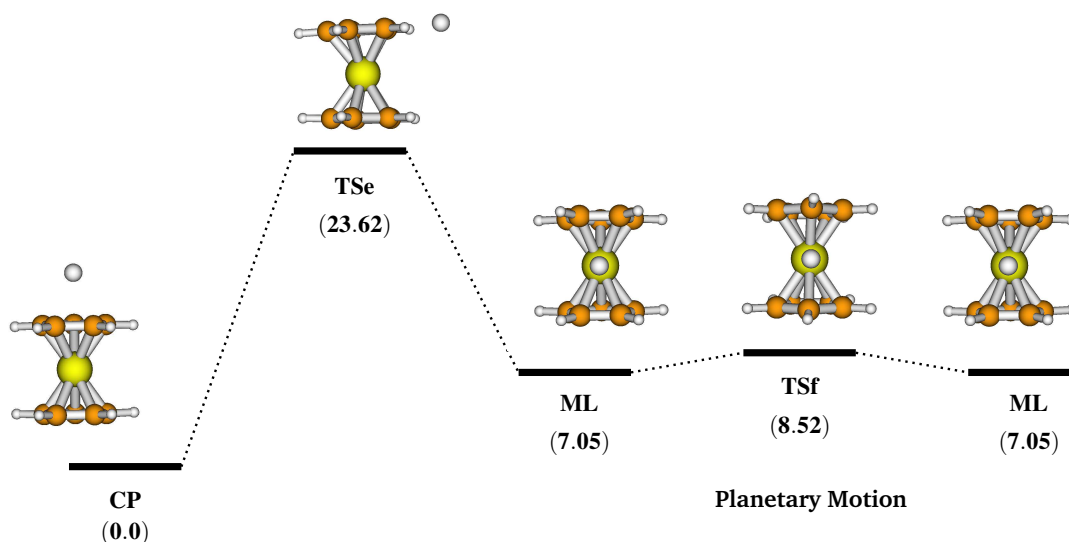


Figure 2.11: Energetic of lithiated ferrocene calculated at the B3LYP/DZVP level of theory.

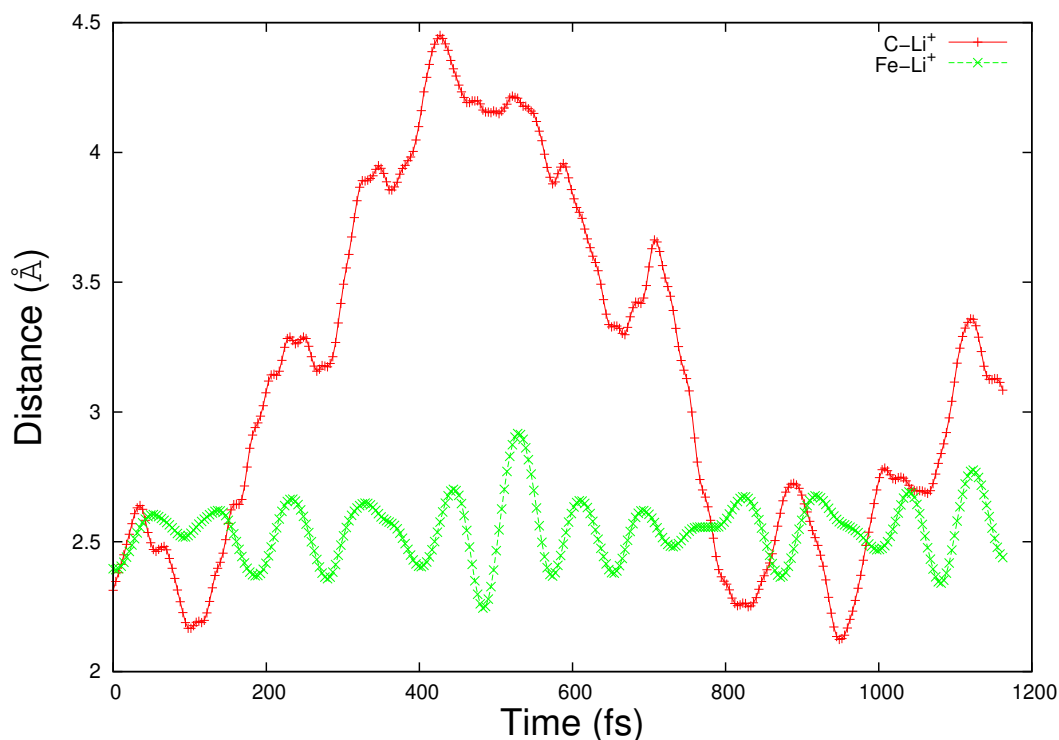


Figure 2.12: Plot of Fe-Li and C-Li distances as a function of time for a representative trajectory that showed planetary motion.

2.12 shows a plot of Fe-Li and C-Li bond distance as a function of time for a representative trajectory that showed planetary motion of  $\text{Li}^+$  about Fe atom. In this plot, the Fe- $\text{Li}^+$  bond distance oscillates about  $2.45 \text{ \AA}$  which is the equilibrium bond distance of Fe- $\text{Li}^+$  indicating that  $\text{Li}^+$  cation is bound to Fe atom during the trajectory. On the other hand, C- $\text{Li}^+$  distance goes as high as  $4.5 \text{ \AA}$  and then decreases because of planetary motion of  $\text{Li}^+$ . The remaining trajectories out of 25 showed relative Cp ring rotation with incomplete planetary motion of  $\text{Li}^+$  about Fe atom.

Five trajectories were also initiated and integrated for 1.5 ps from the transition state **TSe** using similar initial conditions as discussed above. These trajectories followed two kinds of pathways. In the first path, the  $\text{Li}^+$  cation goes above the Cp ring and forms the most stable

**CP** complex and stayed there for full integration time of 1.5 ps. In the second path, the  $\text{Li}^+$  cation goes near the Fe metal, forms **ML** complex and showed planetary motion through the transition state **TSf**.

### 2.3.2.2 Bimolecular dynamics of the lithiation

Having understood the dynamics and various pathways followed once ferrocene is lithiated, it is of fundamental interest to understand the initial binding site of  $\text{Li}^+$  on the ferrocene moiety. In order to do that, bimolecular collisions were carried out between  $\text{Li}^+$  cation and ferrocene moiety. The initial separation between ferrocene and  $\text{Li}^+$  was 8 Å and for effective collisions, an impact parameter of zero was used for all the trajectories. The vibrational and rotational energies were sampled using Boltzmann distribution at 300 K. 80 trajectories were initiated and integrated numerically using velocity-Verlet algorithm by using a time step of 0.3 fs. The trajectories were integrated for 0.5-1.5 ps. The initial orientation of  $\text{Li}^+$  cation with respect to ferrocene for 80 trajectories covers the full range of  $0^\circ$ - $90^\circ$  for the angle  $\angle X_1\text{-Fe-Li}^+$  as shown in Figure 2.13(a). In this figure, filled blue circles (●) are initial orientations of  $\text{Li}^+$  that exhibited in *exo* attack and filled red triangles (▶) are those that exhibited *endo* attack.

In 67 out of 80 trajectories,  $\text{Li}^+$  attacked the ferrocene moiety at the top of the Cp ring through *exo* attack. The rest 13 trajectories followed *endo* attack and forms **ML** isomer. Figure 2.13(b) shows three representative trajectories in which different pathways were followed. In this figure, black squares (□) and blue circles (○) show two trajectories exhibiting *exo* attack and red triangles (▶) showed a trajectory showing *endo* attack. Out of 67 *exo* trajectories, 56 of them were trapped in the **CP** minimum for the full integration time. In the rest 11 trajectories, after the formation of **CP** isomer, **ML** isomer was formed. Interestingly, in 2 out these 11 trajectories, after the formation of **ML** isomer, *planetary* motion of  $\text{Li}^+$  was observed about the Fe atom. Figure 2.14(a) shows superimposed frames of a representative trajectory in which after *exo* attack, **ML** isomer is formed which then isomerizes to other symmetrical **ML** isomers via the transition state **TSf** resembling a *planetary* kind of motion. In the 13 trajectories in

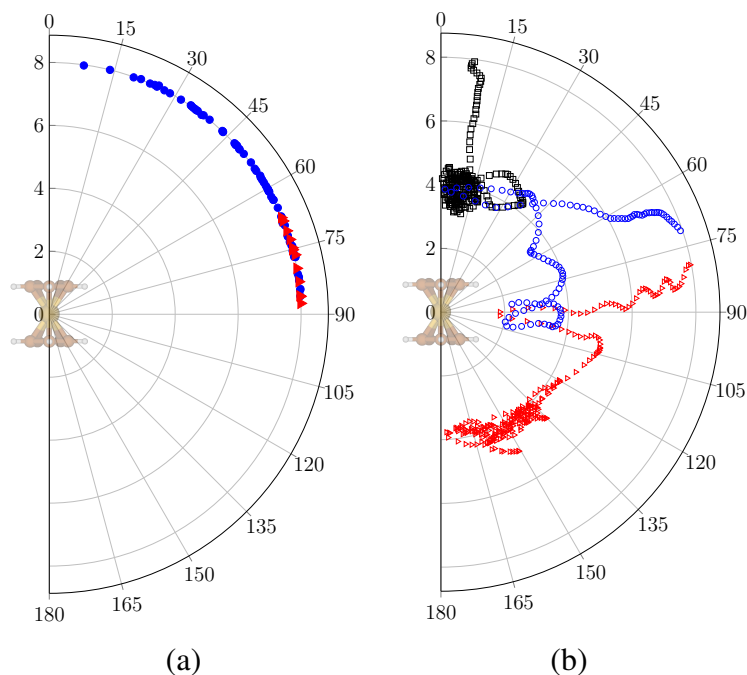


Figure 2.13: Plots of  $\angle X_1\text{-Fe-Li}^\circ$  vs Fe-Li distance in polar coordinates (Å). (a) Initial orientation of  $\text{Li}^+$  in 80 trajectories. (b) 3 representative trajectories showing different attacks.

which  $\text{Li}^+$  attacked in *endo* fashion, 3 trajectories were trapped in the **ML** minimum for the full integration time. In 1 out of 13 trajectories, after the formation of **ML**, the system exhibited *planetary* motion. In another 5 trajectories out of 13, after the formation of **ML** isomer via *endo* attack, the system isomerized to form the **CP** isomer and stayed in that minimum for complete integration time. In the remaining 2 *endo* trajectories, after the formation of **ML** isomer, interconverted to form the **CP** isomer and then back to the **ML** isomer and then showed *planetary* motion. Figure 2.14(b) shows a representative trajectory exhibiting this kind of pathway. It is important to note that  $\text{Li}^+$  was also found to be very mobile as that of  $\text{H}^+$  and showed rich dynamical features during dynamics.

As seen in protonation of ferrocene, it is interesting to see if there is any kind of effect on the pathway followed in the reaction due to the initial orientation of  $\text{Li}^+$  cation with respect to ferrocene. Figure 2.13(a) shows the plot of  $\angle X_1\text{-Fe-Li}^+$  vs Fe- $\text{Li}^+$  distance for the initial point of 80 trajectories. The initial orientation of  $\text{Li}^+$  ( $\angle X_1\text{-Fe-Li}^+$ ) is well distributed in the full

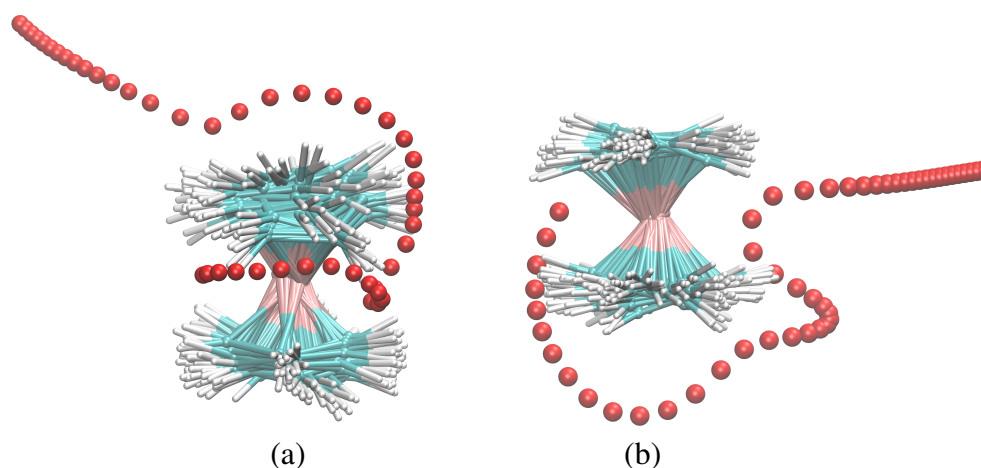


Figure 2.14: Superimposed frames for representative trajectories exhibiting (a) *exo* attack of  $\text{Li}^+$  followed by planetary motion and (b) *endo* attack of  $\text{Li}^+$  followed by the formation of **CP** and then **ML** via **TSd**. The incoming  $\text{Li}^+$  is shown in red color.

range of  $0^\circ$ - $90^\circ$  with respect to ferrocene. It was quite evident from the plot that trajectories that follow *endo* mechanism showed orientational preference ( $65^\circ < \angle \text{X}_1\text{-Fe-Li}^+ < 90^\circ$ ). However, the trajectories in which *exo* mechanism is followed did not show any such preference on the initial orientation of  $\text{Li}^+$  and  $\angle \text{X}_1\text{-Fe-Li}^+$  covers the full range of  $0^\circ$ - $90^\circ$ .

## 2.4 Summary and conclusions

To understand the atomic level mechanism of protonation and lithiation of ferrocene, *ab initio* classical trajectory simulations were performed at the B3LYP/DZVP level of theory. The simulations revealed that both the electrophiles  $\text{H}^+$  and  $\text{Li}^+$  are very mobile during the dynamics showing rich dynamical features. In both protonation and lithiation, the *exo* path was followed by a majority of the trajectories consistent with the model given by Cunningham and coworkers for hard electrophiles. An initial orientation of the incoming electrophile was observed for trajectories that follow *endo* pathway. However, for trajectories that follow *exo* pathway, no such preference was observed. Interestingly, during lithiation,  $\text{Li}^+$  cation exhibited *planetary* motion around Fe atom.



## COMPUTATIONAL STUDY OF BORYLATION OF 1-1'-BIS(TRIMETHYLSTANNYL)FERROCENE WITH $\text{BCl}_3$

### 3.1 Introduction

**E**lectrophilic aromatic substitution reactions are an important class of chemical reactions that are used extensively in the synthesis of substituted aromatic compounds. Ferrocene being aromatic undergoes electrophilic aromatic substitution reactions characteristic of aromatic compounds such as Friedel-Crafts reactions<sup>9,10,29</sup> and mercuration.<sup>11</sup> In these class of reactions, an incoming electrophile attacks the cyclopentadienyl ring by either *exo* or *endo* pathway as discussed in Chapter 1. It has been observed that hard electrophiles attack using *exo* pathway, while, soft electrophiles attack using *endo* pathway.<sup>9-11</sup> Using this approach, several derivatives of ferrocene have been synthesized that have found applications in various fields in chemistry.<sup>30-32</sup>

In a recent work,<sup>33</sup> borylation of ferrocene has been achieved by the electrophilic substitution of  $\text{BCl}_3$  to 1-1'-bis(trimethylstannyl)ferrocene (Figure 3.1). The reaction of **F1** with

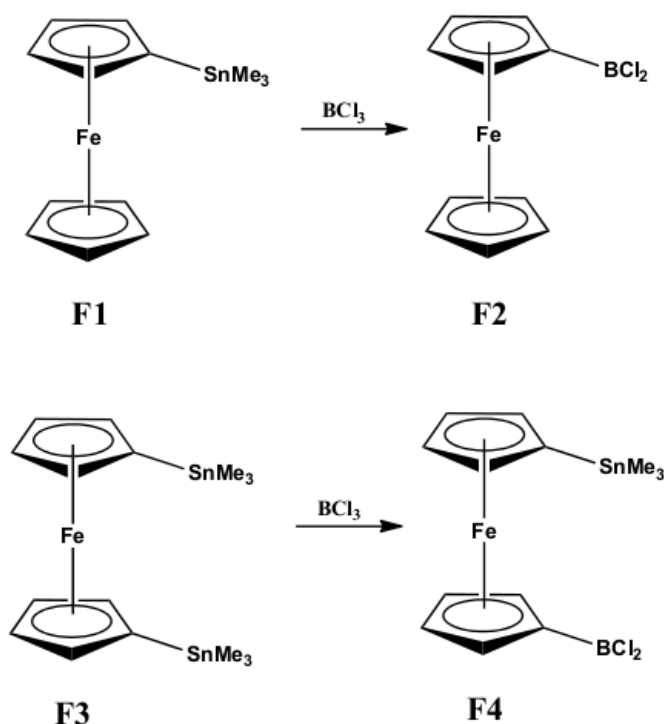


Figure 3.1: Reaction of trimethylstannyl ferrocene and 1-1'-bis(trimethylstannyl)ferrocene with  $\text{BCl}_3$  to give  $\text{BCl}_2$  substituted ferrocene derivatives.

$\text{BCl}_3$  gives **F2** where  $\text{BCl}_2$  replaces  $\text{SnMe}_3$  group. On the other hand, when **F3** is treated with 1 equivalent of  $\text{BCl}_3$ , it is expected that one of the  $\text{SnMe}_3$  group would be replaced by  $\text{BCl}_2$  to form **F4**. However, when this reaction was carried out by Frieder and coworkers<sup>33</sup> in hexane solvent at  $-78\text{ }^\circ\text{C}$ , they found three products: 1-stannyl-2-borylferrocene (**1-2**), 1-stannyl-3-borylferrocene (**1-3**), and 1-stannyl-1'-borylferrocene (**F4**). The spectroscopic yields from NMR experiments revealed that **1-2** is the major product with a yield of 87%, **1-3** - 10% and **F4** - 3%. This is quite unusual because as explained in Figure 3.1, **F4** is expected to be the major product as  $\text{Ar-Sn}$  ( $\text{Ar}=\text{Aryl}$ ) is more reactive towards boron halides as compared to  $\text{Ar-H}$  bonds. Moreover, the reaction resulted in the formation of selective ortho-substituted product with a yield of 87%. This means that  $\text{BCl}_3$  replaces H atom from the C atom of the Cp ring and this H atom can now hop to the adjacent C atoms on the same Cp ring or to the other Cp ring leading to the removal of  $\text{SnMe}_3\text{Cl}$  to form products.  $\text{BCl}_3$  being a hard electrophile is expected to follow *exo* pathway according to previous studies conducted by Cunningham and coworkers.<sup>9-11</sup>

Here, in this study, a detailed DFT study was undertaken to understand the atomic-level mechanism of the reaction of 1-1'-bis(trimethylstannyl)ferrocene (**F3**) with  $\text{BCl}_3$ .

## 3.2 Methodology

The mechanism of the reaction was investigated by computing free energy profile (FEP) for different pathways along the reaction at the experimental temperature (195.15 K). The DFT functional B3LYP<sup>34,35</sup> along with Dunning's DZVP basis set<sup>36</sup> for C, H, B and Cl and LANL2DZ for Fe and Sn was used to calculate the FEP. To incorporate solvent effects, polarizable continuum model (PCM) was used for hexane solvent. The nature of the stationary points were characterized by computing the harmonic vibrational frequencies. Intrinsic reaction coordinate (IRC) calculations were performed to connect the transition states to their adjacent minima. All the free energies reported here for different stationary points are with respect to the energy of the reactants. All the electronic structure calculations were performed using Gaussian 16 software package.<sup>37</sup>

## 3.3 Results

The reactant (**F3**) can exist in two isomers: **1-2'** and **1-3'** as shown in Figure 3.2. The **1-3'** isomer was found to be more stable than **1-2'** isomer with free energy difference of 1.06 kcal/mol.

Since 1-1'-bis(trimethylstannyl)ferrocene can exist in two isomers, **1-2'** and **1-3'**, attack of  $\text{BCl}_3$  on both the isomers will give rise to different pathways. To understand the mechanism of this reaction, free energy profiles for different pathways were mapped.

### 3.3.1 Pathway for 1-2 product

$\text{BCl}_3$  being a Lewis acid can behave as an electrophile and attack 1-1'-bis(trimethylstannyl)ferrocene either by *exo* or *endo* pathway to form products. Figure 3.3 shows the free energy profile of the *exo* attack of  $\text{BCl}_3$  on **1-2'** isomer of 1-1'-bis(trimethylstannyl)ferrocene leading to the formation of **1-2** product.  $\text{BCl}_3$  attacks **1-2'** isomer of 1-1'-bis(trimethylstannyl)ferrocene on the  $\alpha$ -C atom of Cp ring by forming an agostic intermediate **1** via the transition state **TS1**. The barrier for the formation of **1** is 21.0 kcal/mol. During this process, the B–C bond distance changes from 2.09 Å in **TS1** to 1.74 Å in intermediate **1**. In intermediate **1**, the H atom on the  $\alpha$ -C atom forms a three-centered bond with Fe–H bond distance being 2.29 Å. This H atom can hop to the other ring through transition state **TS2** to form an agostic intermediate **2** with the trimethylstannyl group projecting out of the ring. The barrier for this H-atom hopping is 5 kcal/mol with the Fe–H bond distance changing from 1.51 Å in **TS2** to 2.49 Å in **2**. Trimethylstannyl group can now abstract one Cl atom from  $\text{BCl}_3$  via **TS3** with a barrier of 15 kcal/mol to form the  $\alpha$ -substituted product and trimethylstannyl chloride. Free energy of products was found to be 22.8 kcal/mol below the reactants.

The *exo* attack of  $\text{BCl}_3$  on the  $\alpha$ -C atom of the **1-3'** isomer to give **1-2** product was also

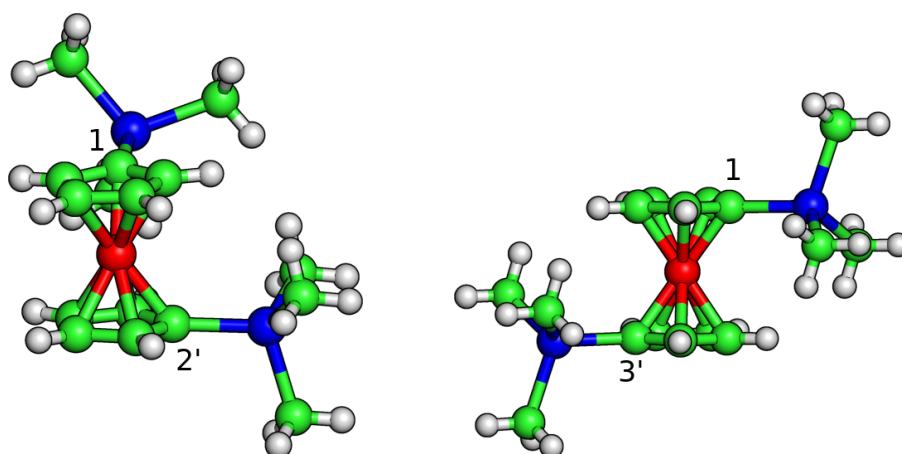


Figure 3.2: **1-2'** and **1-3'** isomers of 1-1'-bis(trimethylstannyl)ferrocene

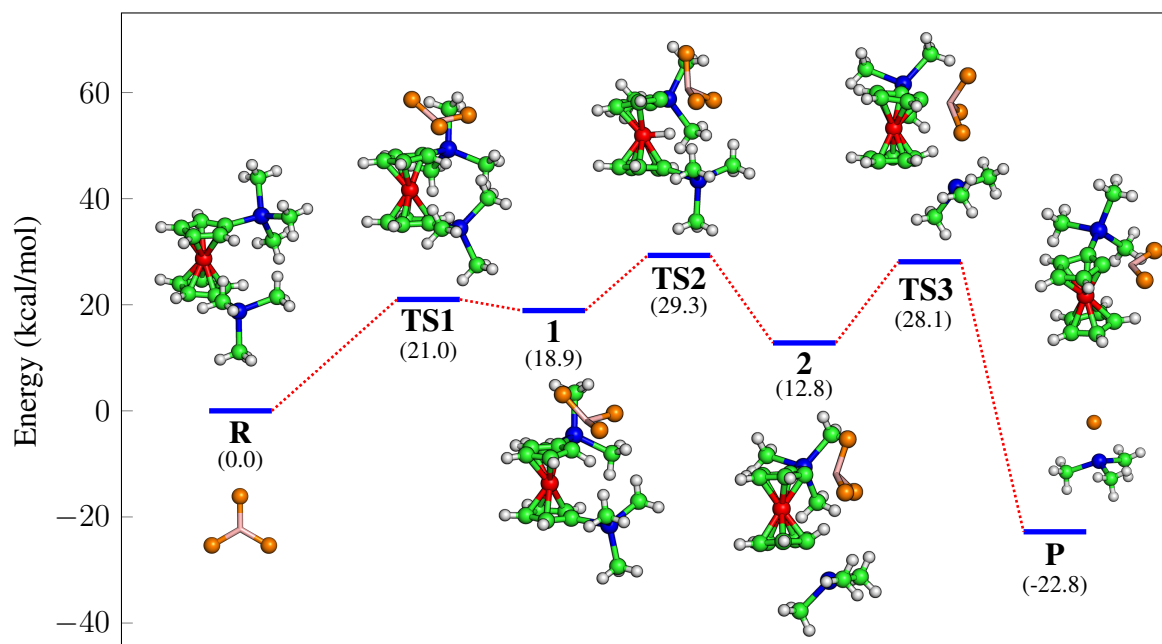


Figure 3.3: Free energy profile of *exo* attack of  $\text{BCl}_3$  to form  $\alpha$ -substituted **1-2** product

studied. Figure 3.4 shows the free energy profile of *exo* attack of  $\text{BCl}_3$  on **1-3'** isomer to give **1-2** product.  $\text{BCl}_3$  attacks **1-3'** isomer on the  $\alpha$ -C atom to form agostic intermediate **4** via the transition state **TS4** with a barrier of 12.9 kcal/mol. The B–C( $\alpha$ ) bond distance changes from 1.97 Å in **TS4** to 1.83 Å in the agostic intermediate **4**. The Fe–H bond distance in intermediate **4** is 2.44 Å. The intermediate **4** with free energy of 12.8 kcal/mol is converted to another agostic intermediate **5** on the other ring through the transition state **TS5** with a barrier of 10.5 kcal/mol in which an H atom hops to another ring. Here, the Fe–H bond distance changes from 2.44 Å in intermediate **4** to 1.51 Å in **TS5** to 1.8 Å in the intermediate **5**. The free energy of the intermediate **5** is 21.3 kcal/mol. The other H atom that is not involved in agostic interaction in intermediate **5** hops to the adjacent C atom bearing the leaving group  $\text{Me}_3\text{Sn}$  through a high barrier transition state **TS6** (19.2 kcal/mol) to form another agostic intermediate **6** having a free energy of 15.1 kcal/mol. As seen in other pathways, the  $\text{Me}_3\text{Sn}$  group now leaves by abstracting a Cl atom from  $\text{BCl}_3$  that is attached on the other Cp ring through the transition state **TS7** with a barrier of 1.4 kcal/mol to form products having free energy of -22.3 kcal/mol.

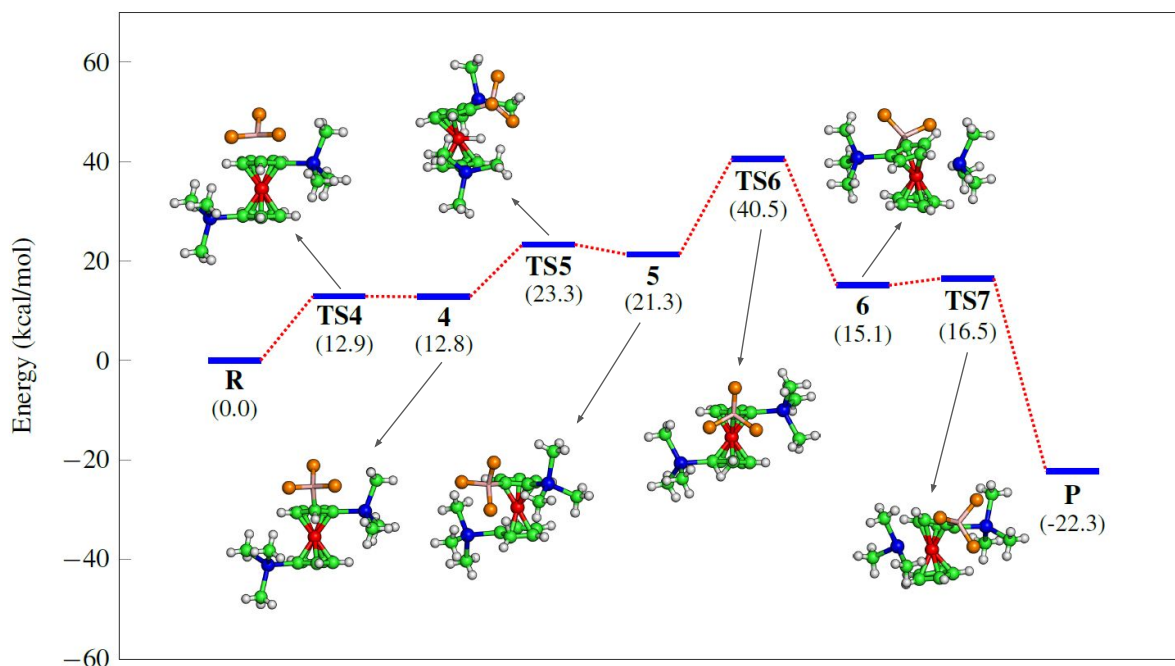


Figure 3.4: Free energy profile of *exo* attack of  $\text{BCl}_3$  on **1-3'** isomer

To understand if *endo* attack of  $\text{BCl}_3$  can give rise to **1-2** product, various *endo* pathways were investigated using both the isomers of 1-1'-bis(trimethylstannyl)ferrocene but none of those intermediates could be stabilized.

### 3.3.2 Reaction path for the formation of **1-3** product

To map the free energy profile for the formation of **1-3** product, we started with the *exo* attack of  $\text{BCl}_3$  on  $\beta$ -C atom of **1-3'** isomer. Figure 3.5 shows the free energy profile for the *exo* attack of  $\text{BCl}_3$  on **1-3'** isomer of 1-1'-bis(trimethylstannyl)ferrocene.  $\text{BCl}_3$  attacks  $\beta$ -C atom through the transition state **TS8** which is 19.4 kcal/mol above reactant to form the intermediate **7** having free energy of 18.7 kcal/mol. Intermediate **7** is an agostic structure with the Fe–H bond distance was 2.36 Å. The B–C( $\beta$ ) bond distance changes from 2.07 Å in **TS7** to 1.76 Å in **7**. The H atom that forms agostic interaction in the intermediate **7** then hops to another ring through the transition state **TS9** to form another agostic like structure **8**. The free energies of **TS9** and **8**

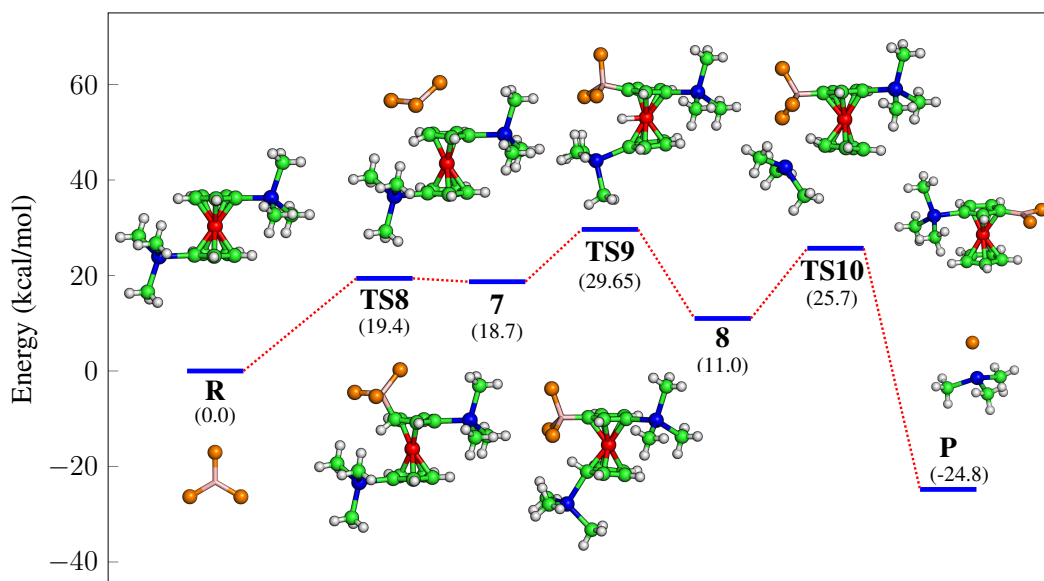


Figure 3.5: Free energy profile of *exo* attack of  $\text{BCl}_3$  to form **1-3** product

are 29.65 and 11.0 kcal/mol, respectively and the Fe–H bond distance in **TS9** is 1.51 Å which changes to 2.48 Å in the agostic intermediate **8**. The trimethylstannyl group in intermediate **8** is above the Cp ring and can abstract one Cl atom from  $\text{BCl}_3$  on the other ring through the transition state **TS10** (25.7 kcal/mol) to form **1-3** product. The Sn–C bond distance changes from 2.32 Å in intermediate **8** to 2.93 Å in transition state **TS10**. The products have a free energy of -24.8 kcal/mol.

### 3.3.3 Free energy profile for direct product (**F4**)

To understand the formation of the third product **F4**, various *exo* pathways were investigated in which  $\text{BCl}_3$  attacks different C atoms of the Cp ring of both **1-2'** and **1-3'** isomers of 1-1'-bis(trimethylstannyl)ferrocene. However, none of those intermediates could be stabilized. Then, the pathways in which  $\text{BCl}_3$  attacks in *endo* fashion were investigated. Figure 3.6 shows the partial free energy profile for the formation of the product **F4** via the *endo* pathway. The path begins with the  $\text{BCl}_3$  attack the carbon atom bearing the leaving group  $\text{Me}_3\text{Sn}$  by an *endo* face to form the intermediate **9** in which both  $\text{BCl}_3$  and the leaving group  $\text{Me}_3\text{Sn}$  are attached.

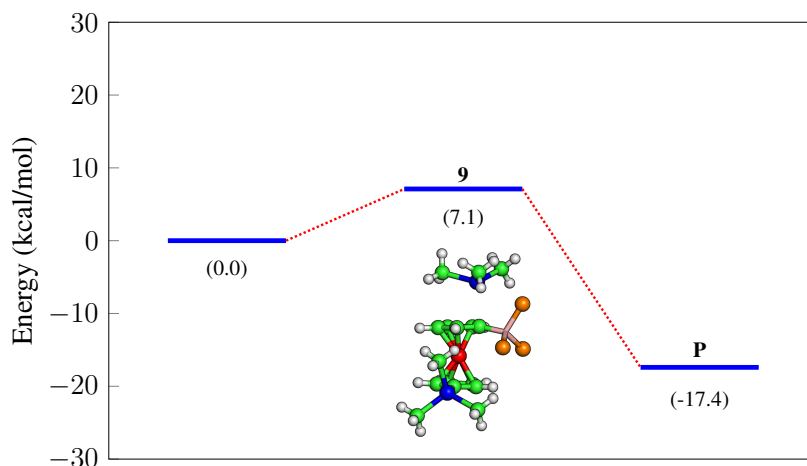


Figure 3.6: Free energy profile for the formation of **direct product (F2)**

Clearly, the intermediate **9** can only be formed through an *endo* pathway in which BCl<sub>3</sub> first precomplexes with Fe metal and then attacks the C atom bearing the leaving group Me<sub>3</sub>Sn. The free energy of the intermediate **9** is 7.1 kcal/mol. In the intermediate **9**, the Sn–C and B–C bond distances are 2.58 and 1.64 Å, respectively. Me<sub>3</sub>Sn then leaves by abstracting one Cl atom from BCl<sub>3</sub> but this transition state could not be identified. The free energy of the products (**F4** + Me<sub>3</sub>SnCl) is -17.4 kcal/mol.

### 3.4 Discussion and summary

To understand the mechanism of the borylation reaction between 1-1'-bis(trimethylstannyl)ferrocene and BCl<sub>3</sub>, FEP were mapped for various pathways leading to the formation of different products. Both *exo* and *endo* attacks of BCl<sub>3</sub> were employed in mapping the pathways. It was found that the *exo* attack of BCl<sub>3</sub> on **1-2'** isomer of **F3** leads to the formation of **1-2** product. In a similar way, the pathway for the formation of **1-3** product was also mapped in which **1-3'** isomer was used and the attack of BCl<sub>3</sub> followed *exo* pathway. Interestingly, **1-2** product was also obtained by the *exo* attack of BCl<sub>3</sub> on the α-C atom of **1-3'** isomer. This pathway included the hopping of H atom from one C atom to another which has high barrier making this pathway highly

unlikely to happen. Various pathways were also investigated in which *endo* attack of  $\text{BCl}_3$  was employed to form **1-2** and **1-3** products but none of them could be identified. So, **1-2** and **1-3** products can only be formed by the *exo* attack of  $\text{BCl}_3$ . In case of **direct** product, different pathways in which  $\text{BCl}_3$  attacks in *exo* fashion was employed but none of those intermediates could be identified. On the contrary, an intermediate **9** was identified on the FEP that can only be formed by the *endo* attack of  $\text{BCl}_3$ . This indicates that **direct** product can only be obtained by the *endo* attack of  $\text{BCl}_3$ .

To summarize, **1-2** and **1-3** products can only be formed through an *exo* attack of  $\text{BCl}_3$  in which one H atom is displaced by  $\text{BCl}_3$  to the another Cp ring leading to the formation of products and **direct** product (**F4**) can only be formed through an *endo* attack of  $\text{BCl}_3$ .



## MECHANISMS AND DYNAMICS OF NUCLEOPHILIC AROMATIC SUBSTITUTION ( $S_NAr$ ) REACTION

### 4.1 Introduction

Substitution reactions are a broad class of chemical reactions with numerous applications in the field of synthetic organic chemistry and molecular biology.<sup>7,38</sup> Nucleophilic aromatic substitution reactions<sup>39</sup> ( $S_NAr$ ) are a subset of substitution reactions in which aromatic ring is involved and the substitution happens at one of the carbon atoms of the aromatic ring by a nucleophile. For an  $S_NAr$  reaction to happen, the aromatic ring needs to be activated by electron-withdrawing group/groups attached to the ring. It has been proposed that this reaction goes through a concerted or an addition-elimination pathway.<sup>7</sup> In the first step, the incoming nucleophile attacks the ipso carbon of the aromatic ring where the leaving group is attached and forms Meisenheimer complex (or,  $\sigma$  complex). In the second step, the leaving group departs to form the products. The nature of the Meisenheimer complex (minimum or maximum) on the potential energy surface (PES) and thus the mechanisms, are

dictated by the number of electron-withdrawing groups attached to the aromatic ring which stabilize the complex and were sometimes isolated experimentally.<sup>40</sup> A transition state (TS) nature of the  $\sigma$ -complex results in a concerted mechanism while the minimum energy point results in the step-wise addition-elimination mechanism.

Various theoretical<sup>41-48</sup> and experimental studies<sup>49-57</sup> have been carried out to understand the mechanism of  $S_NAr$  reactions in different systems in the past few decades. Harris and coworkers performed semi-empirical calculations using the Modified Neglect of Diatomic Overlap (MNDO) method for the reactions between substituted benzene rings and halogens and found that the reactions go through addition-elimination mechanism.<sup>41</sup> In another semi-empirical study using MNDO and AM1 methods, Vladimir and coworkers<sup>42</sup> found out that proton transfer might play an important role in the mechanism with reaction going through the stable  $\sigma$ -complex. Laiter and coworkers employed MP2 method with 6-31+g\* basis set to map the PES of monosubstituted halobenzenes and disubstituted nitrohalobenzene with halogens as nucleophile and studied the effect of electron-withdrawing groups on the  $\sigma$ -complex.<sup>43</sup> They observed that in the case of monosubstituted halobenzenes, the reaction followed a single-step mechanism without the  $\sigma$ -complex formation, while, in case of disubstituted nitrohalobenzene, the reaction followed a multi-step pathway with the formation of  $\sigma$ -complex. They also showed that for the identity reaction  $C_6H_5X + X^- \longrightarrow C_6H_5X + X^-$  ( $X = \text{halide}$ ), only  $F^-$  formed the stable  $\sigma$ -complex, and for the other halides,  $\sigma$ -complex was a transition state on the PES. These results clearly showed that electronic effects govern the stability of  $\sigma$ -complex and electron-withdrawing nitro groups help in stabilizing  $\sigma$ -complex. In the DFT study using B3LYP/6-31+g\*\* level of theory<sup>44</sup>, Svensson and coworkers computed the relative stabilities of the  $\sigma$ -complex in various aromatic systems with anionic and neutral nucleophiles and found out that the  $\sigma$ -complex was stable (step-wise pathway) when  $F^-/HF$  was the leaving group. For  $Cl^-/HCl$  and  $Br^-/HBr$  as leaving groups, the stable  $\sigma$ -complex could not be found on the PES and they concluded that these reactions go through concerted substitution step. To

understand how electronic factors affect the  $S_NAr$  reactions, Uggerud and coworkers<sup>45</sup> employed OPBE DFT functional with 6-311++g\*\* basis set to map the PES of reactions between various substituted benzene with various nucleophiles. They found that intrinsic nucleophilicity (energy required to form  $\sigma$ -complex) is an important criteria. Stable  $\sigma$ -complexes had more intrinsic nucleophilicity and decreased the aromatic character of the  $\sigma$ -complex. Cramer and coworkers<sup>46</sup> used M06-2X/6-311+g(3df,2p) level of theory to understand the dehalogenation of aromatics by the attack of hydride anion on various halogen substituted benzene rings. They concluded that for fluorinated benzene, concerted substituted pathway was followed, however in the case of chlorinated and brominated benzene systems,  $H^-$  attacked the carbon atom ortho to C–X bond via the formation of an anionic intermediate followed by elimination of HX to form the dehalogenated product.

Several experimental studies<sup>49–57</sup> were also conducted to understand the mechanism and importance of  $\sigma$ -complex in  $S_NAr$  reactions. Gerbaux and coworkers<sup>49</sup> did mass spectrometry experiments on ionized benzene derivatives with methyl isocyanide as nucleophile and found that N-methylbenzotrilium ions are formed in large amount as a result of  $S_NAr$  reaction. They also did theoretical studies at the B3LYP/6-31+g\*\* level of theory and found that reaction is exothermic and goes through ipso attack of nucleophile to form N-methylbenzotrilium ion as products. Ellervik and coworkers<sup>50</sup> undertook a kinetic study on the acid-catalyzed  $S_NAr$  reaction between phenolic hydroxyl group and sulfur containing nucleophiles and computed thermodynamic parameters for the reactions. They demonstrated that the mechanism of the reaction was different in non-polar solvents (multi-step) as compared to that in polar solvents. They further computed thermodynamic parameters using DFT methods and the numbers were comparable with the experiments. In another mass spectrometry experiment by Cooks and coworkers<sup>51</sup>, it was shown that the Meisenheimer complex was formed between 2,4,6-trinitrotoluene and  $CH_2NO_2^-$ . The mechanism of reaction between radical cations of mono and dihalogenated benzenes with  $NH_3$  was studied by Hans-Friedrich and coworkers<sup>52</sup> using

fourier-transform ion cyclotron resonance mass spectrometry (FT-ICR) and semi empirical (MNDO) calculations. They found that the mechanism was a slow two-step process involving addition and elimination via two complexes. The first one was a long lived  $\pi$ -complex in which  $\text{NH}_3$  sits on top of the radical cation benzene ring and the second complex is the  $\sigma$ -complex after which elimination happened. Rodrigo and coworkers<sup>53</sup> studied  $\text{S}_{\text{N}}\text{Ar}$  reaction between 1-fluoro-2,4-dinitrobenzene with series of amines experimentally and computationally and found that these reactions proceed through  $\sigma$ -complex and that formation of  $\sigma$ -complex was the rate determining step in the reaction. Their MP2 calculations showed the presence of strong interaction between ortho nitro group and acidic H atom of the amine. To understand the mechanism of the reaction between acetyl anion ( $\text{CH}_3\text{COCH}_2^-$ ) and electron-deficient nitroaromatics, Cooks and coworkers<sup>55</sup> used mass spectrometry and found that stable Meisenheimer complex formation takes place which results in distinctive and unique fragmentation pattern. In order to understand the effect of solvent polarity on  $\text{S}_{\text{N}}\text{Ar}$  reactions, Maia and coworkers<sup>56</sup> studied the aromatic nucleophilic substitution reaction between 4-chloronitrobenzene and N-anions from aryl and heteroarylamines and found that the reaction was two orders of magnitude faster in DMSO than in toluene. They argued that in DMSO, the ions were free, while, in toluene, the ions existed as ion pairs to explain the low reactivity in toluene.

While there have been several studies supporting the step-wise mechanism, the  $\text{S}_{\text{N}}\text{Ar}$  reaction can also be thought to follow a direct concerted mechanism similar to  $\text{S}_{\text{N}}2$  reaction. Riveros and coworkers<sup>57</sup> tried to address this question by doing mass experiments and DFT calculations (B3LYP/6-311++g\*\*) for the  $\text{S}_{\text{N}}\text{Ar}$  reaction  $\text{C}_6\text{H}_5\text{NO}_2 + \text{F}^- \longrightarrow \text{C}_6\text{H}_5\text{F} + \text{NO}_2^-$ . They found out that this reaction was quite unusual with large rate constant giving rise to only one product. Generally, direct attack is unfavorable for mono-substituted benzene ring as it needs high amount of energy making this reaction infeasible but it was seen that this reaction was very fast. They mapped only important stationary points on the PES and found out that the  $\sigma$ -complex is a transition state on the PES.

Here, in this study, the various reaction pathways for the aromatic nucleophilic substitution reaction of nitrobenzene with  $F^-$  was investigated using density functional theory (DFT), Møller-Plesset perturbation theory and coupled-cluster wavefunction methods. The dynamical pathways followed in the reaction were studied by classical trajectory simulations.

## 4.2 Methodology

The potential energy profile was mapped for the  $S_NAr$  reaction  $C_6H_5NO_2 + F^- \longrightarrow C_6H_5F + NO_2^-$  using different levels of theory. MP2<sup>58</sup> and DFT methods were employed with 6-31+G\*, 6-311++G\*\*<sup>59,60</sup>, aug-cc-pVDZ<sup>61,62</sup> and aug-cc-pVTZ<sup>61,62</sup> basis sets. In addition, different DFT functionals such as B3LYP<sup>34,35</sup>, M06-2X<sup>63</sup>, BHandh<sup>64</sup>, OPBE<sup>65-67</sup>, OLYP<sup>34,65,66</sup>, B97-1<sup>68</sup> and HCTH407<sup>69</sup> were also used for the study. The nature of the stationary points was established by computing harmonic vibrational frequencies. Intrinsic reaction coordinate (IRC) calculations were performed to connect the transition states to their adjacent minima. To obtain more reliable energies, single-point energies were computed using DLPNO-CCSD(T) method<sup>70,71</sup> with correlation consistent aug-cc-pVXZ ( $X = D, T, Q$ ) basis sets using the B3LYP/aug-cc-pvdz geometries using ORCA software package<sup>72</sup>. To obtain accurate energies, single point energies were computed for B3LYP/aug-cc-pVDZ optimized geometries of all the stationary points obtained on the PES using DLPNO/CCSD(T) method with aug-cc-pVDZ, aug-cc-pVTZ and aug-cc-pVQZ basis functions. The obtained energies were extrapolated to get CBS energies using the following three-point form equation<sup>73</sup>,

$$E(X) = E_{CBS} + Be^{\alpha X} \quad (4.1)$$

In equation 4.1,  $X = 2, 3, 4$  and  $E(X)$  corresponds to DLPNO-CCSD(T) energies computed using aug-cc-pVDZ, aug-cc-pVTZ and aug-cc-pVQZ basis functions, respectively. The DFT and MP2 calculations were performed using Gaussian 09 software package<sup>24</sup>. The energies reported for the different stationary points are with respect to the energy of the reactants.

## 4.3 Results and Discussions

### 4.3.1 Energetics

The potential energy profile for the reaction between  $C_6H_5NO_2$  and  $F^-$  was mapped using various DFT and MP2 methods. Table 4.1 shows relative energies of various stationary points computed at different levels of theory. In order to compare energies obtained at various levels of theory with DLPNO/CCSD(T)/CBS energies, mean absolute deviations (MUD) were computed for different levels of theory with respect to DLPNO/CCSD(T)/CBS energies. It was found that MUD for B3LYP/6-31+G\*, B3LYP/aug-cc-pVDZ and B3LYP/aug-cc-pVTZ methods were less than 1.5 kcal/mol. Except for B3LYP/6-311++G\*\* and M06-2X/6-31+G\* levels of theory, all other methods were able to identify all the stationary points on the PES. In both B3LYP/6-311++G\*\* and M06-2X/6-31+G\* levels of theory, optimized structure of **idm** had a linear  $C(sp^2)-H \cdots F$  geometry and the transition state **ts2** could not be found on the PES using these methods. Considering the computational cost for trajectory simulations and accuracy of various methods as compared to DLPNO/CCSD(T)/CBS level, B3LYP/6-31+G\* was chosen for further calculations.

Figure 4.1 shows the potential energy profile at B3LYP/6-31+G\* level of theory.  $F^-$  can form two kinds of complexes with nitrobenzene. If nitrobenzene and  $F^-$  approach each other in such a way that  $F^-$  is coplanar to the phenyl ring, then various ion-dipole (**id**) complexes can be formed with  $F^- \cdots H$  hydrogen bonds. Nitrobenzene with five hydrogen atoms can therefore form five hydrogen-bonded **id** complexes with  $F^-$ : two *ortho*-complexes (**ido** and **ido'**), two *meta*-complexes (**idm** and **idm'**) and one *para*-complex (**idp**). These **id** complexes can interconvert through different transition states. **idp** can convert to **idm** through the transition state **ts1** with a barrier of 2.81 kcal/mol. **idm** is also connected to **ido** through the transition state **ts2** having a barrier of 4.05 kcal/mol.

Approach of  $F^-$  from above or below the plane of the phenyl ring can result in the formation

Table 4.1: Electronic energies (kcal/mol) of stationary points relative to the reactants obtained at different levels of theory<sup>a</sup>

Method	idp	ts0	psc	ts1	idm	ts2	ido	ts3	osc	ts4	ipc	mts	P	MUD <sup>b</sup>
<b>B3LYP/6-31+G*</b>	-26.10	-19.70	-23.54	-23.29	-24.54	-20.49	-20.51	-16.24	-20.58	-12.87	-14.34	-9.11	-25.87	1.4
<b>B3LYP/6-311++G**</b>	-27.10	-20.78	-23.62	-24.48	-25.64	- <sup>c</sup>	19.93 <sup>d</sup>	-17.52	-20.80	-14.44	-15.82	-10.68	-26.21	
<b>B3LYP/aug-cc-pVDZ</b>	-25.92	-19.59	-23.02	-22.81	-24.43	-20.12	-20.42	-16.08	-20.21	-12.76	-14.11	-9.34	-23.92	1.3
<b>B3LYP/aug-cc-pVTZ</b>	-25.10	-19.04	-22.38	-22.30	-23.65	-19.61	-19.69	-15.65	-19.54	-12.65	-13.97	-9.25	-25.98	1.2
<b>M06-2X/6-31+G*</b>	-26.46	-18.55	-29.80	-25.18	-25.30	- <sup>c</sup>	19.96 <sup>d</sup>	-16.33	-27.53	-15.52	-16.86	-15.96	-29.18	
<b>M06-2X/6-311++G**</b>	-27.78	-19.90	-30.09	-26.42	-26.65	-23.62	-23.64	-17.82	-27.92	-17.18	-18.39	-17.65	-29.80	5.0
<b>MP2/aug-cc-pVDZ</b>	-23.22	-10.28	-16.09	-21.72	-21.23	-18.60	-17.09	-8.45	-12.99	-9.92	-5.90	-1.56	-32.51	4.4
<b>BHandH/aug-cc-pVDZ</b>	-31.73	-22.85	-35.81	-29.32	-30.24	-26.70	-26.95	-20.17	-33.32	-18.65	-20.80	-19.20	-23.40	7.7
<b>BHandH/aug-cc-pVTZ</b>	-30.96	-22.42	-36.15	-28.68	-29.51	-26.11	-26.29	-19.89	-33.60	-18.57	-20.78	-20.55	-26.06	7.5
<b>OPBE/aug-cc-pVDZ</b>	-24.41	-18.76	-24.15	-19.82	-22.79	-17.23	-19.08	-14.60	-21.45	-9.63	-12.00	-10.99	-21.51	2.4
<b>HCTH407/aug-cc-pVDZ</b>	-25.34	-20.52	-21.82	-22.04	-23.58	-19.43	-19.78	-16.68	-18.93	-12.59	-13.76	-8.99	-21.20	1.6
<b>OLYP/aug-cc-pVDZ</b>	-23.85	-18.81	-20.65	-20.25	-22.07	-17.54	-18.03	-14.79	-17.65	-10.12	-11.39	-7.77	-22.98	2.0
<b>B97-1/aug-cc-pVDZ</b>	-27.20	-20.62	-25.91	-23.97	-25.72	-21.34	-21.85	-17.18	-23.26	-13.84	-15.37	-12.45	-23.87	2.5
<b>DLPNO-CCSD(T)/CBS</b>	-24.27	-15.80	-19.88	-22.80	-23.76	-20.67	-20.49	-13.80	-18.00	-13.54	-14.17	-10.10	-24.84	
<b>Experiment<sup>e</sup></b>														-28.7

<sup>a</sup>Energies do not include zero-point energy.<sup>b</sup>Mean unsigned deviation(MUD) with respect to the DLPNO-CCSD(T)/CBS level of theory.<sup>c</sup>Optimized geometry is a minimum where C(sp<sup>2</sup>)-H-F is linear.<sup>d</sup>Geometry optimization results in **idm** stationary point.<sup>e</sup>Enthalpy of the reaction at 298 K<sup>?</sup>.

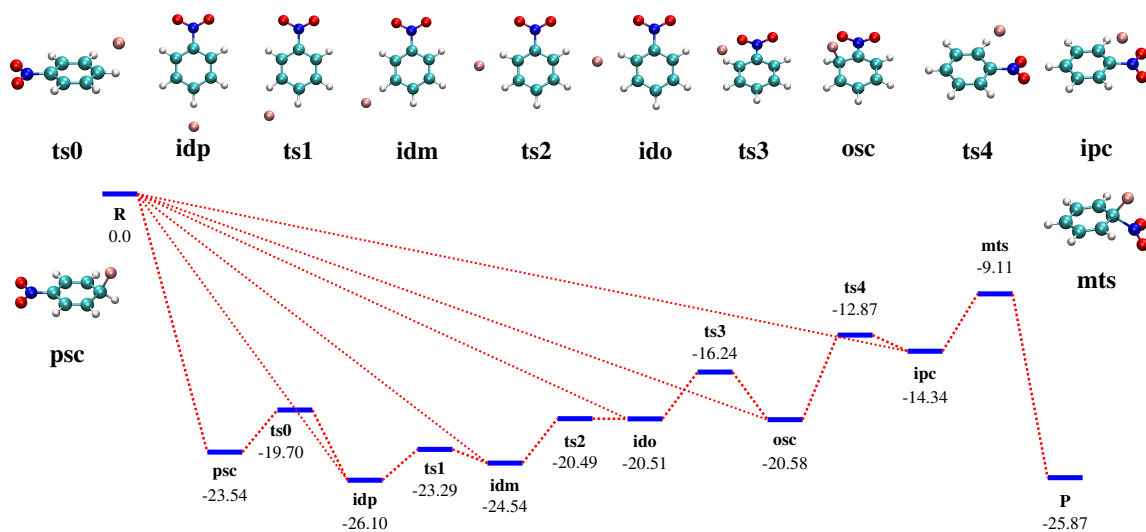


Figure 4.1: Potential energy profile for the reaction  $\text{C}_6\text{H}_5\text{NO}_2 + \text{F}^- \longrightarrow \text{C}_6\text{H}_5\text{F} + \text{NO}_2^-$  at B3LYP/6-31+G\* level of theory

of various sigma ( $\sigma_{\text{H}}$ )-complexes: **osc** and **osc'** at ortho carbon atom and **psc** at para carbon atom. These  $\sigma_{\text{H}}$ -complexes can also convert to **id** complexes through different transition states. **psc** is connected to **idp** through the transition state **ts0** with a barrier of 3.84 kcal/mol. **osc** is connected to **ido** via transition state **ts3** having a barrier of 4.34 kcal/mol.  $\text{F}^-$  can also approach the aromatic carbon atom bearing the leaving group (*ipso* carbon) from above or below the phenyl ring to form *ipso* complex (**ipc**) in which  $\text{F}^-$  sits above the *ipso* C atom. **ipc** is connected to products (**P**) through Meisenheimer transition state (**mts**) in which *ipso* carbon is  $sp^3$  hybridized. The barrier for this step was 5.23 kcal/mol and energy of the products (**P**) was found to be below reactants (**R**) by 25.87 kcal/mol. Interestingly, for this reaction, the Meisenheimer structure was found to be the transition state. It is to be noted that the various **id** and  $\sigma_{\text{H}}$ -complexes can also be formed directly from the reactants (**R**) depending on how  $\text{F}^-$  approaches nitrobenzene moiety. Figure 4.2 shows the optimized structures with their important geometrical parameters of different stationary points obtained on the PES.

It is important to point out that the energy of reactants (**R**) is higher in energy of all the

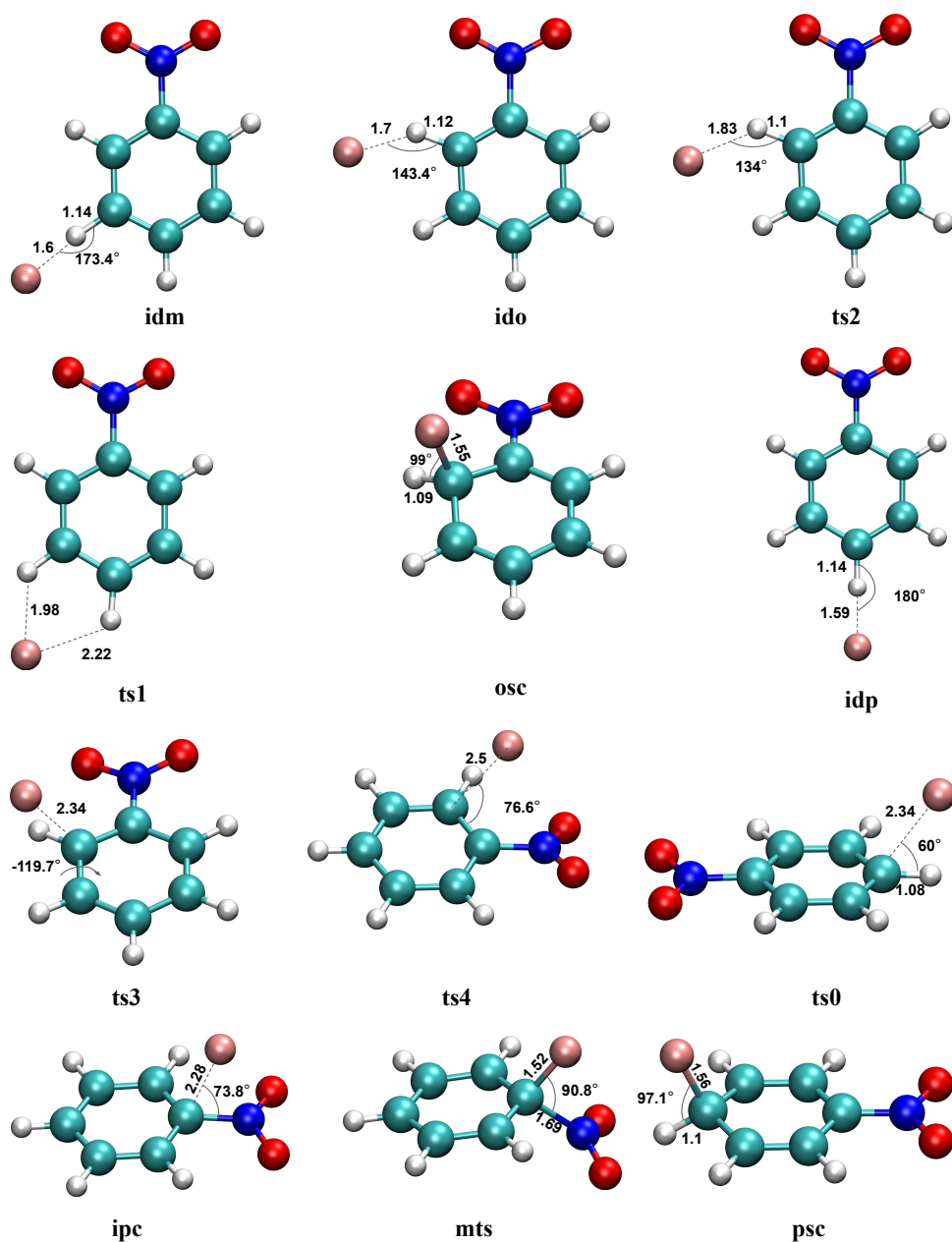


Figure 4.2: Optimized structures of different stationary points and their important geometrical parameters obtained at the B3LYP/6-31+G\* level of theory

stationary points. This indicates that there are many thermally accessible pathways as shown in Figure 4.1 in which **R** is connected to different complexes that can be formed directly from **R** as discussed above. To understand the atomic-level mechanism and different dynamical

pathways that takes place during the reaction, *ab initio* chemical dynamics simulations were performed at B3LYP/6-31+G\* level of theory.

### 4.3.2 *Ab initio* Chemical Dynamics

In order to understand different dynamical pathways followed in the S<sub>N</sub>Ar reaction between nitrobenzene and F<sup>-</sup>, *ab initio* classical dynamics simulations<sup>5,25,74</sup> were performed at B3LYP/6-31+G\*<sup>34,35,59,60</sup> level of theory using VENUS/NWChem software.<sup>25,74</sup> Since B3LYP/6-31+G\* level of theory gave energies close to DLPNO/CCSD(T)/CBS level, B3LYP/6-31+G\* level of theory was used for the dynamics.

#### 4.3.2.1 Bimolecular trajectory simulations

Bimolecular collision trajectories were computed between C<sub>6</sub>H<sub>5</sub>NO<sub>2</sub> and F<sup>-</sup> to understand the mechanism of the reaction C<sub>6</sub>H<sub>5</sub>NO<sub>2</sub> + F<sup>-</sup> → C<sub>6</sub>H<sub>5</sub>F + NO<sub>2</sub><sup>-</sup>. The initial separation between the two reactants was taken to be 10 Å. The rotational and vibrational energies of C<sub>6</sub>H<sub>5</sub>NO<sub>2</sub> was sampled using Boltzmann distribution<sup>5</sup> at 335 K which is the temperature at which Riveros and coworkers conducted gas phase experiments for this reaction.<sup>57</sup> For effective collisions, impact parameter *b* was equal to zero for the trajectories. A time step of 0.4 fs was used to numerically integrate the trajectories for 4 ps using velocity-Verlet algorithm. Relative translational energy of 0.99 kcal/mol, computed at 335 K, was given to reactants. The initial orientation of F<sup>-</sup> with respect to C<sub>6</sub>H<sub>5</sub>NO<sub>2</sub> was randomly chosen in all the trajectories.

In order to understand different pathways followed in the reaction, a new rotated coordinate system was used as shown in Figure 4.3. In this coordinate system, the whole molecule is rotated in such a way that the *para* carbon atom (C1) is placed at origin, *ipso* carbon atom (C2) is placed on the y axis and C1, C2 and C3 lie on *xy* plane. It is worth pointing out that the mechanism followed in the trajectories can be easily understood just by following the coordinates of F atom in this new rotated coordinate system.

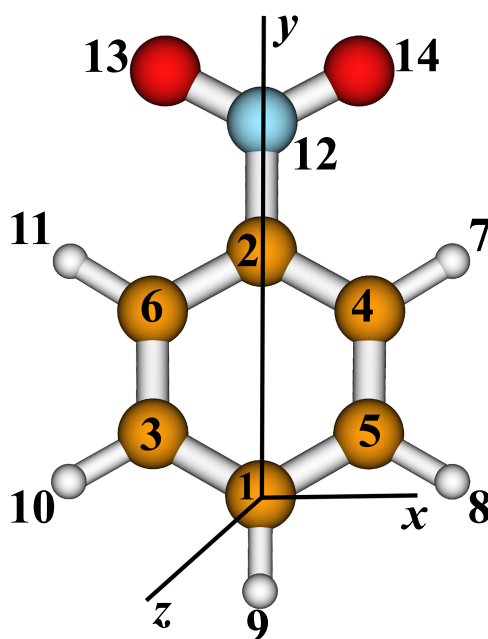


Figure 4.3: Rotated coordinate system with C1 as the origin.

395 trajectories were initiated out of which 3 were found to be reactive trajectories that resulted in the formation of fluorobenzene ( $C_6H_5F$ ) and nitrite anion ( $NO_2^-$ ). Out of rest 392 trajectories, 203 trajectories were trapped in different intermediates in which system isomerised between different **id** and  $\sigma$ -complexes till 4 ps of integration time and remaining 189 trajectories were non-reactive. Bimolecular collision between  $C_6H_5NO_2$  and  $F^-$  followed interesting dynamical pathways even though the reaction probability was found to be quite less. Interestingly, it was observed that the motion of F atom resembled a *roaming* type pathway during the reaction. Figure 4.4 shows three trajectories that resulted in the formation of products ( $C_6H_5F$  and  $NO_2^-$ ). It was observed that in these three reactive trajectories, various **id** and  $\sigma$ -complexes were formed before the formation of **mts** to form products clearly resembling a step wise mechanism even though the Meisenheimer structure is transition state (**mts**) on the PES of this reaction. Figure 4.5 shows snapshot of a representative bimolecular reactive trajectory. This is in contrast with the concerted mechanism proposed for this reaction by

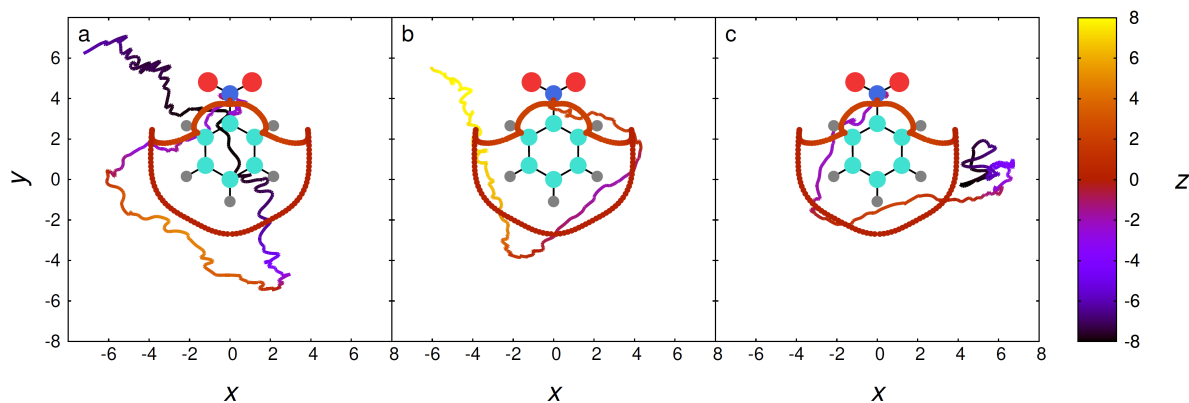


Figure 4.4: Coordinates ( $\text{\AA}$ ) of F atom during the reaction for three bimolecular reactive trajectories in the rotated coordinate system. The *IRC* path is also shown for comparison.

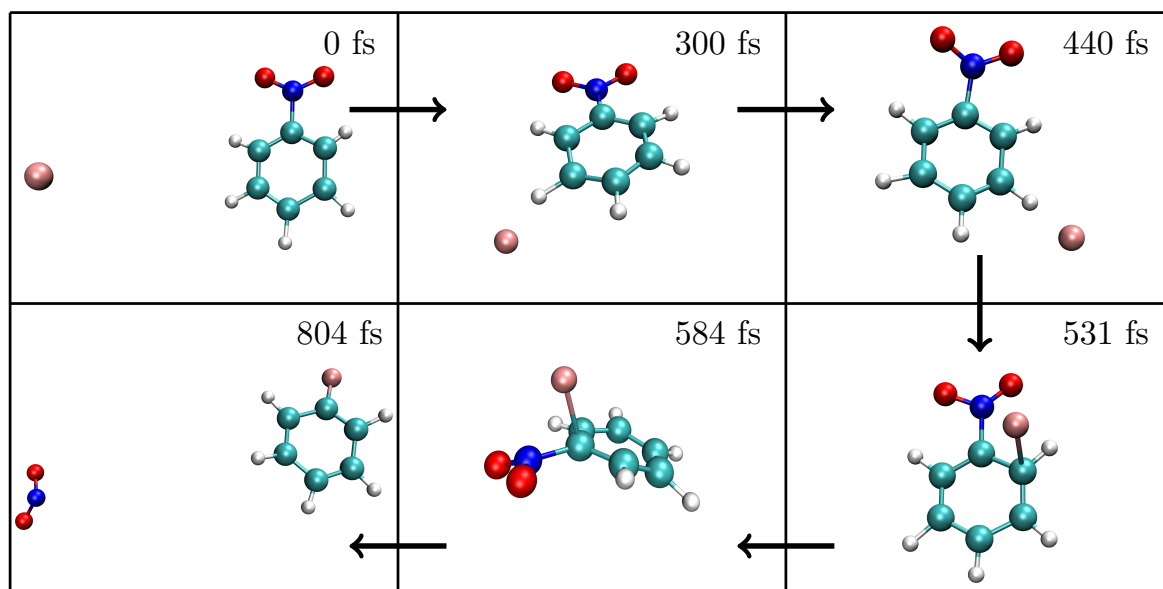


Figure 4.5: Snapshots of a representative bimolecular reactive trajectory

Riveros and coworkers<sup>57</sup> in which  $\text{F}^-$  is expected to attack on the *ipso* carbon bearing the leaving group.

#### 4.3.2.2 Post-Transition State Dynamics

Reaction probability in bimolecular trajectory simulations was very less. So, in order to improve the statistics of reactive trajectories and to understand the atomic-level mechanism

followed in the reaction in a better way, trajectories were initiated from the transition state **mts** using microcanonical normal mode sampling<sup>5</sup> at 335 K. The total energy available at the **mts** transition state ( $E_{\text{mts}}$ ) was calculated by computing the thermal energies of reactants ( $E_{\text{R}}$ ) at 335 K and the difference in potential energy between the reactants and the transition state **mts** ( $\Delta E = 9.1$  kcal/mol) given by,

$$\begin{aligned} E_{\text{mts}} &= \Delta E + E_{\text{R}} \\ &= \Delta E + E_{\text{R,vib}} + E_{\text{R,rot}} + E_{\text{R,trans}} \\ &= 9.1 + 68.04 + 0.99 + 0.99 \\ &= 79.12 \text{ kcal/mol} \end{aligned}$$

where,  $E_{\text{R,vib}}$  is the average vibrational energy for the reactants,  $E_{\text{R,rot}}$  is the average rotational energy for the reactants and  $E_{\text{R,trans}}$  is the relative translation energy for the reactants at 335 K.  $E_{\text{mts}} = 79.12$  kcal/mol was then partitioned as follows,

$$\begin{aligned} E_{\text{mts}} &= E_{\text{mts,vib}} + E_{\text{mts,rot}} + E_{\text{RC}} \\ \Rightarrow E_{\text{mts,vib}} &= E_{\text{mts}} - E_{\text{mts,rot}} - RT \\ \Rightarrow E_{\text{mts,vib}} &= 79.12 - 0.99 - 0.66 \\ \Rightarrow E_{\text{mts,vib}} &= 77.47 \text{ kcal/mol} \end{aligned}$$

where,  $E_{\text{mts,vib}}$  is the vibrational energy,  $E_{\text{mts,rot}}$  is the rotational energy and  $E_{\text{RC}} = RT$  is the reaction coordinate energy at the **mts**. Using the above energy partitioning for the **mts** transition state, 414 trajectories were initiated from the transition state **mts** using microcanonical normal mode sampling. A vibrational energy of 77.47 kcal/mol, rotational energy of 0.99 kcal/mol and energy in the reaction coordinate of 0.66 kcal/mol was provided for all the trajectories. For a given set of initial conditions, the trajectories were integrated for 1 ps each in both the forward and reverse directions. The forward and reverse directions were defined with respect to the momenta sign. If  $p_i^f$  is the momentum for the  $i^{\text{th}}$  component for a trajectory integrated in forward direction then, momentum in the reverse direction would be  $p_i^r = -p_i^f$ . It is to be

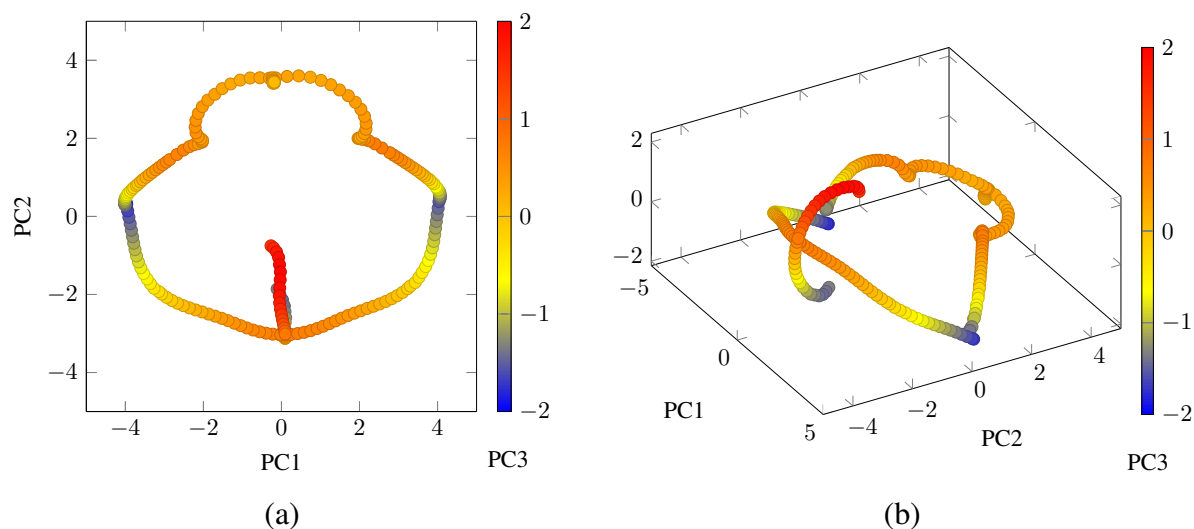


Figure 4.6: Three largest principal components (PC1, PC2 and PC3) representing *IRC* in R3D space

noted that for a given trajectory, coordinates of the system in the forward and reverse directions are same. Each trajectory integrated in forward and reverse directions were combined together to get a complete trajectory. 150 out of 414 were complete reactive trajectories going from reactants to products. In the remaining 264 trajectories, integration in the forward and reverse directions resulted in either reactants or products.

In order to understand the atomic-level mechanism of the reaction, it is important to investigate various dynamical pathways followed in these 150 trajectories initiated from **mts**. The dynamical pathways were analyzed by using reduced three-dimensional (R3D) representation of reaction pathways recently proposed by Carpenter and coworkers.<sup>75</sup> In this method, principal component analysis (PCA) was carried out on the cartesian coordinates of *IRC* to obtain R3D representation of *IRC*. Figure 4.6 shows PC1, PC2 and PC3, the three largest principal components that represent *IRC* in R3D space. In Figure 4.7, F atom cartesian coordinates are plotted along the *IRC* path in the rotated coordinate system discussed before. It was evident that the cartesian coordinates of F atom along the *IRC* path represents R3D space defined by PC1, PC2 and PC3 components (Figure 4.6(a)) quite well. Therefore, cartesian coordinates of F atom were used to represent *IRC* and the trajectories for clarity. In order to understand

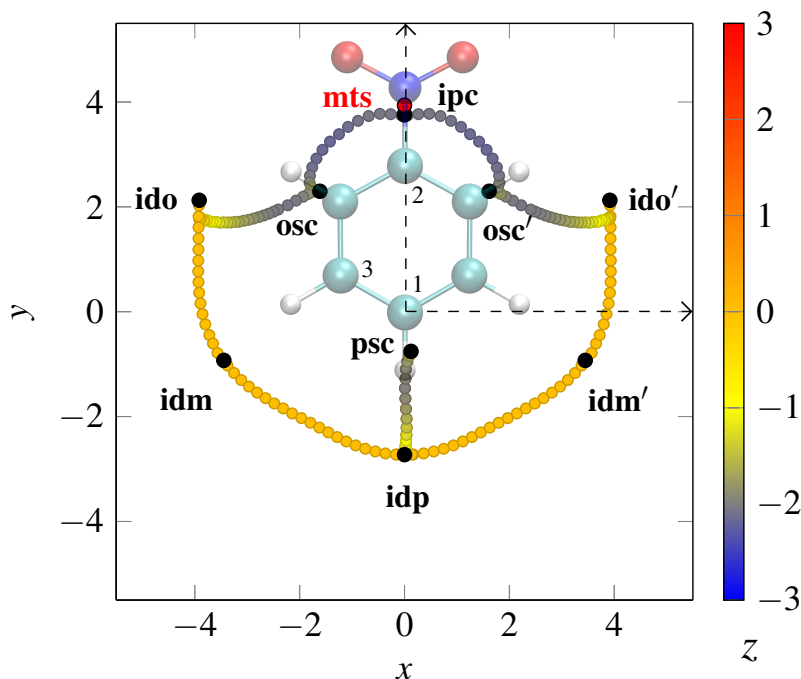


Figure 4.7: Plot of F atom cartesian coordinates in Å along the *IRC* path in the rotated coordinate system. Various stationary point are also shown along the *IRC* path

different mechanisms followed in the trajectories and how much a trajectory deviates from the *IRC* path, the cartesian coordinates of each trajectory was projected on the R3D space which is defined by the three largest principal components PC1, PC2 and PC3. To compute the deviation for a trajectory from *IRC* path in the R3D space, the minimum distance ( $d_{\min}^i$ ) for every point ( $\mathbf{q}^i$ ) in a trajectory was computed from all the *IRC* points ( $\mathbf{q}_{\text{IRC}}^j$ ) using the following equation,

$$d_{\min}^i = \min(\mathbf{q}^i - \mathbf{q}_{\text{IRC}}^j) \quad (4.2)$$

For a trajectory,  $d_{\min}^i$  provides the deviation from the *IRC* path. From the optimized geometries of various **id** complexes, it was found that  $F \cdots H$  was about 1.5 Å. The sum of van der Waal radii of F atom and H atom was 2.5 Å. Qualitatively, a  $d_{\min}$  cut-off of 1 Å (2.5 Å-1.5 Å) was used to define the *IRC* path region, while, a trajectory that deviates by more than 1 Å was categorized as trajectory following non-*IRC* path.

63 out of 150 trajectories had  $d_{\min}$  value of less than 1 Å and followed pathway close

to the MEP. The F atom in 42 of these 63 *IRC* trajectories formed different **id** complexes which isomerized to **osc**. These trajectories then isomerized to **ipc** and formed products via **mts** transition state. A representative trajectory is shown in Figure 4.8(a). As seen in the figure, the trajectory closely followed the MEP pathway with a minimum deviation ( $d_{\min} < 1 \text{ \AA}$ ). In the remaining 21 *IRC* trajectories, it was found that the system was trapped in the **ipc** minimum. Figure 4.8(b) shows a sample trajectory trapped in **ipc** region. It is expected that these trajectories would form reactants if integrated further in the reverse direction. Here, in this study, we assume that all these 21 trajectories formed **ipc** intermediate directly from the reactants and are labelled as trajectories following direct-*IRC* pathway. Interestingly, these trajectories can also be thought of following *concerted* pathway as  $\text{F}^-$  directly attacked the carbon atom bearing the leaving group. 87 out of 150 trajectories showed deviation from MEP ( $d_{\min} > 1 \text{ \AA}$ ) and were labelled as trajectories following non-*IRC* pathway. Figure 4.8(c) shows a non-*IRC* trajectory in which the system does not access the **osc** region and the F atom attacks from the side to form **ipc** intermediate which leads to the formation of products. It was observed that in 21 out of 87 non-*IRC* trajectories, after the formation of **id** complexes, F atom bounces off the nitrobenzene moiety to the weak interaction region and then returns back to form another **id** complexes. It is to be noted that the system skips the formation of **id** complexes when F atom does this motion. This kind of motion depicted by F atom resembled roaming type pathway and these trajectories were labelled as trajectories following *roaming* pathway. In these trajectories, the minimum deviation ( $d_{\min}$ ) was found to be more than 2  $\text{\AA}$ . Figure 4.8(d) shows a representative trajectory that follows roaming pathway. It can be seen that the system skips the formation of **id** complex when F atom roams around the phenyl ring.

It is clear from the analysis of the different pathways that system spends a lot of time in various **id** and  $\sigma$ -complexes before the formation of products. So, to understand the role of various complexes in the mechanism of the reaction, lifetimes of all the intermediates were computed from 150 trajectories initiated at **mts** transition state. The lifetimes are calculated

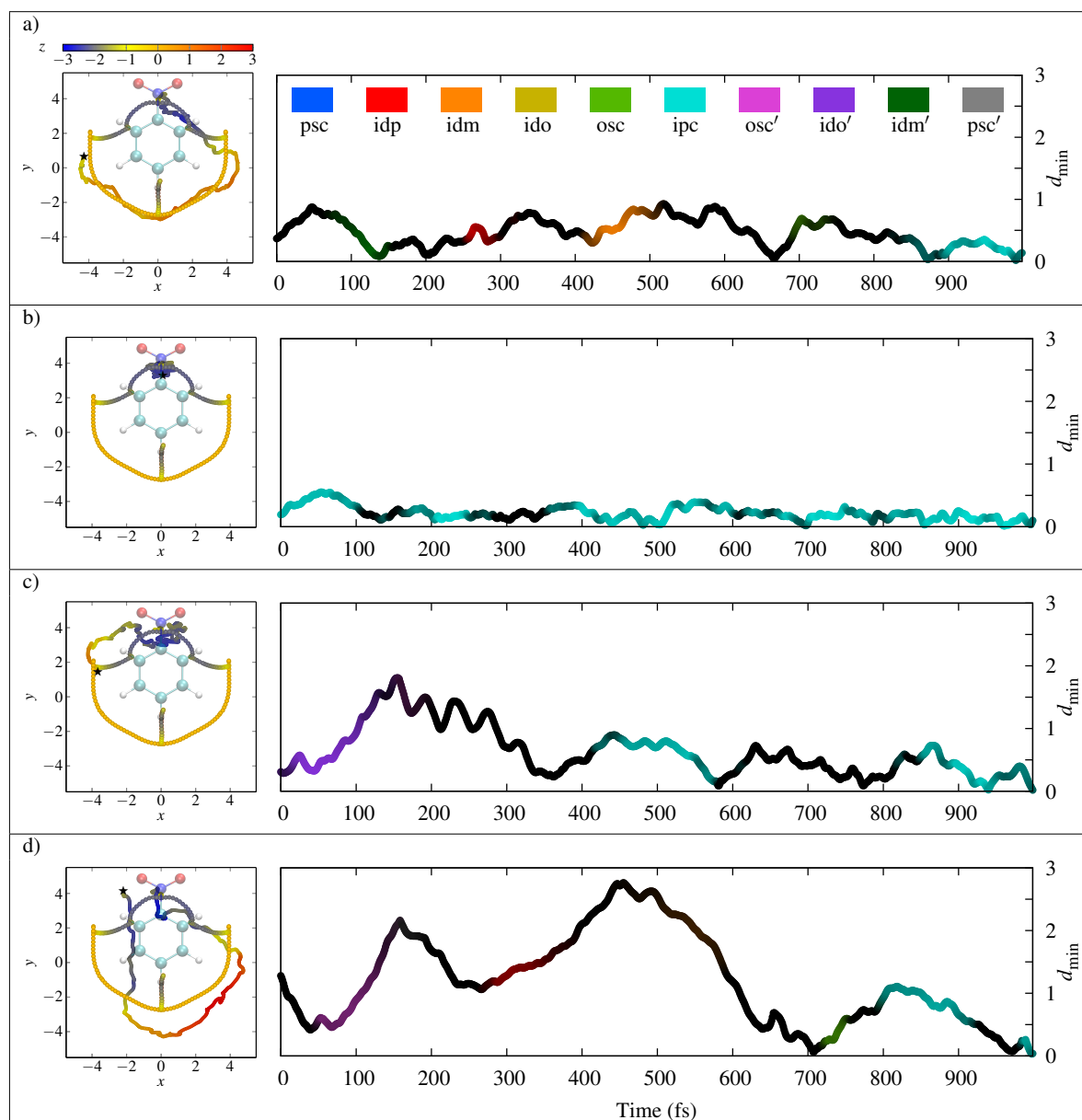


Figure 4.8: Sample trajectories initiated at the transition state **mts** that follow (a) IRC, (b) direct-IRC, (c) non-IRC and (d) roaming pathways. Right: The cartesian coordinates of F atom ( $\text{\AA}$ ) in MEP and in the representative trajectory.  $\star$  denotes the beginning of the trajectory. Left: Plot of minimum deviation from IRC ( $d_{\min}$ ) as a function of time for sample trajectories in the R3D space computed from PCA. The color coding in the right figures indicate stationary point which is closer to a given point in the trajectory

Table 4.2: Geometrical criteria used to define various intermediate region for the calculation of lifetimes of different intermediates.

Intermediate	Criteria <sup>a</sup>
<b>idp</b>	$d(\text{H9-F}) < 2.53 \text{ \AA}$ and $\angle\text{C1-H9-F} < 62.5^\circ$ and $d(\text{H9-F}) \cdot \sin(\angle\text{F-H9-C1}) < 1.97 \text{ \AA}$
<b>psc</b>	$d(\text{C1-F}) < 2.34 \text{ \AA}$ and $\angle\text{H9-C1-F} > 60.0^\circ$
<b>idm</b>	$d(\text{F-H8}) < 2.53 \text{ \AA}$ and $d(\text{F-H8}) \cdot \sin(\angle\text{F-H8-C5}) < 2.19 \text{ \AA}$ for $0^\circ <  \angle\text{F-H8-C5-C4}  < 90^\circ$ (or) $d(\text{F-H8}) < 2.53 \text{ \AA}$ and $d(\text{F-H8}) \cdot \sin(\angle\text{F-H8-C5}) < 1.56 \text{ \AA}$ for $90^\circ \leq  \angle\text{F-H8-C5-C4}  \leq 180^\circ$
<b>idm'</b>	$d(\text{F-H10}) < 2.53 \text{ \AA}$ and $d(\text{F-H10}) \cdot \sin(\angle\text{F-H10-C3}) < 1.56 \text{ \AA}$ for $0^\circ <  \angle\text{F-H10-C3-C6}  < 90^\circ$ (or) $d(\text{F-H10}) < 2.53 \text{ \AA}$ and $d(\text{F-H10}) \cdot \sin(\angle\text{F-H10-C3}) < 2.19 \text{ \AA}$ for $90^\circ \leq  \angle\text{F-H10-C3-C6}  \leq 180^\circ$
<b>ido</b>	$d(\text{F-H11}) < 1.83$ for $0^\circ <  \angle\text{C3-C6-H11-F}  < 35^\circ$ (or) $d(\text{F-H11}) < 2.18$ for $35^\circ <  \angle\text{C3-C6-H11-F}  < 73.2^\circ$
<b>ido'</b>	$d(\text{F-H7}) < 1.83$ for $0^\circ <  \angle\text{C5-C4-H7-F}  < 35^\circ$ (or) $d(\text{F-H7}) < 2.18$ for $35^\circ <  \angle\text{C5-C4-H7-F}  < 73.2^\circ$
<b>osc</b>	$d(\text{C4-F}) < 2.4 \text{ \AA}$ and $76.62^\circ < \angle\text{F-C4-C2} < 119.47^\circ$
<b>osc'</b>	$d(\text{C6-F}) < 2.4 \text{ \AA}$ and $76.62^\circ < \angle\text{F-C6-C2} < 119.47^\circ$
<b>ipc</b>	$d(\text{C2-F}) < 2.5 \text{ \AA}$ , $d(\text{C2-N}) < 1.69 \text{ \AA}$ , $\angle\text{C6-C2-F} > 71.4^\circ$

<sup>a</sup> d represents bond distances.

by computing the time for which the system stayed in an intermediate region. A particular intermediate region is defined by using the geometrical parameters of that intermediate and the transition states it connects to. Table 4.2 shows the criteria used to define different intermediate regions for the computation of lifetimes. The atom indices used were same as shown in Figure 4.3.

The system can enter and leave an intermediate region multiple times in a single trajectory. Each of these events are considered to be individual events and the lifetime is the difference in time when system enters and leaves an intermediate region. Using the criteria listed in Table 4.2, the lifetime distributions of various intermediates were calculated and shown in Figure 4.9. Average lifetimes of various intermediates were found to be quite large as seen in Table 4.3 and the lifetime distributions follow non-exponential behaviour that indicates non-statistical dynamics. Figure 4.9(f) shows the lifetime distribution of **ipc** intermediate just before the product formation. The distribution was non-exponential and shows that the unimolecular dissociation from the intermediate **ipc** is non-statistical in nature. To understand

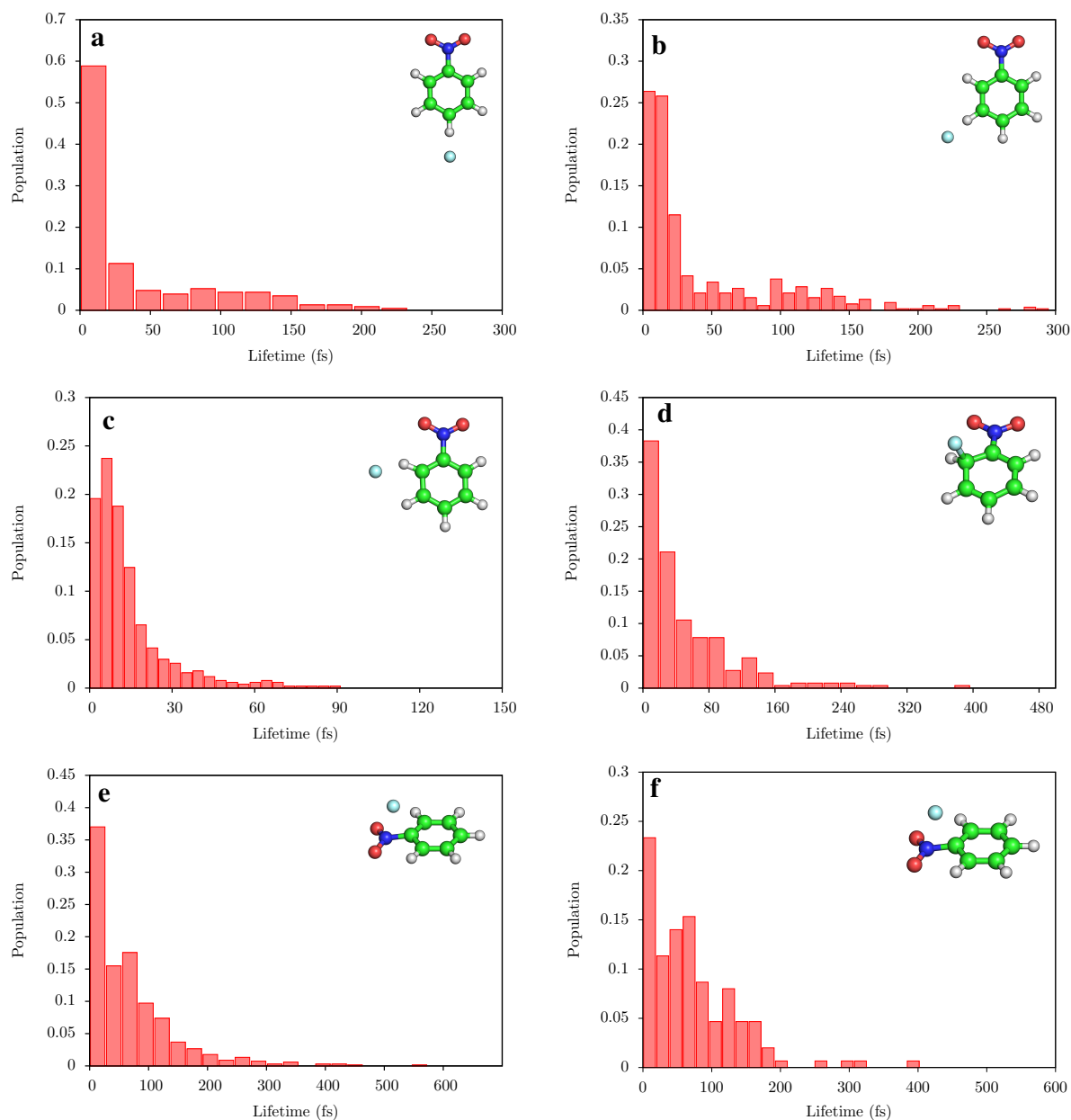
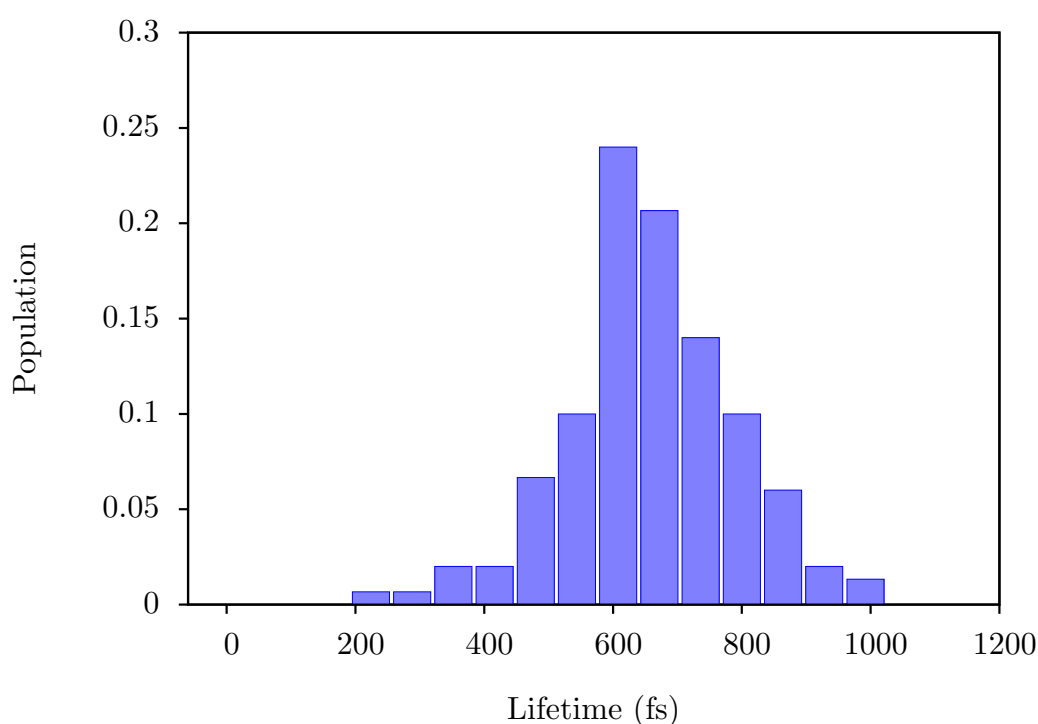


Figure 4.9: Lifetime distribution for (a) **idp**, (b) **idm**, (c) **ido**, (d) **osc**, and (e) **ipc** for 150 reactive trajectories initiated at the transition state **mts**. (f) Lifetime distribution for **ipc** intermediate formed just before the formation of the products

the collective role of all the intermediates in the mechanism of the reaction, total lifetime of all the intermediate regions was computed by adding the lifetimes of all the intermediates during a trajectory. Figure 4.10 shows the distribution of total lifetime in the intermediate region for 150 reactive trajectories initiated at the transition state **mts**. It is clear from this distribution that

Table 4.3: Average lifetimes of various intermediates computed from 150 trajectories initiated at **mts**

Intermediates	Lifetimes	Number of events
<b>idp</b>	40.4	231
<b>psc</b>	32.5	12
<b>idm</b>	44.0	531
<b>ido</b>	14.2	506
<b>osc</b>	49.3	256
<b>ipc</b>	68.8	678

Figure 4.10: Distribution of total lifetime in the intermediate region for the 150 reactive trajectories initiated at **mts** transition state.

the system spends significant amount of time in the intermediate region before the formation of products. 21 out of 150 trajectories followed direct-IRC pathway and can be compared to the single-step concerted pathway followed in  $S_NAr$  reaction because system access only **ipc** intermediate in these trajectories. But the rest of the trajectories that followed IRC and non-IRC pathways do not follow single-step concerted pathway. Instead, these trajectories followed multi-step pathway in which various **id** and  $\sigma$ -complexes were formed before the formation of

the products despite Meisenheimer structure being a transition state (**mts**) on the PES.

## 4.4 Summary and Conclusions

Potential energy profile was mapped for the  $S_NAr$  reaction  $C_6H_5NO_2 + F^- \longrightarrow C_6H_5F + NO_2^-$  using various levels of theory. *Ab initio* classical trajectory simulations were performed to understand the atomic-level mechanism of this reaction using B3LYP/DZVP level of theory. It was found that the dominant mechanism followed in this reaction was multi-step pathway in which various **id** and  $\sigma$ -complexes were formed before the formation of products even though the Meisenheimer structure is a transition state (**mts**) on the PES. Apart from the traditional MEP pathway, majority of the trajectories followed non-IRC and roaming pathways. Lifetimes of various complexes were found to be significantly large and their lifetime distributions were found to be non-exponential indicating non-statistical dynamics.



## DISSOCIATION DYNAMICS OF FORMALDEHYDE ON GRAPHENE SHEET

### 5.1 Introduction

**H**eterogeneous catalysis (HC) is unarguably one of the most important and active areas in the field of catalysis and has impact on various fields. In HC, the rate of the reaction is enhanced due to more surface area, selective formation of product, used for synthesizing products in large scale for industrial applications, etc.<sup>76–78</sup> Gas-surface reaction is a class of HC where reactant is in gas phase and the surface acts as a catalyst. These gas-surface reactions also serve as interesting models to understand the energy transfer between the colliding molecule and the surface. In addition, the study of atomic-level mechanisms and energy transfer at the gas surface interface is important to understand how does the surface affects the dissociation dynamics of unimolecular reactions.<sup>79–81</sup>

Gas-surface reactions can be categorized in two parts. In the first type, metallic surfaces are used which are hard surfaces while in the second, soft surfaces such as graphene are used. Many

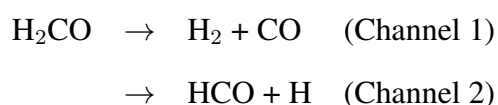
studies have been carried out experimentally<sup>82-85</sup> and theoretically<sup>86-90</sup> using hard and soft surfaces to understand various aspects of gas-surface reactions that include energy and charge transfer at the interface, role of non-adiabatic interactions between reactant molecules and metal surface, effect of mode specificity on dynamics and rate of the reaction. An important aspect of gas-surface reactions is reactive scattering where reactants dissociate due to the collision with the surface. It is important to understand the mechanism of energy transfer at the interface between the reactant molecules and the surface that leads to the dissociation of the reactants to form products.

Density functional theory calculations<sup>91</sup> were carried out to study the dissociation of water on Ni(100) and Ni(111) surfaces. It was observed that H and OH adsorbed on the FCC site in both the surfaces and the energy barrier for the dissociation of H<sub>2</sub>O on Ni(100) is slightly lower than on Ni(111) surface. In another work, dissociation of water on Cu(111) surface using time-dependent wavepacket dynamics was studied<sup>92</sup>. It was observed that dissociation probability depends on various factors like vibration, rotation and initial orientation of the molecule. Various first principles theoretical models based on DFT have been used extensively to understand surface reaction dynamics in different systems.<sup>89</sup> Quantum-state resolved gas-surface reactions of various small molecules with different Ni and Pt surfaces using molecular beam experiments.<sup>93</sup> They were able to clearly show that these gas-surface reactions are bond selective and vibrational mode specific. These studies provided important benchmarks for comparison with various theoretical models. The energy transfer and reaction between gas molecules and carbon based surfaces were also studied by several research groups.<sup>94-97</sup> Wodtke and coworkers<sup>96,97</sup> studied various gas surface collisions using molecular-beam experiments to understand how energy transfer happens between the molecule and the surface.

Various studies were also carried out using soft surfaces. Hase and coworkers<sup>87</sup> studied the dissociation dynamics of chemisorption of <sup>3</sup>O<sub>2</sub> with graphene containing various number of defects by using (5a,6z)-periacene as the model system at high temperature. They carried out

direct dynamics simulations using semi-empirical method PM7/UHF with different collision energy for  $^3\text{O}_2$  and various defects were incorporated in (5a,6z)-periacene by removing C atoms from the sheet. It was established that collision of  $^3\text{O}_2$  with graphene having one, two, three and four defects showed no reactive trajectories. On the other hand, reactive trajectories were observed with higher number of defects (five and six) and also with four defect but with different morphology. It was concluded that morphology plays an important role in dissociative chemisorption. Majewski and coworkers<sup>98</sup> studied dissociative adsorption of  $\text{CH}_4$  on normal and defected graphene sheet by computing reaction free energies using ab initio molecular dynamics (AIMD) method. It was observed that graphene acts as a catalyst in the dissociation of  $\text{CH}_4$ . It was also seen that defects influenced reaction energetics and changed free energy landscapes for both adsorption and dissociation steps. Ciraci and coworkers<sup>99</sup> studied the dissociative adsorption of small molecules on vacancy defects of graphene and silicene by performing first principles calculations using density functional theory (DFT). It was observed that atoms at vacancy defect reconstruct and form active sites which help in the dissociative adsorption of small molecules by lowering the barrier for dissociation. The dissociative adsorption of  $\text{H}_2$  on graphene was studied by various groups computationally. Sugimoto and coworkers<sup>100</sup> used DFT to study dissociative adsorption of  $\text{H}_2$  on graphene and found that  $\text{H}_2$ -graphene interactions depends on reconstruction of carbon atoms in the graphene sheet. It was also concluded that activation barrier of  $\text{H}_2$  dissociation on unrelaxed graphene sheet is more than the relaxed one.

In the present work, the gas-surface reaction between  $\text{H}_2\text{CO}$  and graphene is investigated. Formaldehyde photodissociation reaction is well studied both theoretically<sup>101,102</sup> and experimentally in the gas phase<sup>103–105</sup> due to its small size and well resolved energy levels. The decomposition of  $\text{H}_2\text{CO}$  takes place via multiple pathways to give following products.



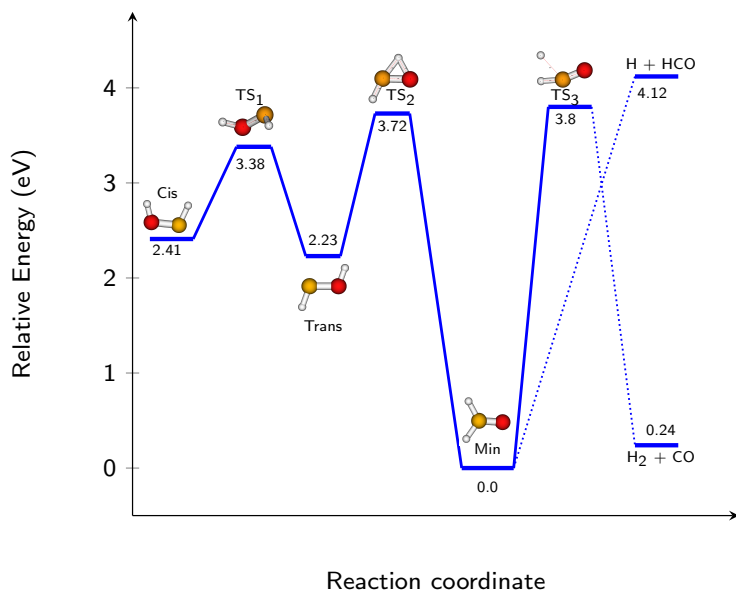


Figure 5.1: Relative energies for minima and saddle points on the ground state PES of formaldehyde.

The energetics of the pathway leading to the two products are shown in Figure 5.1. One of the important aspects of the dissociation reaction is the observation of the roaming atom mechanism in the molecular channel  $\text{H}_2\text{CO} \rightarrow \text{H}_2 + \text{CO}$  resulting in rotationally cold CO and vibrationally excited  $\text{H}_2$ <sup>106</sup>. In the roaming atom mechanism, the dissociating H atom roams around HCO fragment with large C-H distance ( $r_{\text{CH}} > 3 \text{ \AA}$ ) by weak interactions, before it forms the  $\text{H}_2 + \text{CO}$  products. Interestingly, the roaming atom mechanism does not follow the minimum energy path. In this study, dynamics of  $\text{H}_2\text{CO}$  decomposition on a single layer graphene sheet was investigated using classical trajectory simulations. The effect of the graphene sheet on the atomic level mechanism and dynamics was investigated.

## 5.2 Computational methods

To understand the dissociation dynamics of  $\text{H}_2\text{CO}$  in the presence of single graphene sheet, classical trajectory simulations were performed. The total potential energy of the system is

given by

$$V_{\text{total}} = V_{\text{form}} + V_{\text{graphene}} + V_{\text{int}} \quad (5.1)$$

where,  $V_{\text{form}}$ ,  $V_{\text{graphene}}$  and  $V_{\text{int}}$  are potential energies of  $\text{H}_2\text{CO}$ , the graphene sheet and the interaction between  $\text{H}_2\text{CO}$  and graphene sheet respectively.

The potential energy for the graphene sheet is defined using AMBER force field<sup>107</sup> as

$$V_{\text{graphene}} = \sum_{\text{bonds}} k_b(l - l_0)^2 + \sum_{\text{angles}} k_a(\theta - \theta_0)^2 + \sum_{\text{torsions}} \sum_n \frac{1}{2} V_n [1 + \cos(n\omega - \gamma)] + \sum_{j=1}^{N-1} \sum_{i=j+1}^N f_{ij} \left\{ \epsilon_{ij} \left[ \left( \frac{r_{0ij}}{r_{ij}} \right)^{12} - 2 \left( \frac{r_{0ij}}{r_{ij}} \right)^6 \right] + \frac{q_i q_j}{4\pi\epsilon_0 r_{ij}} \right\} \quad (5.2)$$

In equation (5.2), the first two terms represents potential energy due to harmonic stretching, the second terms represents harmonic bending of bonds, the third and fourth terms represent energy due torsional motion and non-bonded interactions, respectively.

The potential energy function for  $\text{H}_2\text{CO}$  was used as described by Bowman and coworkers.<sup>108</sup> They developed a global PES for  $\text{H}_2\text{CO}$  dissociation using *ab initio* data calculated at MRCI/aug-cc-pVTZ and CCSD(T)/aug-cc-pVTZ levels of theory. This PES describes both the radical and the molecular channels along with cis and trans isomerization of  $\text{H}_2\text{CO}$ . The PES is constructed using six local fits joined by switching functions. The functional form of the potential is a direct product, multinomial in Morse variables for six internuclear distances  $r_i$  i.e.,  $R_{\text{CH}_a}$ ,  $R_{\text{CH}_b}$ ,  $R_{\text{CO}}$ ,  $R_{\text{OH}_a}$ ,  $R_{\text{OH}_b}$  and  $R_{\text{HH}}$  respectively:

$$V(r_1 \dots r_6) = \sum_{n_1, n_2, \dots, n_6} \prod_{i=1}^6 (1 - e^{-\alpha(r_i - r_{ie})})^{n_i} \quad (5.3)$$

where,  $n_1 - n_6$  are the set of integers with  $n_3 \leq 3$  and  $n_1 + n_2 + \dots + n_6 \leq 6$ .  $\alpha$  was set to 0.5 in the fit and  $r_{ie}$   $i = 1 - 6$  are the equilibrium geometry values of the molecule at global minima of formaldehyde, ( $r_{1e} = r_{5e} = 3.8215$  bohrs,  $r_{2e} = r_{4e} = 2.0845$  bohrs,  $r_{3e} = r_{6e} = 3.5467$  bohrs).

To account for the interaction between  $\text{H}_2\text{CO}$  and the graphene sheet, interaction potential was developed by Lourderaj and coworkers<sup>109</sup> by using *ab initio* data obtained at LPNO-CEPA/1/CBS level of theory for three orientations, 1,2 and 3 given in Figure 5.2. These

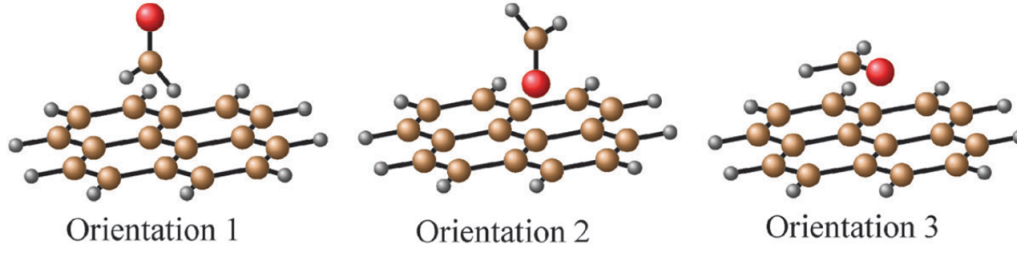


Figure 5.2: Orientations of the  $\text{H}_2\text{CO}$ -pyrene system considered for calculating interaction potential,  $V_{\text{int}}$ .

data points were fitted to an analytical function which was written as the sum of two-body interactions as

$$V_{\text{int}} = \sum_X \sum_Y V_{X \cdots Y} \quad (5.4)$$

where, X represents C atoms of graphene sheet ( $C_g$ ) and Y represents C, H and O atoms of  $\text{H}_2\text{CO}$ . The two body energy function used to describe different interactions ( $C_g \cdots C$ ,  $C_g \cdots O$  and  $C_g \cdots H$ ) is given as

$$V_{X \cdots Y} = A \exp[-Br] + f(r) \left[ \frac{C}{r^2} + \frac{D}{r^4} + \frac{E}{r^6} + \frac{F}{r^8} \right] \quad (5.5)$$

where,

$$\begin{aligned} f(r) &= \exp \left[ - \left( \frac{R_0}{r} - 1 \right)^2 \right], \text{ for } r < R_0 \\ &= 1, \text{ for } r \geq R_0 \end{aligned}$$

where,  $r$  is the internuclear distance between two atoms and  $A, B, C, D, E, F$  and  $R$  are fitting parameters. The values of these parameters obtained from the fit are listed in Table 5.1

Table 5.1: Parameters for H<sub>2</sub>CO - graphene interaction obtained from the fit

	<i>A</i>	<i>B</i>	<i>C</i>	<i>D</i>	<i>E</i>	<i>F</i>	<i>R</i> <sub>0</sub>
<b>C..C</b>	8305	2.87	1.00	-55.40	-145	-2184	2.4
<b>C..O</b>	42624	3.36	0.81	84.80	-1442	-3720	2.4
<b>C..H</b>	9719	3.50	-1.00	1.85	-222	-344	2.3

It is worth pointing out that  $V_{\text{int}}$  represents interaction only for the equilibrium geometries of H<sub>2</sub>CO and graphene. But during the reaction, the geometries of H<sub>2</sub>CO change as the molecule dissociates. It is assumed that  $V_{\text{int}}$  does not change significantly during the dissociation of H<sub>2</sub>CO.

To understand the dissociation dynamics of H<sub>2</sub>CO on graphene sheet, classical trajectories were computed. Initial coordinates and momenta were selected using quasiclassical sampling procedure.<sup>5</sup> Initial conditions for H<sub>2</sub>CO were sampled using a quantum microcanonical procedure<sup>110</sup> with a fixed vibrational energy ( $E_{\text{vib}}$ ). Rotational energies were sampled from a Boltzmann distribution at a given temperature.

A graphene sheet of 100 Å × 100 Å in dimensions that contains 3984 carbon atoms was used for the trajectory simulations. To avoid the formation of a tubular structure by folding of the boundaries, the four carbon atoms at the corner were fixed. It is important to note that the graphene sheet used in the simulations was large enough to model an infinite sized graphene sheet. H<sub>2</sub>CO was placed at a distance of 15 Å above the graphene sheet. The interaction potential between H<sub>2</sub>CO and C atoms at this distance was only about  $1.8 \times 10^{-5}$  kcal/mol.

The initial conditions for the graphene sheet was chosen by assigning velocities corresponding to a given temperature. The surface was then equalibrated for a total of 80 ps to attain Maxwell-Boltzmann distribution at that temperature. In the first 40 ps of equalibration, the velocities of carbon atoms were rescaled using velocity rescaling algorithm to attain desired temperature. The graphene sheet was then equalibrated for another 40 ps. A time step of 0.05

fs was used to integrate the trajectories for 10 ps using velocity-Verlet algorithm.

The trajectories that lead to the product formation were terminated and product energies were then partitioned to rotational, translational and vibrational energies. The vibrational and rotational quantum numbers were then computed using Einstein-Brillouin-Keller (EBK) semiclassical quantization of the action integral.<sup>111</sup>

## 5.3 Results and discussion

Classical trajectory simulations were performed to investigate the effect of vibrational energy of H<sub>2</sub>CO, sheet temperature, orientation of H<sub>2</sub>CO and collision energy on the dissociation dynamics of H<sub>2</sub>CO on single graphene sheet.

### 5.3.1 Effect of Vibrational Energy of H<sub>2</sub>CO

To understand the effect of vibrational energy of H<sub>2</sub>CO on dissociation dynamics of H<sub>2</sub>CO, classical trajectories were performed. Quantum microcanonical sampling<sup>110</sup> was used for H<sub>2</sub>CO with fixed vibrational energies of 3.7 eV, 3.8 eV, 4.2 eV, 4.37 eV and 4.46 eV. It is important to note that 3.8 eV corresponds to classical barrier for H<sub>2</sub> + CO path whereas, 4.2 eV and 4.46 eV are H<sub>2</sub> + CO barrier height and H + HCO threshold including zero-point energy, respectively. Also, 4.1 eV corresponds to the classical threshold for radical channel (H + HCO). To investigate only the effect of vibrational energy of H<sub>2</sub>CO on the dynamics, a very low relative translational energy of 0.1 eV was used for the simulations. With this relative translational energy, H<sub>2</sub>CO was directed towards the center of the graphene sheet. A total of 2000 trajectories for each vibrational energy were computed.

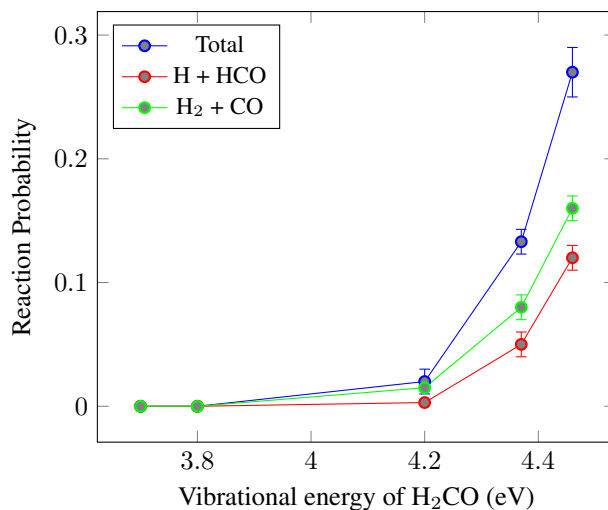


Figure 5.3: Reaction probability as a function of H<sub>2</sub>CO vibrational energy

Figure 5.3 shows the plot of total reaction probability as a function of vibrational energy of H<sub>2</sub>CO. As expected, it can be seen that total reaction probability increases with the increase of vibrational energy of H<sub>2</sub>CO. It was also observed that reaction probability of individual channels also increases as vibrational energy increases. At low vibrational energy of H<sub>2</sub>CO (3.7 eV and 3.8 eV), none of the trajectories gave products. Interestingly, reaction probability for the molecular channel increases more as compared to that of radical channel with increase in H<sub>2</sub>CO vibrational energy because radical channel needs 0.32 eV more energy than molecular channel.

### 5.3.2 Effect of Orientation of H<sub>2</sub>CO

To understand the orientation effect of H<sub>2</sub>CO, four different orientations of H<sub>2</sub>CO were considered with respect to graphene sheet and investigated. Figure 5.4 shows four different orientations of H<sub>2</sub>CO namely, Orientation 1 (O1), Orientation 2 (O2), Orientation 3 (O3), and Orientation 4 (O4). In these calculations, the initial orientation was fixed at these geometries and no extra rotational energy was provided for the collision. In orientations 1 and 4, H<sub>2</sub>CO approaches graphene sheet with 2 H atoms and 1 H atom, respectively. In orientation 2, H<sub>2</sub>CO approaches

graphene with O atom and in orientation 3,  $\text{H}_2\text{CO}$  approaches graphene sheet in a parallel fashion with all the 4 atoms of  $\text{H}_2\text{CO}$  in a plane.

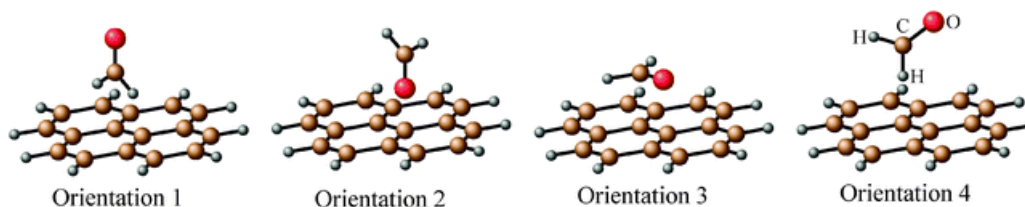


Figure 5.4: Four different orientations of  $\text{H}_2\text{CO}$  with respect to graphene considered in the trajectory simulations.

Classical trajectory simulations were performed for the four orientations discussed above at different collision energies of 0.1 eV, 0.5 eV, 1.0 eV, 1.5 eV and 2.0 eV. Quasi-classical microcanonical sampling<sup>110</sup> was used for  $\text{H}_2\text{CO}$  with a vibrational energies of 4.46 eV. This is the same energy as used for gas phase study of dissociation dynamics of formaldehyde<sup>106</sup>. A total of 1000 trajectories were computed for each combination of four orientations and different collision energies. The reaction probability obtained from the analysis of classical trajectory simulations are summarized in Table 5.2 and the total reaction probability as a function of collision energy for the four different orientations is shown in Figure 5.5. It can be seen that the reaction probability increases as collision energy increases for all the orientations.

Orientation 1 in which  $\text{H}_2\text{CO}$  approaches graphene sheet with two H atoms has least reaction probability at all the collision energies. Interestingly, at lower collision energies (0.1 eV and 0.5 eV), it was observed that orientations 2 and 3 have higher reaction probabilities as compared to other orientations. It is important to note that in orientations 2 and 3, oxygen atom is closer to the graphene sheet. So this orientational effect is seen due to the repulsion between oxygen atom of  $\text{H}_2\text{CO}$  and graphene sheet. On the other hand, at high collision energy (2 eV), orientation 4 in which  $\text{H}_2\text{CO}$  approaches the graphene sheet with one H gave highest reaction probability as compared to other orientations.

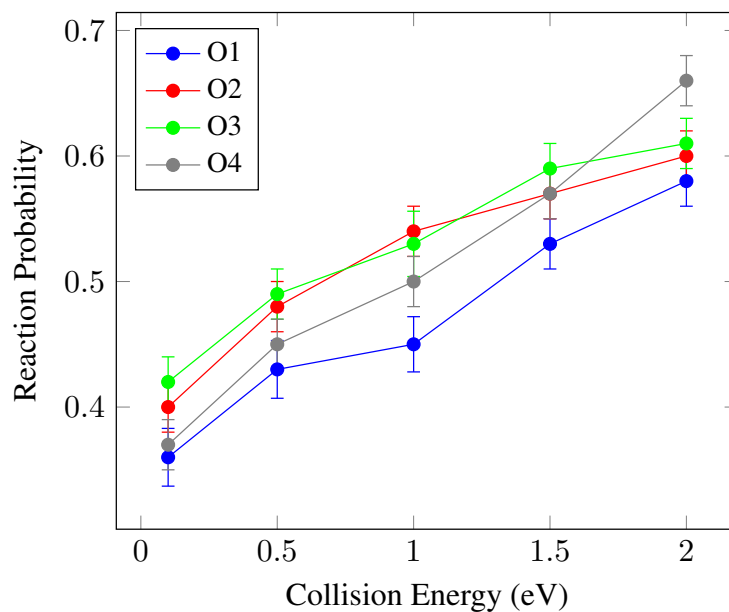


Figure 5.5: Reaction probability as a function of different collision energies for four different orientations of  $\text{H}_2\text{CO}$ .

Table 5.2: Reaction probabilities for different orientations and Collision energy

Collision Energy (eV)	Orientation	$P_{(\text{H}_2 + \text{CO})}$	$P_{(\text{H} + \text{HCO})}$	$P_{\text{Total}}$
0.1	Orientation 1	0.21	0.15	0.36
0.1	Orientation 2	0.19	0.20	0.40
0.1	Orientation 3	0.20	0.22	0.42
0.1	Orientation 4	0.22	0.16	0.37
0.5	Orientation 1	0.20	0.23	0.43
0.5	Orientation 2	0.23	0.25	0.48
0.5	Orientation 3	0.22	0.27	0.49
0.5	Orientation 4	0.18	0.27	0.45
1.0	Orientation 1	0.20	0.25	0.45
1.0	Orientation 2	0.23	0.31	0.54
1.0	Orientation 3	0.24	0.30	0.54
1.0	Orientation 4	0.21	0.30	0.51
1.5	Orientation 1	0.21	0.33	0.54
1.5	Orientation 2	0.23	0.34	0.57
1.5	Orientation 3	0.23	0.36	0.59
1.5	Orientation 4	0.20	0.37	0.57
2.0	Orientation 1	0.18	0.40	0.58
2.0	Orientation 2	0.20	0.40	0.60
2.0	Orientation 3	0.21	0.42	0.61
2.0	Orientation 4	0.18	0.48	0.66

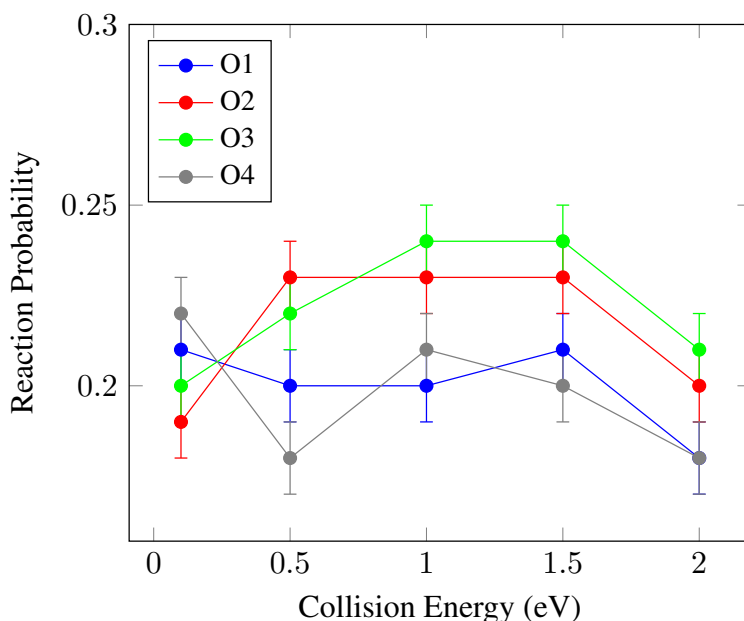


Figure 5.6: Reaction probability as a function of collision energy for  $\text{H}_2 + \text{CO}$  channel.

Figure 5.6 shows the plot of the reaction probability for molecular channel ( $\text{H}_2 + \text{CO}$  product) as a function of different collision energies. It was observed that for Orientation 2 and 3 reaction probability for  $\text{H}_2 + \text{CO}$  channel first increases then decreases with increase in collision energy and was higher than orientation 1 and 4 for all the collision energies except 0.1 eV. It is to be noted that the orientations 2 and 3 are those in which oxygen atom of  $\text{H}_2\text{CO}$  faces the graphene sheet.

Figure 5.7 shows the variation of the reaction probability at different collision energies for the formation of radical product ( $\text{H} + \text{HCO}$ ). Unlike molecular channel, the reaction probability for the radical channel increases throughout with the increase in collision energy. It was observed that at low collision energy (0.1 eV), orientations 2 and 3 gave more radical products. On the other hand, at high collision energy (2 eV), orientation 4 in which  $\text{H}_2\text{CO}$  approaches the graphene with one H atom gave more radical products when compared to other orientations. The reaction probability for orientation 4 increases quite sharply from 1.5 eV to 2 eV. An orientational effect was observed at high collision energy with orientation 4 giving more radical

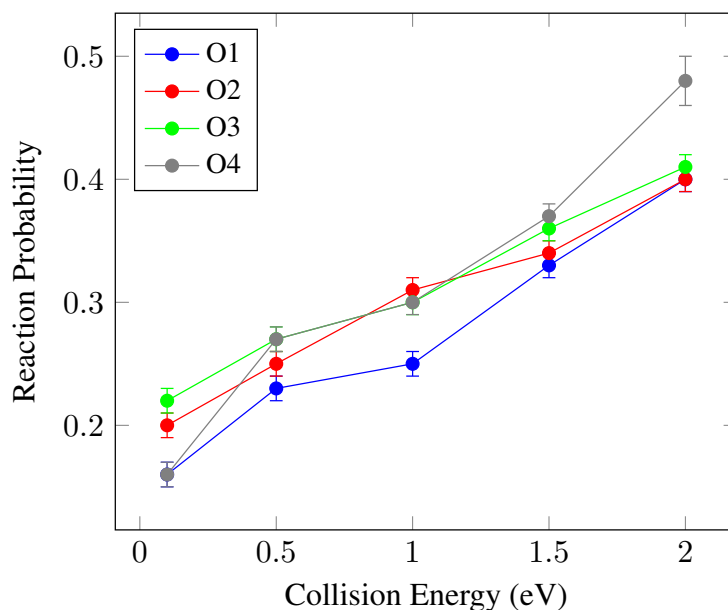


Figure 5.7: Reaction probability as a function of collision energy for H + HCO channel.

product as compared to other orientations.

Figure 5.8 shows the plot of the total reaction probability as a function of collision energy for randomly chosen orientations of  $\text{H}_2\text{CO}$ . The total reaction probability increases with the increase in collision energy which can also be seen in Figure 5.5 for four different orientations. The reaction probability for the radical channel follows a similar trend as that of total reaction probability and increases as collision energy increases which can also be seen in Figure 5.7 for different orientations. On the contrary, and as seen in Figure 5.6 for four different orientations, the reaction probability of molecular channel first increases from 0.1 to 0.5 eV and then decreases as collision energy increases.

### 5.3.3 Roaming atom mechanism

In the gas phase dissociation of  $\text{H}_2\text{CO}$ , it was observed that molecular product can either be obtained through tight transition state  $\text{TS}_3$  or through a roaming pathway in which one of the H atom of  $\text{H}_2\text{CO}$  detaches from HCO moiety, roams around this moiety and abstracts the other

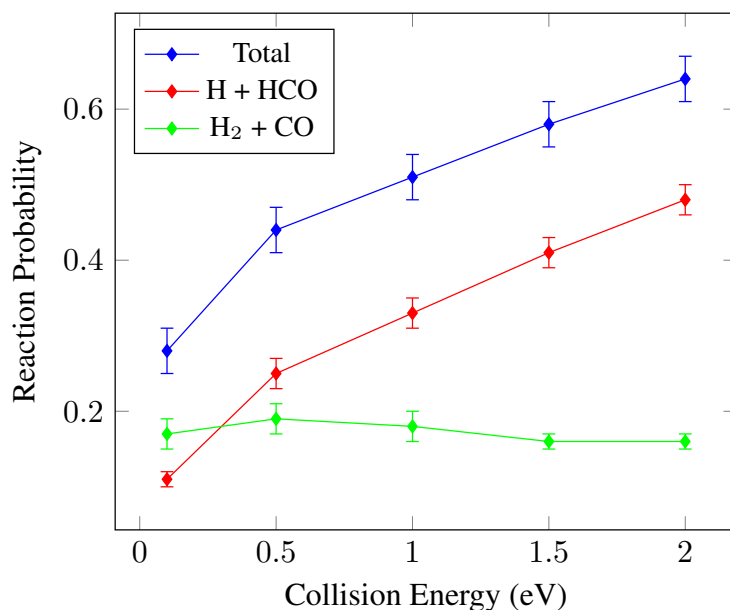


Figure 5.8: Reaction probability as a function of collision energy for random orientations.

H atom to form molecular product. This resulted in vibrationally hot H<sub>2</sub> and rotationally cold CO products.<sup>106</sup> It was observed that about 18-20% of molecular product formed in the gas phase dissociation of H<sub>2</sub>CO is through roaming atom mechanism. It is of interest to know if the roaming atom mechanism exists in the H<sub>2</sub>CO-graphene collision reaction. In order to identify trajectories in which roaming atom mechanism was followed, the H–H and C–H distances were followed as a function of time. If one of the C–H distances remained between 3-4.5 Å before forming H<sub>2</sub> molecule, the trajectory was labeled as roaming trajectory. Interestingly, it was observed that only 7-10% of molecular product were formed via the roaming atom mechanism in the presence of graphene sheet. Thus, 50% decrease in the roaming atom mechanism in the presence of graphene sheet was observed. To understand the effect of collision energy on various pathways, reaction probability for different pathways were plotted as a function of collision energy in Figure 5.9. At the low collision energy of 0.1 eV, the reaction probability of molecular channel is more than the radical channel and at higher collision energies, radical product dominates. Interestingly, the reaction probability of molecular channel formed via

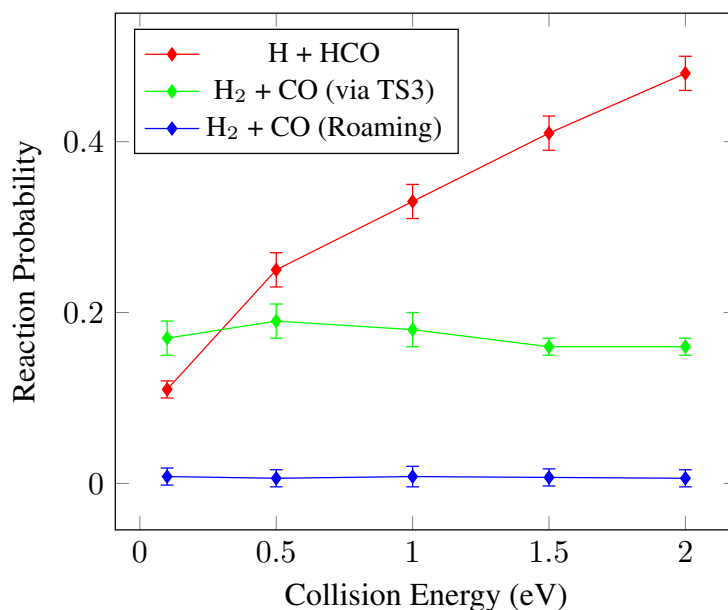


Figure 5.9: Reaction probability as a function of collision energy for three different pathways.

roaming atom mechanism did not change much as a function of collision energy even though the reaction probability of molecular channel formed via **TS**<sub>3</sub> decreases when collision energy increases.

As discussed above, the roaming atom pathway is characterized by the formation of rotationally cold CO and vibrationally hot H<sub>2</sub> products. It is interesting to see the effect of graphene sheet on the vibrational and rotational distributions of H<sub>2</sub> and CO, respectively. To this end, the gas-surface simulation results were compared to that obtained in the gas phase. here, the gas phase simulations were performed by using a quantum microcanonical sampling procedure with a vibrational energy of 4.43 eV and rotational temperature of 10 K. A total of 6000 trajectories were calculated in the gas phase. Figure 5.10 shows the vibrational state distribution of H<sub>2</sub> formed during the gas-phase dissociation of H<sub>2</sub>CO and when H<sub>2</sub>CO dissociates on graphene sheet at low (0.1 eV) and high (2 eV) collision energies. All the three distributions followed similar trend where the population decreases as vibrational quantum number increases. Interestingly, an increase in the population of excited states of H<sub>2</sub> was

observed when collision energy was increased from 0.1 eV to 2 eV.

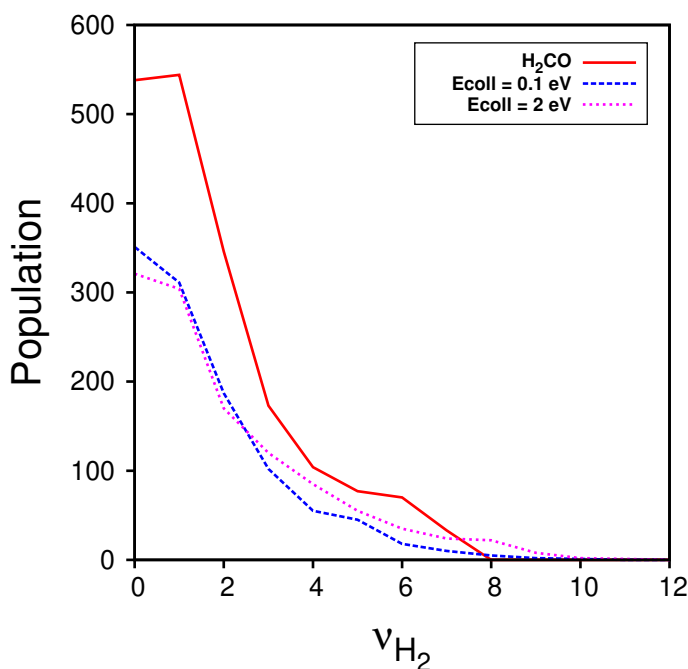


Figure 5.10: Vibrational state distribution of H<sub>2</sub> products ( $\nu_{H_2}$ ) formed in gas-phase dissociation and in the dissociation of H<sub>2</sub>CO on graphene.

It is also interesting to see the effect of the graphene sheet on the rotational distribution of CO products at low and high collision energies and compare them with that of the rotational distribution obtained in the gas phase dissociation of H<sub>2</sub>CO. Figure 5.11 shows three different rotational distributions of CO products. It is evident that all the three distributions follow a similar trend along with a small shoulder at low  $J$  values corresponding to products formed by roaming atom mechanism. Interestingly, at high collision energy, more CO molecules are formed at higher rotational states.

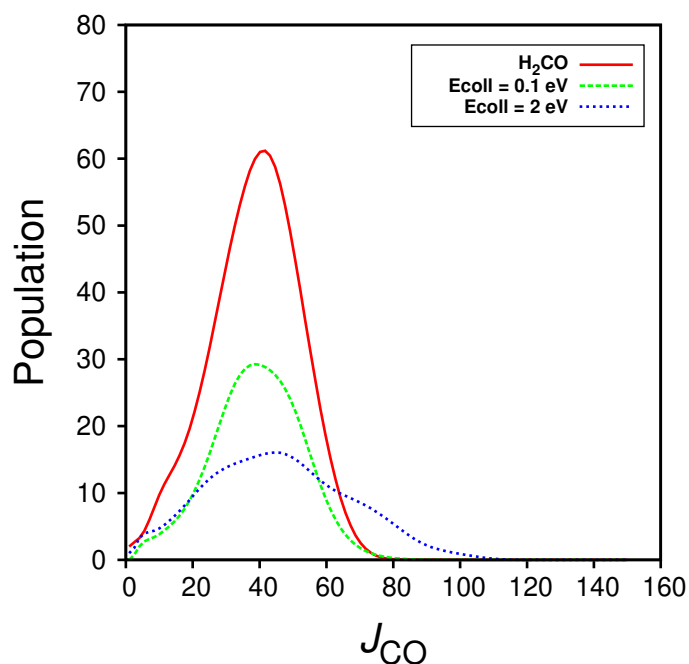


Figure 5.11: Rotational state distribution of H<sub>2</sub> products ( $J_{CO}$ ) formed in gas-phase dissociation and in the dissociation of H<sub>2</sub>CO on graphene.

## 5.4 Summary

Classical trajectory simulations were performed to understand the effect of graphene sheet on the dissociation dynamics of H<sub>2</sub>CO. The effect of various factors like vibrational energy of H<sub>2</sub>CO, orientations of H<sub>2</sub>CO and collision energy were investigated. It was found that as vibrational energy of H<sub>2</sub>CO increases, total reaction probability along with the the reaction probability of both the channels increases. At low collision energy, orientations 2 and 3 gave more products, while, at high collision energy, orientation 4 gave more products. With increase in collision energy, the reaction probability of the radical channel was found to increase and on the other hand, reaction probability for molecular channel decreased. The reaction probability of roaming pathway did not change much as a function of collision energy. A 50% decrease in the roaming atom mechanism was observed in the presence of graphene sheet. In addition, increase in collision energy, H<sub>2</sub> and CO products were formed in higher vibrational and rotational states, respectively.



## EFFECT OF CONFINEMENT ON DISSOCIATION DYNAMICS OF FORMALDEHYDE

### 6.1 Introduction

Chemical reactions are affected by various factors such as temperature, pressure, catalysts, etc. It is of fundamental interest to understand the mechanism of chemical reactions under these conditions to enhance reactivity or selectively form one product of interest. Another factor that can alter chemical reactions is confinement. There are several experimental studies where reactions were performed in microporous and nanoporous materials and it was observed that confinement affected chemical reactions and their outcome.<sup>112,113</sup> Various metal organic frameworks (MOFs) and zeolites are examples of such materials. These materials enhance rate of the reaction by increasing the contact area between the reaction mixture and catalysts if any. It is also found that in some cases, these materials selectively adsorb one of the products and thus lead to the formation of a selective product in the reaction.<sup>113</sup>

The factors that affect reactions in confinement can be broadly classified into three classes: (i) shape-catalytic effects, (ii) physical or soft effects, and chemical or hard effects. The chemical reactions catalyzed by zeolites are good examples of shape-catalytic effects.<sup>114</sup> In these reactions, the shape of the confining material dictates the pathways of the reaction. The interactions of reactant molecules with the confining structure of the zeolite determines the chemical pathways allowed in the reaction. The methylation of toluene to form para-xylene using zeolite HZSM-5 as catalyst is a good example that shows shape-catalytic effects.<sup>113</sup> Physical or soft effects include electrostatic and dispersion interactions between the reactant molecules and the confining material which affect the mechanism of chemical reactions.

In chemical and hard effects, the reaction mixture and the confining material involve in making and breaking of chemical bonds between reactant and confining material. This significant electron rearrangement alters the rate and mechanisms of the reactions.<sup>115,116</sup> Due to effective surface-molecule interactions, molecules in confined space and molecules adsorbed on the surface show different thermodynamic properties as compared to bulk material. It is reported recently that the carbon based materials such as carbon nanotubes (CNT), graphene and fullerenes can also influence chemical reactions because of their large surface area and extended  $\pi$ -conjugation.<sup>117-119</sup> Graphene and CNTs are particularly used to understand chemical reactions in confinement due to large polarizability and flexibility.

In this work, the effect of confinement on the dissociation dynamics of  $\text{H}_2\text{CO}$  was studied using two models: (i)  $\text{H}_2\text{CO}$  between two graphene sheets and (ii)  $\text{H}_2\text{CO}$  inside single-walled carbon nanotube. To this end, classical trajectory simulations were performed to understand the effect of confinement on the mechanisms and dynamics of the reactions.

## 6.2 Computational Methods

The effect of confinement was studied by performing classical trajectory simulations of the dissociation dynamics of  $\text{H}_2\text{CO}$  inside two graphene sheets. The total potential energy of the

system is written as

$$V_{\text{total}} = V_{\text{form}} + V_{\text{graphene}} + V_{\text{int}} \quad (6.1)$$

where,  $V_{\text{form}}$ ,  $V_{\text{graphene}}$  and  $V_{\text{int}}$  in Equation 6.1 are potential energies of  $\text{H}_2\text{CO}$ , the graphene sheet and the interaction between  $\text{H}_2\text{CO}$  and both the graphene sheets, respectively.

The potential energy for the graphene sheet is defined using AMBER force field<sup>107</sup>. The interactions between the two graphene sheets was described by Lennard-Jones potential using AMBER force field parameters.

As discussed in the previous chapter, the potential energy function for  $\text{H}_2\text{CO}$  was used as described by Bowman and coworkers<sup>108</sup> as discussed in Chapter 5. To account for the interaction between  $\text{H}_2\text{CO}$  and the two graphene sheets, interaction potential was developed by Lourderaj and coworkers<sup>109</sup> and is discussed in Chapter 5.

The initial conditions for  $\text{H}_2\text{CO}$  were sampled using a quantum microcanonical procedure<sup>110</sup> with a fixed vibrational energy. Rotational energies were sampled from a Boltzmann distribution at a given temperature. Two graphene sheets of  $50 \text{ \AA} \times 50 \text{ \AA}$  in dimensions that contain 1032 carbon atoms each were used for the trajectory simulations.  $\text{H}_2\text{CO}$  was placed at the mid point of the two graphene sheets. The initial conditions for both the graphene sheets was chosen by assigning velocities corresponding to a given temperature. The surface was then equilibrated for a total of 80 ps to attain Maxwell-Boltzmann distribution at that temperature. In the first 40 ps of equilibration, the velocities of carbon atoms were rescaled using velocity rescaling algorithm to attain desired temperature. The graphene sheet was then equilibrated for another 40 ps. A time step of 0.05 fs was used to integrate the trajectories for 10 ps using the velocity-Verlet algorithm.

To model the CNT, the following potential energy function was used.

$$V_{\text{nano}} = \sum_{\text{bonds}} k_{Cr}(\epsilon_{ij} - 1)^2 + \sum_{\text{angles}} k_{C\theta}(\theta - \theta_0)^2 + \sum_{\text{torsions}} K_{ijkl}(1 - 2\cos\phi_{ijkl}) \quad (6.2)$$

where,  $\epsilon_{ij} = e^{-\gamma(r_{ij}-r_C)}$ ,  $K_{Cr}$ ,  $K_{C\theta}$  and  $K_{C\phi}$  are the force constants and  $r_C$ ,  $\theta_C$  and  $\phi_C$  are the equilibrium parameters. In this equation, the first, second and third terms are potentials for

Morse bond, harmonic bending and a two fold torsion, respectively. The parameters given by Walther and coworkers<sup>120</sup> were used in the calculations.

## 6.3 Results and discussions

To understand the effect of confinement on the dissociation dynamics of  $\text{H}_2\text{CO}$ , two models system were used: (i)  $\text{H}_2\text{CO}$  between the two graphene sheets and (ii)  $\text{H}_2\text{CO}$  inside a single-walled carbon nanotube.

### 6.3.1 $\text{H}_2\text{CO}$ confined between two graphene sheets

Figure 6.1 shows a model system used to study the dissociation dynamics of  $\text{H}_2\text{CO}$  between the two graphene sheets. To understand the effect of pore size, four sets of simulations were carried out in which the two graphene sheets was kept at distances 12.5 Å, 15 Å, 17.5 Å and 20 Å away from each other. Microcanonical sampling was used for  $\text{H}_2\text{CO}$  for a fixed vibrational energy of 102.9 kcal/mol, while the rotational energy corresponding to 10 K was provided to  $\text{H}_2\text{CO}$ . This temperature corresponds to typical thermal environment in a molecular beam setup

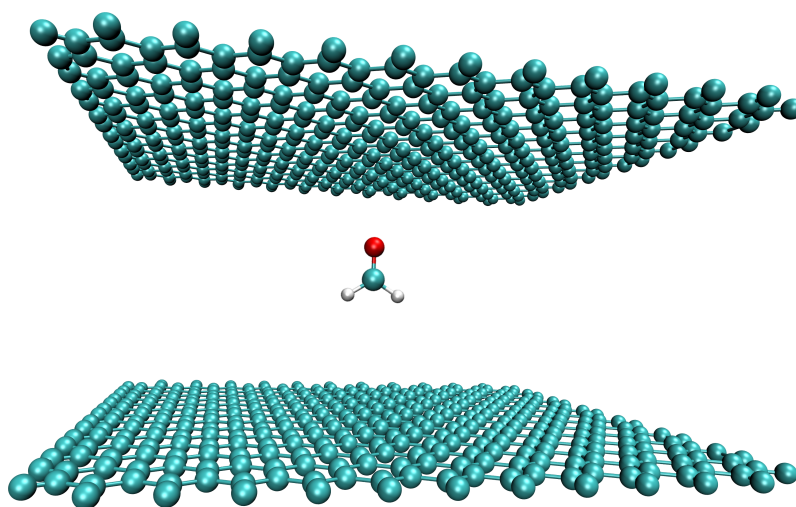


Figure 6.1: Model for  $\text{H}_2\text{CO}$  confined between two graphene sheets.

for gas-surface experiments.  $\text{H}_2\text{CO}$  was placed at the mid point between the two graphene sheets. To see the effect of confinement, no excess translational energy was provided. A total of 800 trajectories were integrated for 10 ps using velocity-Verlet algorithm.

Figure 6.2 shows the total reaction probability along with the reaction probability of both the molecular and radical channel as a function of distance between the two graphene sheets. Interestingly, it was observed that as the distance between the two graphene sheets (pore-size) decreased, the reaction probability also decreased. It is important to note that irrespective of the pore-size, more molecular products were formed than the radical products. The reaction probability did not change much in going from poresize 15 Å to 12.5 Å and reached saturation for both the product channels. The rate of decrease of reaction probability in going from 20 Å to 15 Å was found to be more for the  $\text{H} + \text{HCO}$  channel as compared to the  $\text{H}_2 + \text{CO}$  channel. It is worth pointing out that no molecular product was formed via the roaming atom mechanism.

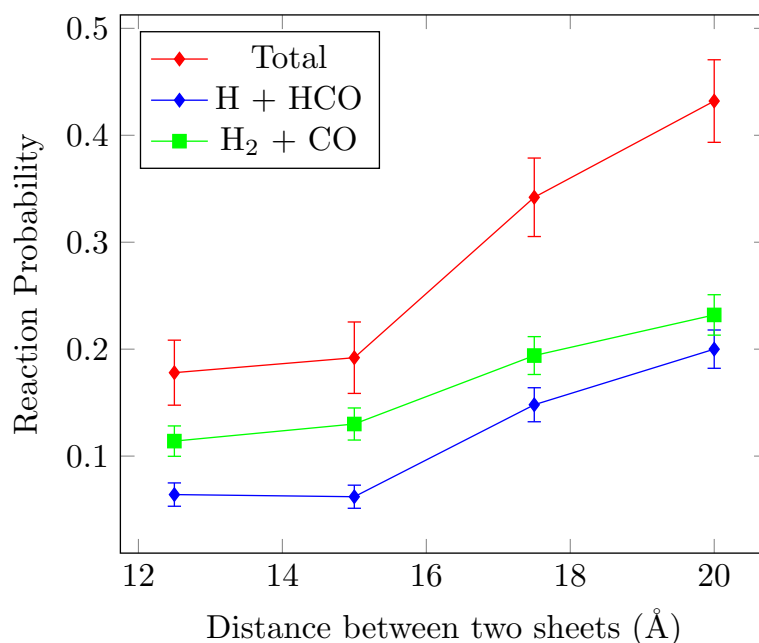


Figure 6.2: Reaction probability as a function of distance between the two graphene sheets.

It is interesting to investigate the dynamics of formaldehyde inside the pore. Figure 6.3a shows the plot of the  $z$ -component of the carbon atom of the formaldehyde during the dissociation process for three representative trajectories when the two sheets are placed 20 Å apart. It can be seen that H<sub>2</sub>CO moves towards the top graphene sheet and then breaks. In one of the trajectories (green) the H<sub>2</sub>CO bounces of the graphene sheet before the bond breaking, in another (red) H<sub>2</sub>CO breaks near the surface and in the third trajectory (blue) the dissociation happens before the collision on the graphene sheet.

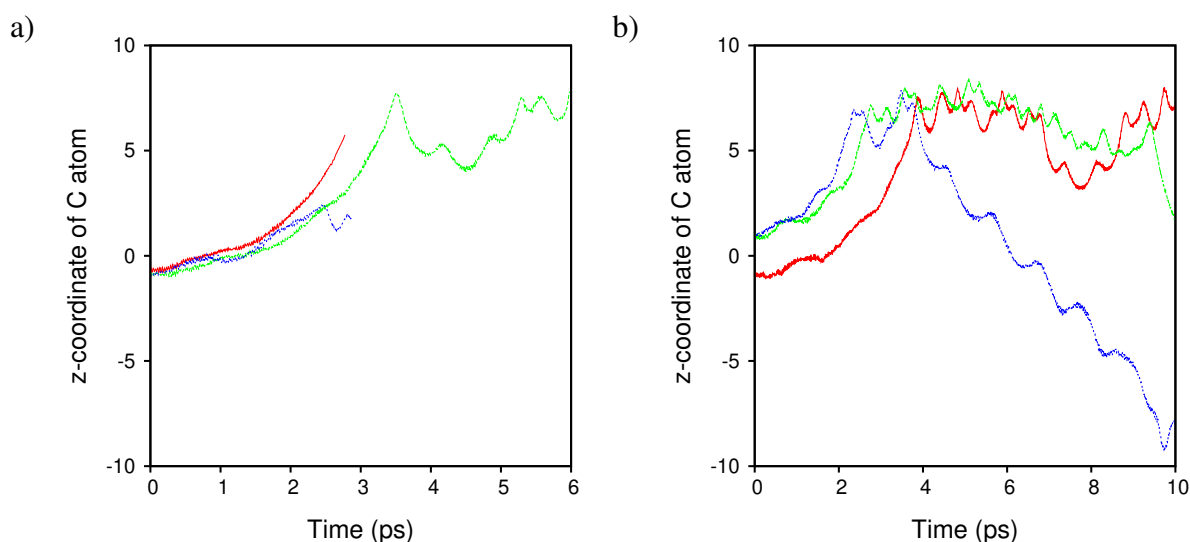


Figure 6.3: Plot of  $z$ -component of the coordinates (Å) for C atom of H<sub>2</sub>CO vs time for three representative (a) reactive and (b) non-reactive trajectories. The two graphene sheets are placed 20 Å apart.

Figure 6.3b shows the the plot of the  $z$ -component of the carbon atom of the formaldehyde for three representative non-reactive trajectories. In two of the trajectories (green and red) H<sub>2</sub>CO exhibits multiple bounces on the top graphene sheet. However, in the third trajectory (blue), H<sub>2</sub>CO is seen bouncing between the two graphene sheets. It is expected that in these trajectories H<sub>2</sub>CO dissipates energy to the surface due to H<sub>2</sub>CO-graphene interaction and thus not acquire the required energy to dissociate.

### 6.3.2 H<sub>2</sub>CO confined inside a single-walled carbon nanotube

Figure 6.4 shows a model system that was used to study the effect of confinement on the dissociation dynamics of H<sub>2</sub>CO when H<sub>2</sub>CO was confined inside a single-walled carbon nanotube. Nanotubes of length 30 Å having diameter 20 Å, 16.5 Å and 12.5 Å was used

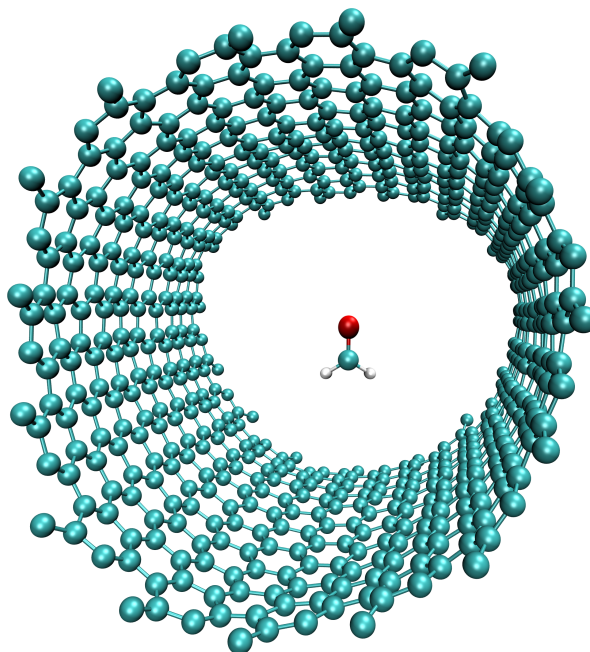


Figure 6.4: Model for H<sub>2</sub>CO confined inside single-walled nanotube.

for the classical trajectory simulations. H<sub>2</sub>CO was placed at the center of mass position of the nanotube. To understand the effect of confinement inside a nanotube, collision energy was set to 0 kcal/mol. H<sub>2</sub>CO was sampled using a microcanonical sampling procedure with a vibrational energy of 102.9 kcal/mol. 1000 trajectories were performed for each diameter of the nanotube and results were analyzed.

A representative reactive trajectory giving the radical products is shown in Figure 6.5. It can be seen that, although the formaldehyde initially placed at the center of the CNT, it moves towards to inner wall of the CNT and then hovers about the wall before giving the dissociated products. The dissociated products are also found to be adsorbed to the wall of the CNT. Such behaviour is seen in nearly all of the trajectories.

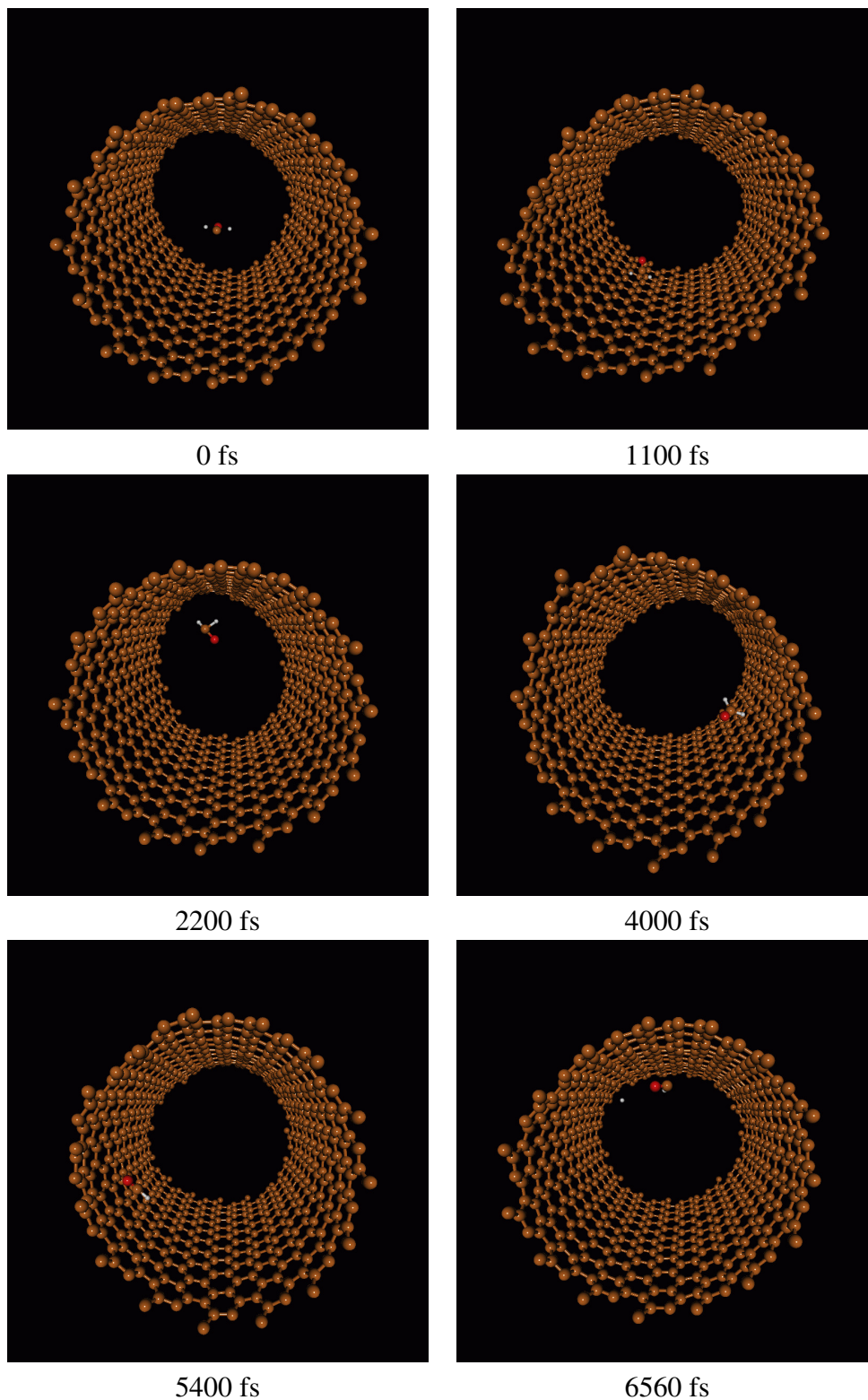


Figure 6.5: Snapshot of a representative trajectory that forms H + HCO inside a CNT.

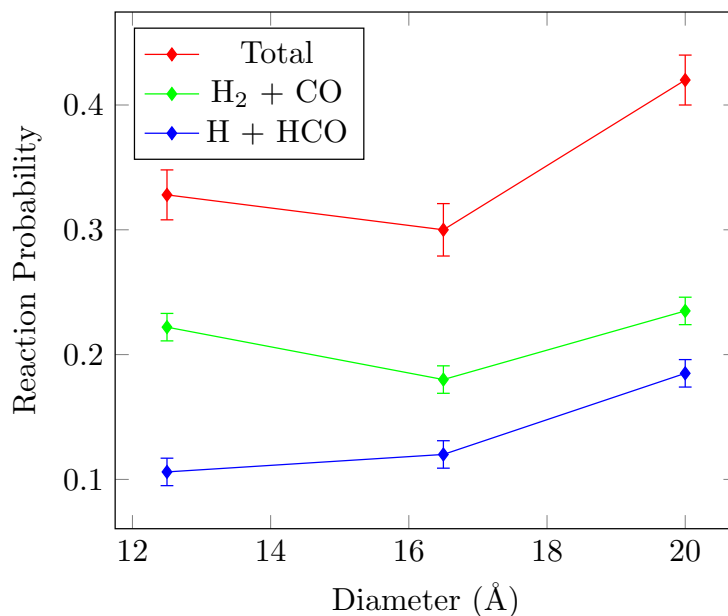


Figure 6.6: Reaction probability as a function of the diameter of carbon nanotube

Figure 6.6 shows the plot of total reaction probability along with the reaction probability for the H + HCO and H<sub>2</sub> + CO channels as a function of the diameter of carbon nanotube. With decrease in the diameter of nanotube, the reaction probability of radical channel decreased throughout but the reaction probability of molecular channel decreases from diameter 20 Å to 16.5 Å and then increases when the diameter is 12.5 Å. It is important to note that none of the trajectories followed roaming atom mechanism to form molecular product.

## 6.4 Summary

In summary, classical trajectory simulations were performed to understand the effect of confinement on the unimolecular dissociation of H<sub>2</sub>CO. To define confined space, two models were used. (i) H<sub>2</sub>CO between two the graphene sheets and (ii) H<sub>2</sub>CO inside a single-walled carbon nanotube. In case of H<sub>2</sub>CO between two graphene sheets, the reaction probability was found to decrease as the pore-size decreases. Interestingly, the reaction probability for molecular

channel was always more than the radical channel irrespective of the pore-size. In case of  $\text{H}_2\text{CO}$  inside a single-walled carbon nanotube, the reaction probability of radical channel was found to decrease as the diameter of the nanotube decreases, while, on the other hand, the reaction probability of molecular channel first decreases and then increases.

## BIBLIOGRAPHY

- [1] Levine, I. N.; Busch, D. H.; Shull, H. *Quantum chemistry*; Pearson Prentice Hall Upper Saddle River, NJ, 2009; Vol. 6.
- [2] Szabo, A.; Ostlund, N. S. *Modern quantum chemistry: introduction to advanced electronic structure theory*; Courier Corporation, 2012.
- [3] Kohn, W.; Sham, L. J. *Phys. Rev.* **1965**, *140*, A1133.
- [4] Sousa, S. F.; Fernandes, P. A.; Ramos, M. J. *J. Phys. Chem. A* **2007**, *111*, 10439–10452.
- [5] Sun, L.; Hase, W. L. *Reviews in Computational Chemistry, Vol. 19*; John Wiley & Sons, Ltd, 2003; Chapter 3, pp 79–146.
- [6] Levesque, D.; Verlet, L. *J. Stat. Phys.* **1993**, *72*, 519–537.
- [7] Smith, M. B.; March, J. *March's advanced organic chemistry: reactions, mechanisms, and structure*; John Wiley & Sons, 2007.
- [8] Kealy, T.; Pauson, P. *Nature* **1951**, *168*, 1039–1040.
- [9] Cunningham, A. F. *J. Am. Chem. Soc.* **1991**, *113*, 4864–4870.
- [10] Cunningham, A. F. *Organometallics* **1994**, *13*, 2480–2485.
- [11] Cunningham, A. F. *Organometallics* **1997**, *16*, 1114–1122.
- [12] Curphey, T. J.; Santer, J. O.; Rosenblum, M.; Richards, J. H. *J. Am. Chem. Soc.* **1960**, *82*, 5249–5250.
- [13] Meot-Ner, M. *J. Am. Chem. Soc.* **1989**, *111*, 2830–2834.
- [14] Mueller-Westerhoff, U. T.; Haas, T. J.; Swiegers, G. F.; Leipert, T. K. *J. Organomet. Chem.* **1994**, *472*, 229–246.
- [15] Pavlík, I.; Šubrt, J. *Collection Czechoslov. Chem. Commun.* **1967**, *32*, 76–88.

- [16] Hop, C.; McMahon, T. *J. Am. Soc. Mass Spectrom.* **1994**, *5*, 274–281.
- [17] McKee, M. L. *J. Am. Chem. Soc.* **1993**, *115*, 2818–2824.
- [18] Mayor-López, M. J.; Weber, J.; Mannfors, B.; Cunningham, A. F. *Organometallics* **1998**, *17*, 4983–4991.
- [19] Bühl, M.; Grigoleit, S. *Organometallics* **2005**, *24*, 1516–1527.
- [20] Mayor-López, M. J.; Lüthi, H. P.; Koch, H.; Morgantini, P. Y.; Weber, J. *J. Chem. Phys.* **2000**, *113*, 8009–8014.
- [21] Irigoras, A.; Mercero, J. M.; Silanes, I.; Ugalde, J. M. *J. Am. Chem. Soc.* **2001**, *123*, 5040–5043.
- [22] Abboud, J.-L.; Alkorta, I.; Davalos, J.; Gal, J.-F.; Herreros, M.; Maria, P.-C.; Mó, O.; Molina, M.; Notario, R.; Yáñez, M. *J. Am. Chem. Soc.* **2000**, *122*, 4451–4454.
- [23] Carey, F. A.; Sundberg, R. J. *Advanced organic chemistry: part B: reaction and synthesis*; Springer Science & Business Media, 2007.
- [24] Frisch, M. J. et al. Gaussian 09 Revision E.01. Gaussian Inc. Wallingford CT 2009.
- [25] Valiev, M.; Bylaska, E.; Govind, N.; Kowalski, K.; Straatsma, T.; Dam, H. V.; Wang, D.; Nieplocha, J.; Apra, E.; Windus, T.; de Jong, W. *Comput. Phys. Commun.* **2010**, *181*, 1477.
- [26] Lourderaj, U.; Sun, R.; Kohale, S. C.; Barnes, G. L.; de Jong, W. A.; Windus, T. L.; Hase, W. L. *Comput. Phys. Commun.* **2014**, *185*, 1074–1080.
- [27] Sharma, N. Dynamics of protonation and lithiation of ferrocene. M.Sc. thesis, School of Chemical Sciences, NISER Bhubaneswar, 2014.
- [28] Rodríguez-Otero, J.; Cabaleiro-Lago, E. M.; Pena-Gallego, A.; Montero-Campillo, M. M. *Tetrahedron* **2009**, *65*, 2368–2371.
- [29] Ahn, S.; Song, Y.-S.; Yoo, B. R.; Jung, I. N. *Organometallics* **2000**, *19*, 2777–2780.
- [30] Stepnicka, P. *Ferrocenes: ligands, materials and biomolecules*; John Wiley & Sons, 2008.
- [31] Dai, L.-X.; Hou, X.-L. *Chiral ferrocenes in asymmetric catalysis: synthesis and applications*; John Wiley & Sons, 2010.

- [32] Togni, A. *Ferrocenes: homogeneous catalysis, organic synthesis, materials science*; John Wiley & Sons, 2008.
- [33] Gamboa, J. A.; Sundararaman, A.; Kakalis, L.; Lough, A. J.; Jäkle, F. *Organometallics* **2002**, *21*, 4169–4181.
- [34] Lee, C.; Yang, W.; Parr, R. G. *Phys. Rev. B* **1988**, *37*, 785–789.
- [35] Becke, A. D. *J. Phys. Chem.* **1993**, *98*, 5648–5652.
- [36] Godbout, N.; Salahub, D. R.; Andzelm, J.; Wimmer, E. *Can. J. Chem.* **1992**, *70*, 560–571.
- [37] Frisch, M. J. et al. Gaussian 16 Revision C.01. 2016; Gaussian Inc. Wallingford CT.
- [38] Soderberg, T. **2016**,
- [39] Terrier, F. *Modern nucleophilic aromatic substitution*; John Wiley & Sons, 2013.
- [40] Destro, R.; Gramaccioli, C. M.; Simonetta, M. *Acta Crystallogr., Sect. B* **24**, 1369–1386.
- [41] Dotterer, S. K.; Harris, R. L. *J. Org. Chem.* **1988**, *53*, 777–779.
- [42] Simkin, B. Y.; Gluz, E. B.; Glukhovtsev, M. N.; Minkin, V. I. *J. Mol. Struct.* **1993**, *284*, 123–137.
- [43] Glukhovtsev, M. N.; Bach, R. D.; Laiter, S. *J. Org. Chem.* **1997**, *62*, 4036–4046.
- [44] Liljenberg, M.; Brinck, T.; Herschend, B.; Rein, T.; Tomasi, S.; Svensson, M. *J. Org. Chem.* **2012**, *77*, 3262–3269.
- [45] Fernández, I.; Frenking, G.; Uggerud, E. *J. Org. Chem.* **2010**, *75*, 2971–2980.
- [46] Sadowsky, D.; McNeill, K.; Cramer, C. J. *Environ. Sci. Technol* **2014**, *48*, 10904–10911.
- [47] Lozano, A. E.; Jimeno, M. L.; de Abajo, J.; de La Campa, J. G. *Macromolecules* **1994**, *27*, 7164–7170.
- [48] Arvanites, A. C.; Boerth, D. W. *Molecular modeling annual* **2001**, *7*, 245–256.
- [49] Bouchoux, G.; Winter, J. D.; Flammang, R.; Gerbaux, P. *J. Phys. Chem. A* **2010**, *114*, 7408–7416.
- [50] Jacobsson, M.; Oxgaard, J.; Abrahamsson, C.-O.; Norrby, P.-O.; Goddard, W.; Ellervik, U. *Chem. Eur. J.* **14**, 3954–3960.

- [51] Chen, H.; Chen, H.; Cooks, R. *J. Am. Soc. Mass Spectrom.* **2004**, *15*, 998 – 1004.
- [52] Thoelmann, D.; Gruetzmacher, H. F. *J. Am. Chem. Soc.* **1991**, *113*, 3281–3287.
- [53] Ormazábal-Toledo, R.; Contreras, R.; Tapia, R. A.; Campodónico, P. R. *Org. Biomol. Chem.* **2013**, *11*, 2302–2309.
- [54] Danikiewicz, W.; Bieńkowski, T.; Kozłowska, D.; Zimnicka, M. *J. Am. Soc. Mass Spectrom.* **2007**, *18*, 1351–1363.
- [55] Song, Y.; Chen, H.; Cooks, R. G. *Rapid Communications in Mass Spectrometry: An International Journal Devoted to the Rapid Dissemination of Up-to-the-Minute Research in Mass Spectrometry* **2005**, *19*, 3493–3499.
- [56] Landini, D.; Maia, A.; Secci, D.; M. Vlasov, V.; Os'kina, I. *New J. Chem.* **1998**, *22*, 71–74.
- [57] Giroldo, T.; Xavier, L. A.; Riveros, J. M. *Angew. Chem. Int. Edit.* **2004**, *116*, 3672–3674.
- [58] Møller, C.; Plesset, M. S. *Phys. Rev.* **1934**, *46*, 618.
- [59] Clark, T.; Chandrasekhar, J.; Spitznagel, G. W.; Schleyer, P. V. R. *J. Comput. Chem.* **1983**, *4*, 294–301.
- [60] Krishnan, R. *J. Chem. Phys.* **1980**, *72*, 650.
- [61] Dunning Jr, T. H. *J. Chem. Phys.* **1989**, *90*, 1007–1023.
- [62] Kendall, R. A.; Dunning Jr, T. H.; Harrison, R. J. *J. Chem. Phys.* **1992**, *96*, 6796–6806.
- [63] Zhao, Y.; Truhlar, D. G. *Theor. Chem. Acc.* **2008**, *120*, 215–241.
- [64] Becke, A. D. *J. Chem. Phys.* **1993**, *98*, 1372–1377.
- [65] Handy, N. C.; Cohen, A. J. *Mol. Phys.* **2001**, *99*, 403–412.
- [66] Hoe, W.-M.; Cohen, A. J.; Handy, N. C. *Chem. Phys. Lett.* **2001**, *341*, 319–328.
- [67] Perdew, J. P.; Burke, K.; Ernzerhof, M. *Phys. Rev. Lett.* **1996**, *77*, 3865.
- [68] Hamprecht, F. A.; Cohen, A. J.; Tozer, D. J.; Handy, N. C. *J. Chem. Phys.* **1998**, *109*, 6264–6271.
- [69] Boese, A. D.; Handy, N. C. *J. Chem. Phys.* **2001**, *114*, 5497–5503.

- [70] Riplinger, C.; Neese, F. *J. Chem. Phys.* **2013**, *138*, 034106.
- [71] Riplinger, C.; Sandhoefer, B.; Hansen, A.; Neese, F. *J. Chem. Phys.* **2013**, *139*, 134101.
- [72] Neese, F. *Wiley Interdiscip. Rev. Comput. Mol. Sci* **2012**, *2*, 73–78.
- [73] Okoshi, M.; Atsumi, T.; Nakai, H. *J. Comput. Chem.* **2015**, *36*, 1075–1082.
- [74] Lourderaj, U.; Sun, R.; Kohale, S. C.; Barnes, G. L.; de Jong, W. A.; Windus, T. L.; Hase, W. L. *Comput. Phys. Commun.* **2014**, *185*, 1074–1080.
- [75] Hare, S. R.; Bratholm, L. A.; Glowacki, D. R.; Carpenter, B. K. *Chem. Sci.* **2019**, *10*, 9954–9968.
- [76] Ross, J. R. *Heterogeneous catalysis: fundamentals and applications*; Elsevier, 2011.
- [77] Van Santen, R. A. *Modern heterogeneous catalysis: an introduction*; John Wiley & Sons, 2017.
- [78] Thomas, J. M.; Thomas, W. J. *Principles and practice of heterogeneous catalysis*; John Wiley & Sons, 2014.
- [79] Nogueira, J. J.; Hase, W. L.; Martínez-Núñez, E. *J. Phys. Chem. C* **2014**, *118*, 2609–2621.
- [80] Niimi, T.; Fujimoto, T.; Oishi, Y. *Comput. Mech.* **1994**, *15*, 224–232.
- [81] Rettner, C.; Auerbach, D.; Tully, J.; Kleyn, A. *J. Phys. Chem.* **1996**, *100*, 13021–13033.
- [82] Oh, J.; Kondo, T.; Arakawa, K.; Saito, Y.; Nakamura, J.; Hayes, W.; Manson, J. *J. Phys.: Condens. Matter* **2012**, *24*, 354001.
- [83] Diesing, D.; Hasselbrink, E. *Chem. Soc. Rev.* **2016**, *45*, 3747–3755.
- [84] Wodtke, A. M. *Chem. Soc. Rev.* **2016**, *45*, 3641–3657.
- [85] Chadwick, H.; Beck, R. D. *Chem. Soc. Rev.* **2016**, *45*, 3576–3594.
- [86] Majumder, M.; Gibson, K.; Sibener, S.; Hase, W. L. *J. Phys. Chem. C* **2018**, *122*, 16048–16059.
- [87] Hariharan, S.; Majumder, M.; Edel, R.; Grabnic, T.; Sibener, S.; Hase, W. L. *J. Phys. Chem. C* **2018**, *122*, 29368–29379.

- [88] Kroes, G.-J.; Díaz, C. *Chem. Soc. Rev.* **2016**, *45*, 3658–3700.
- [89] Jiang, B.; Yang, M.; Xie, D.; Guo, H. *Chem. Soc. Rev.* **2016**, *45*, 3621–3640.
- [90] Pratihari, S.; Barnes, G. L.; Hase, W. L. *Chem. Soc. Rev.* **2016**, *45*, 3595–3608.
- [91] Seenivasan, H.; Tiwari, A. K. *J. Chem. Phys.* **2013**, *139*, 174707.
- [92] Mondal, A.; Seenivasan, H.; Tiwari, A. K. *J. Chem. Phys.* **2012**, *137*, 094708.
- [93] Chadwick, H.; Beck, R. D. *Chem. Soc. Rev.* **2016**, *45*, 3576–3594.
- [94] Gibson, K.; Sibener, S. *J. Phys. Chem. A* **2016**, *120*, 4863–4871.
- [95] Zion, B.; Hanbicki, A.; Sibener, S. *Surf. Sci.* **1998**, *417*, L154–L159.
- [96] Park, G. B.; Krüger, B. C.; Meyer, S.; Kandratsenka, A.; Wodtke, A. M.; Schäfer, T. *Phys. Chem. Chem. Phys.* **2017**, *19*, 19904–19915.
- [97] Krüger, B. C.; Park, G. B.; Meyer, S.; Wagner, R. J.; Wodtke, A. M.; Schäfer, T. *Phys. Chem. Chem. Phys.* **2017**, *19*, 19896–19903.
- [98] Wlazło, M.; Majewski, J. A. *J. Chem. Phys.* **2018**, *148*, 094703.
- [99] Gurel, H. H.; Özçelik, V. O.; Ciraci, S. *J. Phys. Chem. C* **2014**, *118*, 27574–27582.
- [100] Miura, Y.; Kasai, H.; Dino, W.; Nakanishi, H.; Sugimoto, T. *J. Appl. Phys.* **2003**, *93*, 3395–3400.
- [101] Moore, C. B.; Weisshaar, J. *Ann. Rev. Phys. Chem.* **1983**, *34*, 525–555.
- [102] Van Zee, R. D.; Foltz, M. F.; Moore, C. B. *J. Chem. Phys.* **1993**, *99*, 1664.
- [103] Ghosh, A.; Subrahmanyam, K.; Krishna, K. S.; Datta, S.; Govindaraj, A.; Pati, S. K.; Rao, C. *J. Phys. Chem. C* **2008**, *112*, 15704–15707.
- [104] Patchkovskii, S.; John, S. T.; Yurchenko, S. N.; Zhechkov, L.; Heine, T.; Seifert, G. *Proc. Natl. Acad. Sci. U.S.A* **2005**, *102*, 10439–10444.
- [105] Tran, F.; Weber, J.; Wesolowski, T. A.; Cheikh, F.; Ellinger, Y.; Pauzat, F. *J. Phys. Chem. B* **2002**, *106*, 8689–8696.
- [106] Townsend, D.; Lahankar, S.; Lee, S.; Chambreau, S.; Suits, A.; Zhang, X.; Rheinecker, J.; Harding, L.; Bowman, J. *Science* **2004**, *306*, 1158–1161.

- [107] Cornell, W. D.; Cieplak, P.; Bayly, C. I.; Gould, I. R.; Merz, K. M.; Ferguson, D. M.; Spellmeyer, D. C.; Fox, T.; Caldwell, J. W.; Kollman, P. A. *J. Am. Chem. Soc.* **1995**, *117*, 5179–5197.
- [108] Zhang, X.; Zou, S.; Harding, L. B.; Bowman, J. M. *J. Phys. Chem. A* **2004**, *108*, 8980–8986.
- [109] Dodda, L. S.; Lourderaj, U. *Phys. Chem. Chem. Phys.* **2013**, *15*, 17479–17486.
- [110] Park, K.; Engelkemier, J.; Persico, M.; Manikandan, P.; Hase, W. L. *J. Phys. Chem. A* **2011**, *115*, 6603–6609.
- [111] Curtis, L. J.; Ellis, D. G. *Am. J. Phys.* **2004**, *72*, 1521–1523.
- [112] Smit, B.; Maesen, T. L. *Nature* **2008**, *451*, 671–678.
- [113] Smart, L. E.; Moore, E. A. *Solid state chemistry: an introduction*; CRC press, 2012.
- [114] Gläser, R.; Weitkamp, J. *Basic Principles in Applied Catalysis*; Springer, 2004; pp 159–212.
- [115] Santiso, E. E.; George, A. M.; Turner, C. H.; Kostov, M. K.; Gubbins, K. E.; Buongiorno-Nardelli, M.; Sliwinska-Bartkowiak, M. *Appl. Surf. Sci.* **2005**, *252*, 766–777.
- [116] Santiso, E. E.; George, A. M.; Gubbins, K. E.; Buongiorno Nardelli, M. *J. Chem. Phys.* **2006**, *125*, 084711.
- [117] Ghosh, A.; Subrahmanyam, K.; Krishna, K. S.; Datta, S.; Govindaraj, A.; Pati, S. K.; Rao, C. J. *Phys. Chem. C* **2008**, *112*, 15704–15707.
- [118] Patchkovskii, S.; John, S. T.; Yurchenko, S. N.; Zhechkov, L.; Heine, T.; Seifert, G. *Proc. Natl. Acad. Sci. U.S.A* **2005**, *102*, 10439–10444.
- [119] Tran, F.; Weber, J.; Wesolowski, T. A.; Cheikh, F.; Ellinger, Y.; Pauzat, F. *J. Phys. Chem. B* **2002**, *106*, 8689–8696.
- [120] Walther, J. H.; Jaffe, R.; Halicioglu, T.; Koumoutsakos, P. *J. Phys. Chem. B* **2001**, *105*, 9980–9987.

